Extension of the peridynamic theory of solids for the simulation of materials under extreme loadings

by
Michael R. Tupek
B.S., University of Wisconsin - Madison (2007)
S.M., Massachusetts Institute of Technology (2010)

Submitted to the Department of Aeronautics and Astronautics
in partial fulfillment of the requirements for the degree of
Doctor of Philosophy in Aeronautics and Astronautics
at the
MASSACHUSETTS INSTITUTE OF TECHNOLOGY
February 2014

Author .....
Department of Aeronautics and Astronautics
September 4, 2013

Certified by .....
Raúl Radovitzky
Professor of Aeronautics and Astronautics
Thesis Supervisor

Committee Member .....
Jaime Peraire
Professor of Aeronautics and Astronautics

Committee Member .....
Rohan Abeyaratne
Professor of Mechanical Engineering

Committee Member .....
Tomasz Wierzbicki
Professor of Mechanical Engineering

Accepted by .....
Eytan H. Modiano
Professor of Aeronautics and Astronautics
Chair, Graduate Program Committee

Extension of the peridynamic theory of solids for the simulation of materials under extreme loadings

by

Michael R. Tupek

Submitted to the Department of Aeronautics and Astronautics
on September 4, 2013, in partial fulfillment of the
requirements for the degree of
Doctor of Philosophy in Aeronautics and Astronautics

Abstract

The simulation of materials exposed to extreme loads, as is relevant in many areas of engineering, including protection materials, impact damage in turbine engines and high velocity impact in space, remains one of the key challenges in the field of computational mechanics. Despite significant advances, a fully robust and generally applicable computational framework for simulating the response of materials under a wide range of dynamic loading conditions is still lacking and the search for improved approaches continues. Existing methods suffer from a litany of limitations and drawbacks, including difficulty representing fracture, robustness issues, difficulty scaling to a large number of processors, excessive computational expense, and fundamental convergence issues for problems involving material damage.

In this thesis, we conduct a thorough investigation into the theory of peridynamics and its numerical implementation as a promising alternative approach for simulating extreme material response. Peridynamics is a relatively new nonlocal formulation of continuum mechanics based on integral equations. It includes a physical length scale and naturally supports the presence of discontinuities in the solution field. As part of the work for this thesis, we uncover fundamental limitations in existing constitutive formulations of the peridynamic theory, and propose solutions to these limitations which furnish an extended constitutive theory of peridynamic for large deformations of continua. It is shown that these issues are responsible for numerical instabilities commonly observed in peridynamic particle discretizations. Specifically, unphysical deformation modes which allow for matter interpenetration, without contributing to the strain energy, are shown to exist in the original formulation. In order to address this issue, we introduce an extension of the constitutive correspondence framework based on bond-level nonlinear strain measures. It is found that numerical instabilities are suppressed by the extended theory.

In addition, we address the issue of incorporating damage and fracture, as is required for modeling materials subjected to intense loads. In particular, two novel approaches for modeling damage and fracture within peridynamics are proposed. One

is based on classical continuum damage models, while the other is specifically suited for brittle fracture response.

A robust, scalable computational framework based on these extensions to the peridynamic theory is developed, and numerical examples are provided which demonstrate the ability to capture experimentally observed ballistic limit curves for ductile materials, as well as realistic fracture patterns in brittle materials subjected to projectile impact loadings.

Thesis Supervisor: Raúl Radovitzky
Professor of Aeronautics and Astronautics

Committee Member: Jaime Peraire
Professor of Aeronautics and Astronautics

Committee Member: Rohan Abeyaratne
Professor of Mechanical Engineering

Committee Member: Tomasz Wierzbicki
Professor of Mechanical Engineering

Acknowledgments

Many people deserve thanks for their support over the years. First and foremost, I would like to thank my adviser, Prof. Raúl Radovitzky, for allowing me to work on an exciting and challenging topic, and for giving me a lot of freedom to explore it. I greatly appreciate the encouragement and guidance he has provided, and for helping me to tell a better story. I have greatly enjoyed our many discussions about mechanics, mathematics and computer science.

Thanks to my committee members, Prof. Rohan Abeyaratne, Prof. Jaime Peraire, and Prof. Tomasz Wierzbicki, for their invaluable advice, discussion and encouragement throughout this thesis work. I would like to thank Dr. Stewart Silling and Dr. Adrien Rosolen for serving as readers for my thesis. Special thanks to Dr. Silling for formulating the theory on which most of my thesis is based and for providing many helpful comments and suggestions. I also thank Prof. Youssef Marzouk for serving as my minor advisor, and for hosting wonderful weekly reading group meetings on uncertainty quantification.

I am thankful for the financial support from the U.S. Army through the Institute for Soldier Nanotechnologies, as well as the office of naval research for funding part of this work.

I have greatly appreciated the various collaborations and discussions I'd had over the years with the other members of the RR group: Piotr Fidkowski, Abiy Tasissa, Felipe Hernandez, Srikanti Rupa Avasarala, Ganesh Gurumurth, Wendy Pino, Giovanna Bucci, and, particularly, Li Yu for our many interesting philosophical discussions. Thanks especially to Andrew Seagraves, Brandon Talamini, Lei Qiao and Michelle Nyein, as we've been together from the beginning. Thanks as well to the post-docs who have been extremely friendly and helpful over the years: Antoine Jerusalem, Ludovic Noels, Tan Bui, Claudio Pita, Julian Rimoli, Gauthier Becker, Martin Hautefeuille, Aurélie Jean, and Adrian Rosolen.

Thanks to my friends, Paul Grogan, Matt Ueckermann and Sarah Bates, for board game nights and tennis. Special thanks to my parents and sister for always encouraging me to finish as quickly as possible. Finally, I thank my wife Amanda, whose love and support over the years has made this thesis possible.

Contents

1 Introduction **17**

1.1 Ballistic impact simulation: computational approaches and issues . . 23

1.1.1 Lagrangian finite element methods 24

1.1.2 Eulerian and arbitrary Eulerian-Lagrangian formulations . . . 26

1.1.3 Particle and meshless methods 27

1.1.4 Particle discretizations based on peridynamics 29

1.2 Objectives and thesis outline 34

1.3 Summary of thesis contributions 38

2 The theory of state-based peridynamics **41**

2.1 Peridynamic states 42

2.2 Constitutive formulations 47

2.2.1 Constitutive correspondence 47

2.2.2 Ordinary peridynamic materials 49

2.3 Kinematic constraint 50

2.4 Constitutive constraint for preventing matter interpenetration 51

3 Numerical discretizations of peridynamics **53**

3.1 Particle discretization 54

3.1.1 Validation using a Taylor impact test 55

3.1.2 Numerical instabilities in constitutive correspondence 58

3.2 Ruling out numerical instabilities: finite element discretization 60
3.2.1 Finite element discretizations of constitutive correspondence: instabilities persist 64
3.2.2 Finite element discretizations of linear ordinary solids: instabilities suppressed 66
3.3 Chapter summary 69

4 An extended constitutive correspondence formulation of peridynamics based on nonlinear bond-strain measures 73
4.1 Limitation in the kinematics of constitutive correspondence 75
4.2 Finite deformation peridynamic bond-strain measures 80
4.2.1 Nonlocal peridynamic strain tensor 82
4.2.2 Properties of the family of nonlocal strain tensors $\bar{\mathbf{E}}_{(m)}$ 82
4.2.3 A fix to the issue of matter interpenetration 85
4.3 Constitutive models based on the nonlocal strain tensor 87
4.4 Chapter summary 89

5 Ordinary elastic solids based on nonlinear bond-strain measures 91
5.1 Nonlinear ordinary elastic solids 92
5.2 Limitations and fixes for ordinary elastic solids 96
5.2.1 Unphysical behavior of the linear theory under degenerate deformations 97
5.2.2 Behavior of the nonlinear theory under degenerate deformations 101
5.3 Numerical example: peridynamic Riemann problem 103
5.4 Chapter summary 107

6 Brittle damage modeling in state-based peridynamics 111
6.1 Bond failure criteria for brittle peridynamic materials 112

6.1.1 Relationship between the dissipated bond energy and the fracture energy . . . 113
6.1.2 Interpretation of the bond energy . . . 116
6.1.3 Brittle peridynamic material model . . . 119
6.2 Validation . . . 123
6.2.1 Edge-on impact test of PMMA plates . . . 123
6.2.2 Kalthoff test . . . 139
6.2.3 Scalability test . . . 142

7 Incorporating classical damage models in peridynamics 145
7.1 Constitutive correspondence with damage . . . 148
7.2 Constitutive model for metal . . . 150
7.3 Ballistic impact simulations . . . 151
7.4 Chapter summary . . . 155

8 Summary and suggestions for future research 159

A Appendix 163
A.1 Virtual power derivation of the peridynamic equations of motion . . . 163
A.2 Thermodynamic restrictions on the constitutive behavior . . . 167

List of Figures

1-1 Aluminum plate impacted by a steel sphere projectile. 18

1-2 Aluminum sandwich structures impacted at different velocities. 19

1-3 Penetration simulations of an aluminum target in LS-DYNA. 20

1-4 Simulation of a long rod projectile impacting a ceramic target using adaptive remeshing. 20

1-5 A comparison of computational approaches for simulating tungsten impacting a steel target. 21

2-1 Schematic representation of a body $\mathcal{B}_0$ and the family $\mathcal{H}(\mathbf{x})$. 42

3-1 Simulated final configurations of a Taylor impact test for varying discretization sizes. 57

3-2 Instabilities in Taylor impact for varying peridynamic horizon size and a fixed discretization size. 59

3-3 Schematic of continuous and discontinuous Galerkin approximants. . 63

3-4 Static solution for constitutive correspondence using a CG mesh. . . . 67

3-5 Static solution for constitutive correspondence using a DG mesh. . . . 68

3-6 Static solution for a linear ordinary elastic solid using a CG mesh. . . 70

3-7 Static solution for a linear ordinary elastic solid using a DG mesh. . . 71

4-1 Schematic showing a region $\mathcal{G} \subset \mathcal{B}_0$ collapsing to a single point $\mathbf{z} \in \mathcal{B}_t$. 75

4-2 Schematic of opening and closing surface discontinuities. 76

5-1 Schematic showing a region $\mathcal{G} \subset \mathcal{B}_0$ collapsing to a single point $\mathbf{z} \in \mathcal{B}_t$. 97

5-2 Schematic of opening and closing surface discontinuities. 98

5-3 Self impact for 20,000 particle mesh with $|\mathbf{v}_0| = 1200$ and $m = 1/2$. . . 106

5-4 Self impact for 20,000 particle mesh with $|\mathbf{v}_0| = 1200$ and $m = 0$. . . 107

5-5 Self impact for 35,912 particle mesh with $|\mathbf{v}_0| = 1200$ and $m = 1/2$. . . 108

5-6 Self impact for 35,912 particle mesh with $|\mathbf{v}_0| = 1200$ and $m = 0$. . . 108

6-1 Schematic showing the region within the horizon $\mathcal{H}(\mathbf{x})$ and across the fracture surface from point $\mathbf{x}$. 114

6-2 A schematic of the specimen and impactor geometry for the Mode-I edge-on impact tests of Umberger and Love on pre-notched PMMA plates. 124

6-3 Experimental results by Umberger and Love showing edge-on impact of PMMA with different initial impact velocities. 126

6-4 Nonlocal damage for a discretization with 61,600 particles, $\delta = 0.0055$ m, and varying initial impact velocities. 127

6-5 Nonlocal damage for 9,856 particle discretization, $v_0 = 15$ m/s. 129

6-6 Nonlocal damage for 22,176 particle discretization, $v_0 = 15$ m/s. . . . 129

6-7 Nonlocal damage for 39,424 particle discretization, $v_0 = 15$ m/s. . . . 130

6-8 Nonlocal damage for 61,600 particle discretization, $v_0 = 15$ m/s. . . . 130

6-9 Nonlocal damage for 109,104 particle discretization, $v_0 = 15$ m/s. . . 131

6-10 Nonlocal damage for unstructured particle distribution, $v_0 = 15$ m/s. 131

6-11 Energies over time for a 109,867 particle discretization. 132

6-12 Dissipated energy over time for various particle densities, $v_0 = 15$ m/s. 133

6-13 Damage over time with 61,600 particles, $\delta = 0.0055$, $v_0 = 35$ m/s. . . 134

6-14 Damage over time with 431,636 particles, $\delta = 0.0015$, $v_0 = 35$ m/s. . . 136

6-15 Damage for varying initial velocities, 431,636 particles, $\delta = 0.0015$. . . 137

6-16 Nonlocal damage with different initial impact velocities for edge-on impact simulations in 3D. 138
6-17 Schematic of the Kalthoff experiment 140
6-18 Nonlocal damage for simulations of the Kalthoff test. 141
6-19 Scalability plot for the peridynamic computational framework. 143

7-1 Spherical steel projectiles impacting aluminum sandwich structures: simulations and experiments. 152
7-2 Modified Johnson-Cook material model fit against uniaxial test data. 153
7-3 Residual velocity vs. initial impact velocity for sandwich panel impact. 156

List of Tables

2.1 Analogies between peridynamics and classical continuum mechanics. . 46

3.1 Material properties used in Taylor impact test simulations. 56

3.2 Comparison of Taylor impact test using different numerical methods. 57

6.1 Comparison of cohesive energy for different particle densities. 133

6.2 Comparison of Kalthoff test crack angle for different particle densities. 140

7.1 Material parameters used in ballistic impact simulations. 154

7.2 Damage parameters used in ballistic impact simulations. 155

Chapter 1

Introduction

Despite advances in the ability to describe many important aspects of the physics of ballistic impact events, computational approaches to the design of armor systems have yet to fully materialize [17]. The key to enabling a fast and relatively inexpensive approach for evaluating the effectiveness of candidate protection materials and multi-material armor systems at mitigating blast and ballistic threats is the development of a robust and accurate ballistic impact simulation framework. Additional important engineering applications for simulating impact other than ballistic loading of armor systems include spall impact damage in turbine engines [77], space debris impact [27], as well as geophysical problems [109].

As noted by a recent study from the National Academy [17], a comprehensive science-based approach for the accurate simulation of armor systems requires three may components: constitutive models which capture the correct dependence of strain, strain-rate, stress, temperature and history; computational methods which can robustly and accurately represent finite deformations and failure modes; and experiments which provide material response data for calibrating constitutive laws and for validating the computational output. The goal of his thesis is to focus on the second component, and explore particle-based numerical methods based on peridynamics for

simulating ballistic impact problems.

An important motivation for the computational efforts in this thesis are provided by a set of experimental results conducted by Professor Haydn Wadley's group at the University of Virginia. This work was part of a Multidisciplinary University Research Initiative (MURI) on cellular concepts for high intensity dynamic load mitigation. The UVA data set includes results from impact experiments on monolithic 6061-T6 aluminum plates (Figure 1-1) and corrugated aluminum sandwich structures (Figure 1-2) [46].

Due to the severe deformations involved, specialized techniques are needed which can robustly and accurately capture these deformations, and which can correctly represent the relevant failure modes. Such modeling improvements could also help successfully furnish the design and analysis of the next generation of protection material systems.

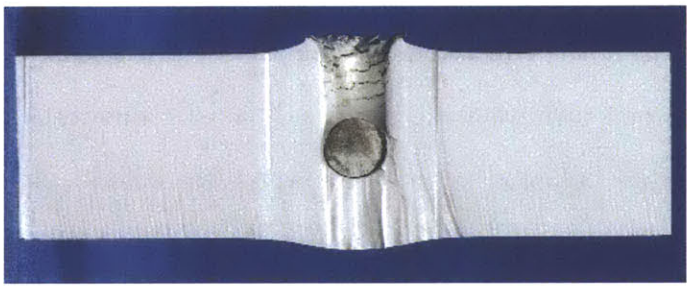

Figure 1-1: Experimental results for a monolithic 6061-T6 aluminum plate impacted by a steel sphere projectile (courtesy of Prof. Haydn Wadley).

In my Master's thesis [68] we focused on exploring the capabilities and limitations of several competing computational approaches for simulating protection materials under a extreme loading conditions. As has been mentioned, the robust and accurate simulation of ballistic impact on protective materials requires addressing some key limitation to the existing computational approaches. In particular, there are still difficulties in efficiently modeling complicated three-dimensional structures, in accurately predicting both ductile and brittle crack propagation, and in robustly handling

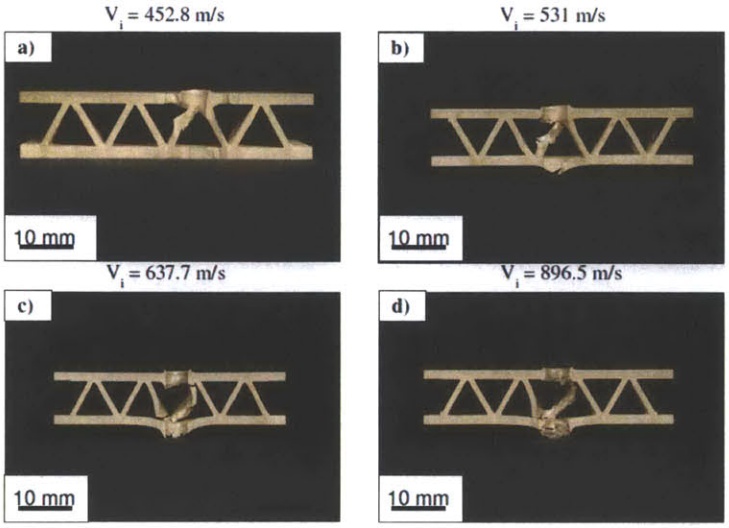

Figure 1-2: Experimental results for 6061-T6 aluminum sandwich structures impacted at different velocities (courtesy of Prof. Haydn Wadley).

severe material deformations.

The current state of the art Lagrangian solvers for simulating impact are explicit dynamics finite element codes such as LS-DYNA and EPIC. An example of a recent LS-DYNA simulation of ballistic impact is shown in Figure 1-3 [12], where severe deformations require the deletion of elements based on a calibrated phenomenological fracture criterion, and it is acknowledged that the solution is mesh dependent due to the softening part of the constitutive response. EPIC uses element deletion or element erosion as well, but also has the capability to convert meshes to particles dynamically during the simulation [50]. This conversion appears somewhat ad-hoc, but reasonably accurate results have resulted from this approach [8].

One of the approaches explored in my master's thesis was to use adaptive remeshing to handling severe deformations. A sample result using this approach is shown in Figure 1-4, where the simulation results for the impact of a long rod projectile on a ceramic target is depicted. While this approach has several appealing aspects such as a well defined field interpolation at all times and the ability to handle large

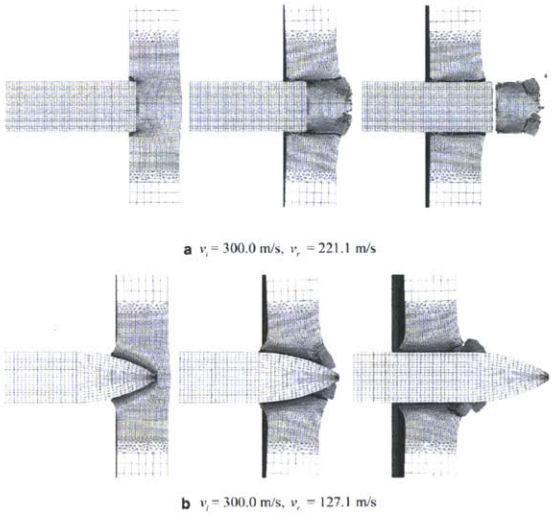

Figure 1-3: Penetration simulation with a damage model for AA7075-T651 aluminum in LS-DYNA (reproduced from [12]).

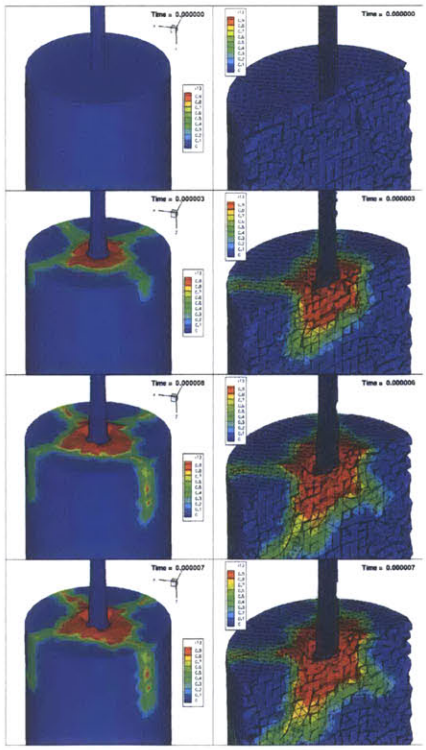

Figure 1-4: Long rod projectile impacting ceramic target with adaptive remeshing [68]. Contours depict material damage using the Deshpande-Evans ceramic damage model [19].

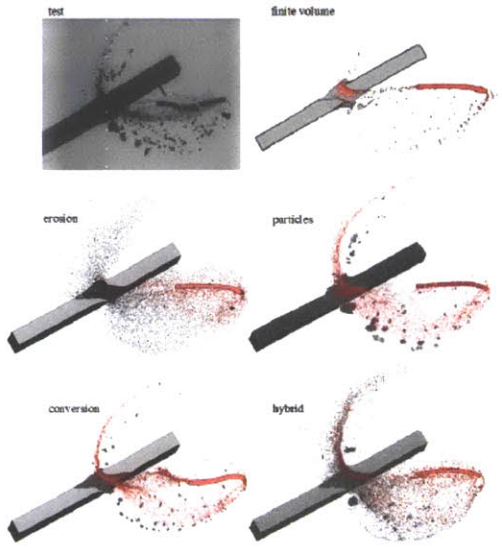

Figure 1-5: A comparison of results from five computational approaches for a tungsten projectile impacting a steel target at 1,615 m/s (reproduced from [8]).

deformation without removing mass and energy from the system via element deletion, it was found the approach is not yet sufficiently robust in 3D and limits scalability. In addition, it does not alleviate the mesh sensitivity issues associated with softening models, and in fact may exacerbate the problem by artificially diffusing material history information and damage throughout the mesh, as can be observed in Figure 1-4. The lack of a reasonable discretization approach for impact problems is demonstrated in [8], where several different computational approaches were applied to simulate the same experimental problem. Results for one such simulation are shown in Figure 1-5, where it is clear that different computational approaches such as conversion to particles, pure particle methods, element deletion, etc, lead to very different results, even when using the same constitutive model and fracture criterion.

Unsatisfied with the ad-hoc workarounds used by the existing commercial codes, and frustrated by the limitations of adaptive remeshing approaches, we began to pursue alternative approaches. One popular alternative is to use so-called particle

or meshless methods, which are summarized in Section 1.1.4. These approaches are promising, but are potentially limited by the fact that either a classical damage law or discrete crack representation approach is still required, leading to same mesh sensitivity issues associated with Lagrangian finite element approaches.

An alternative approach is based on the work of Stewart Silling and his proposed continuum theory of peridynamics, which appears to have the potential to address several of the limitations of existing methods. This continuum theory is based on a reformulated theory of classical continuum mechanics, coined by its author as peridynamics [93, 98]. The theory allows for nonlocal material point interactions, and thus introduces a characteristic physical length scale, which is often necessary for regularizing problems involving fracture and/or damage which are otherwise ill-posed. Peridynamics has enjoyed increasing popularity in the literature since it was first proposed in 2000. It is a continuum formulation which employs integral equations to evaluate internal energies instead of derivatives, with the immediate consequence that the theory is intrinsically nonlocal. Recent advances have allowed the theory to incorporate 'classical' constitutive models, traditionally based on derivatives in the displacement field, while retaining the nonlocal, integral nature of the theory. A summary of some of the potential advantages of peridynamics are as follows:

- Discontinuities such as cracks, shear bands, and phase transitions are naturally supported as a direct consequence of the lack of derivatives in the formulation.
- The theory can be naturally discretized as a particle method, so mesh entanglement issues are avoided.
- In contrast to many other nodally integrated particle discretizations, peridynamic discretization are rooted in a rigorous theoretical framework.
- Because the theory is nonlocal and includes a length-scale, convergence is possible for problems involving material property degradation and localization (i.e.,

damage, fracture).

- Similarities with molecular dynamics allows for straightforward and highly scalable parallel implementations.

- Allows for more general, nonlocal constitutive responses to be modeled.

While promising, the theory is still in its early stages of development and suffers from some limitations which we attempt to uncover and address in this thesis. In order to better understand issues with existing methods, we first review several of the main computational approaches to ballistic impact modeling.

1.1 Ballistic impact simulation: computational approaches and issues

A wide variety of computational approaches for modeling ballistic impact have been developed in the literature, with competing advantages and drawbacks according to their versatility, robustness, efficiency and/or scalability. At a fundamental level there are two general approaches to continuum mechanics simulations, which are Lagrangian methods typically based on finite element or Galerkin methods, and Eulerian methods typically based on finite difference or finite volume techniques (Eulerian hydro-codes). Lagrangian formulations track the motion of material points moving with the body and consider the evolution of field variables such as displacements, velocities, and stresses stored at these material points. Eulerian methods consider a fixed region of space and track the flow of material through this fixed spatial domain. They have, to some extent, complementary advantages and disadvantages. In the following we briefly explore a variety of approaches to simulating ballistic impact, their advantages and limitations, and our experiences with them.

1.1.1 Lagrangian finite element methods

The advantage of the Lagrangian formulation, commonly discretized using the finite element method, is that material histories at material points, boundaries and interfaces are all naturally tracked. The drawback is that severe deformations can result in stability problems which break the discretization. Deformations can cause the mesh to become ill-conditioned and can result in rapidly decreasing stable time steps and mesh entanglement, also called element inversion. Additionally, the nature of the finite element discretization requires specialized techniques for modeling fracture. Common strategies for overcoming these limitations include incorporating phenomenological cohesive zone models [103] and also the practical, but less rigorous technique of element deletion or element erosion [10]. The most common approach to representing fracture with finite elements is via continuum damage models, which phenomenologically model the degradation of material strength and/or stiffness. When the damage parameter reaches a critical value at a specific quadrature point, that element is deleted. This is also sometimes referred to as element erosion or element death. While often very successful in practice with a well calibrated material model on a particular mesh [57], this procedure is well known to be sensitive to the mesh discretization and mesh refinement. There is no known mathematical framework for this modification to the discretization, as it is purely an engineering solution, and it will often artificially remove mass, momentum and energy from the simulation. Continuum damage models, if not regularized with spatial or time gradient terms, lead to an ill-posed continuum formulation [17, 88]. When material softening occurs, the continuum solution predicts imaginary wave-speeds and damage zones of zero volume, resulting in essentially no energy loss due to fracture. When a specific mesh is chosen, the discretization itself provides a length scale and a reasonable solution can often be found, though the solution will be highly sensitive to the mesh size. The procedure of using damage models and element deletion may be easier to justify when modeling

ductile materials, as the energy dissipated during the softening regime of the material response is small compared to the energy dissipated during plastic hardening. As a result, damage models for ductile materials may be somewhat less mesh sensitive than brittle damage models.

Approaches based on cohesive zone models have succeeded in simulating conical cracks in ceramic plates using finite elements, [15] but due to computational limitations in modeling crack surfaces the simulation were conducted in 2D, and had to include a damage model to approximate the effect of radial cracks. It has become evident that to fully capture 3D effects in ballistic impact simulations, alternative scalable algorithms must be investigated. One such approach is based on a scalable implementation of discontinuous Galerkin methods with cohesive zone models on element interfaces [85]. An approach to handle large deformations involves using finite elements, combined with the ability to adaptively modify the mesh (remesh) [58]. This approach has shown some promise for impact problems in two dimensions [15], but extensions to three dimensions have proved difficult.

In my Master's work, I experimented with a continuum mechanics formulation discretized using the finite element method. Numerical examples were presented using the Deshpande-Evans ceramic damage model for modeling brittle ceramic with a mechanism-based damage model [19]. These results demonstrated the constitutive model's ability to predict experimentally observed crack patterns, such as conical shaped crack patterns and multiple radial cracks emanating from the impact zone. Additional examples, which utilized adaptive remeshing algorithms, probed the limitations of the Lagrangian finite element method's ability to predict long rod penetration in a ceramic target and the transition from dwell to penetration. The full potential for this approach to modeling hypervelocity ballistic impact remains unclear, as even frequent adaptive remeshing was unable to avoid element inversion for the impact conditions considered. A sample result using this framework is shown in

Figure 1-4.

1.1.2 Eulerian and arbitrary Eulerian-Lagrangian formulations

As mentioned in the National Academies study [17], Eulerian-based hydro-codes were primarily developed by the DoE and DoD, and their history is discussed in detail in the review by Benson [20]. These codes are still frequently used to this day in the ballistic impact community due to their general robustness and scalability. These approaches are in general only first or second order accurate in time, and first order accurate in space. This low order of accuracy could affect the efficiency of such approaches, and limit their ability to rigorously handle more complicated constitutive laws, such as rate independent damage models, which require additional length scales for regularizing an otherwise ill-posed problem. In addition, for material models with history or internal variables, such as many common constitutive laws for plasticity and damage, the internal variables at material point must be advected by the flow. This introduces additional inaccuracies due to numerical dispersion effects on the advected material point information and incompatibility between the advected material point data and the computed deformation state. This additional inaccuracy can be devastating to the physics of the problem and is often overlooked. To overcome this, many only use constitutive laws formulated in rate form, which may introduce additional discretization error or limit the variety of constitutive models possible. Eulerian approaches suffer from a variety of additional complications, such as difficulty in imposing boundary conditions, difficulty in tracking interfaces and difficulty in accurately and robustly advecting history variables.

Another related method for impact simulations is arbitrary-Lagrangian-Eulerian (ALE) approaches. These attempt to combine aspects of both Lagrangian and Eulerian approaches to improve robustness. They can be thought of as Lagrangian

approaches defined on a moving background mesh, which require at each time-step a remapping back to the newly updated computational domain [20]. In this manner, they can track deforming interfaces and can make boundary condition imposition more straightforward. However, for material models with history they still suffer from the same drawbacks as purely Eulerian methods, which must advect material point data, reducing simulation accuracy.

1.1.3 Particle and meshless methods

Particle based numerical methods for simulating impact problems are believed to provide an advantage in robustness over more traditional methods, such as finite elements and finite differences. The origin of such methods dates back to the smooth particle hydrodynamic (SPH) method, an idea independently introduced in the papers by Lucy [60] and Gingold and Monaghan [84]. An early review by Monaghan [43], along with a more recent review [44] discuss the many advances in techniques for overcoming some of the initial limitations of the method. The primary motivation for these particle methods comes from the astrophysics community's desire to solve hydrodynamic PDEs, but has since been adapted by the computational solid mechanics community, where it is sometimes called smooth-particle applied mechanics (SPAM) [116]. A variational formulation of SPH simulations for both fluids and solids has also been proposed [38]. Several recent papers have used the method for simulating high velocity impact [87, 33] including experimental validation using a Taylor impact test [16]. While extremely robust, the method is well known to have several computational limitations, specifically, the so-called tensile instability, zero energy modes, and difficulties with boundary conditions. Several of these issues have been resolved using somewhat ad-hoc remedies, but at the expense of additional computational costs [44, 116]. The critical advantage of SPH and SPAM methods is their generality and robustness, in particular in the presence of severe material deformations.

This has motivated the development of methods combining Lagrangian finite element methods with the ability to convert elements into SPH particles dynamically during a simulation when elements become too distorted [50].

Meshless methods are a related family of methods which have shown promise for ballistic impact problems involving large deformations. Meshless methods based on the Galerkin procedure for solving partial differential equations were first proposed in a paper by Nayroles on the diffuse element method [5] and further developed by Belytschko with the element-free Galerkin (EFG) method [108]. Various other extensions, improvements, generalizations and alternative formulations have been explored since, including the reproducing kernel particle method (RKPM) [117],[118], h-p clouds [14], partition of unity [48], the local meshless Petrov-Galerkin method (MLPG) [106], the method of finite spheres [92] and the local maximum entropy method [63]. The MLPG method has been validated using a Taylor impact benchmark test [124] and has been shown to be more robust for problems involving ballistic impact than a finite element approach. An extension of the EFG method using moving least square (MLS) approximations combined with an extrinsic crack field enrichment has been successfully applied in two dimensions to a high-speed ballistic impact [122].

An alternative hybrid particle/mesh-based method, originally called the Hamiltonian particle hydrodynamics method, avoids the tensile and boundary instabilities known to plague many particle based methods [26]. The algorithm works by using particles to model contact and impact, as well as material response under compression, while a finite element discretization is used to compute tensile and shear response. The method has been applied to various problems, including hypervelocity impact [26] and orbital debris impact [27]. The method is further improved by a parallel implementation which helps its efficiency. While the method is robust for modeling brittle materials, it is still limited for ductile materials undergoing large shear strains, as elements are still prone to failure in tension and shear.

An interesting recent development in meshless methods uses ideas from variational calculus and in particular, optimal transportation theory, combined with maximum entropy meshfree interpolations [63, 4]. The method has been successfully applied to problems in both fluid and computational mechanics and has been validated using the Taylor impact benchmark problem [4]. Most of these methods overcome some of the specific shortcomings of SPH methods, however the associated computational costs are relatively high, which could hinder their widespread use. Additionally, they do not overcome the mesh sensitivity issues associated with continuum damage laws.

1.1.4 Particle discretizations based on peridynamics

An alternative Lagrangian particle approach is based on discretizations of the peridynamic formulation of continuum mechanics [93, 98]. Peridynamics is a continuum theory based on a generalization of the local stress assumption of classical continuum mechanics to allow for forces acting at a distance, thereby introducing a length scale to the continuum description. The typical assumption of local stress states in a material limits the interaction of materials points to immediate neighbors in direct contact with each other. The alternative approach taken in peridynamics is a continuum theory based on integral equations, which "sums" force contributions from material points acting at a distance. The material behavior is determined by these nonlocal interactions, where the interaction forces are taken to be functions of the deformation within a finite neighborhood of material. In a sense, the peridynamics theory more closely resembles molecular dynamic interactions where forces act on atoms at a distance. All continuum theories are ultimately homogenized macro-scale approximations of these atomistic interactions. The idea for peridynamics was first proposed by Silling in 2000 [93]. The initial model was restricted to elastic materials which in three dimensions have a Poisson's ratio, $\nu = 0.25$. This initial theory laid the foundation of what is now known as bond-based peridynamics, which only considers

pairwise interaction between distinct material points. A more recent extension of the theory, named state-based peridynamics, was introduced by Silling *et al.* in 2007 [98] and allows for more general interaction potentials and interaction forces between distinct material points.

Peridynamics, is a so-called strongly nonlocal theory due to its integral formulation and its explicit inclusion of forces acting at a distance. By contrast, classical continuum constitutive laws result in local theories which in the presence of either plastic softening or damage, suffer from the emergence of negative tangent moduli and therefore imaginary wave speeds [126]. Boundary value problems with such a constitutive response are mathematically ill-posed, as material softening will localize to an infinitesimal region. To solve this issue, a physical length scale must be introduced into the constitutive description using nonlocal theories. Such theories are broadly grouped into two categories: weakly nonlocal and strongly nonlocal [126]. Strain gradient and higher order gradient theories such as those of the Mindlin variety [86] are examples of weakly nonlocal theories, as the nonlocal effects are approximated by evaluating higher order gradients locally. The peridynamics theory, a strongly nonlocal theory, accepts nonlocal interactions from the onset, thereby providing a physical length scale to regularize the continuum description.

A further distinction of the theory compared to classical elasticity theories is the complex dispersion relation which results from to the nonlocal interactions. The issue also arises in other nonlocal models including higher order gradient theories [86] and strongly nonlocal theories [2, 74]. For a homogeneous classical linear elastic material, the wave speed is independent of the wave number, but this is not in general true for peridynamics. It is known that all real materials exhibit complex dispersion behavior at sufficiently small wavelengths [74] and it has been shown that specific peridynamic models are able to reproduce the "exact" elastic dispersion relation for sufficiently large wave number, or equivalently, sufficiently small peridynamic horizon

length [73, 74].

From the point of view of numerical methods, common discretizations of peridynamics lead to a particle based method which is similar to other meshless discretizations of classical continuum mechanics in that the internal forces are work conjugate to particle displacements. The main difference is that the peridynamic discretization uses no elements, basis functions, kernels, or ad hoc differencing techniques. Compared to many common particle methods, one of the key advantages of a particle method based on peridynamics is that it directly inherits important properties of the peridynamic formulation such as strict conservation of linear and angular momentum, and can utilize classical constitutive models, such as viscoplasticity [98, 52].

Owing to the integral formulation and the relaxed continuity requirements, fracture and fragmentation can be introduced in a natural manner without the need for cohesive elements or other devices commonly used in classical continuum discretizations [103]. As no gradient terms arise in the formulation, the equations are still valid in the presence of discontinuities such as cracks and phase boundaries. This eliminates the need for additional constitutive assumptions at the interface. This benefit is not without its own complications, as it is accompanied with the additional burden of incorporating additional constitutive information, such as a failure criterion, directly into the continuum formulation. Significant effort has already gone towards developing and utilizing the advantages of the peridynamic formulation for modeling material failure [95, 94, 22, 67, 100, 121]. The convergence properties of bond-based peridynamics for modeling crack propagation were numerically investigated by Bobaru, *et al.* [28]. This investigation helped to establish the notion that both the spatial resolution of the discretization, along with the length scale introduced by the peridynamic formulation must be considered when evaluating the properties and convergence of a peridynamic discretization.

Since its inception, peridynamics has already been used in a variety of different

continuum mechanics applications. These include membrane and fiber models [95], phase transitions [53], inter-granular fracture [22], and heat transfer [28]. An implementation of peridynamics using traditional finite element codes, via beam elements, has been presented in [89]. A bond based formulation has also been implemented in a molecular dynamics code, LAMMPS [67]. Analytical results have shown the dependence of the nonlocal effect of the bond-based model on the material response for simplified 1D scenarios [99, 64, 73]. Peridynamic formulations of continua have been demonstrated for meso-scale modeling of material response [22]. In this respect, peridynamics may provide a means of bridging length scales within a multi-scale paradigm. Several results exist on the mathematical properties of the bond-based theory, including well-posedness and convergence [25, 96]. In particular, it has been proved that elastic bond-based peridynamics converges to classical elasticity for the special case where the Poisson's ratio is $\nu = 0.25$ [96]. It has also been shown that there is a correspondence between strain gradient elasticity and elastic peridynamics [96]. This comparison between the theories is only applicable in situations where the displacement fields are sufficiently smooth to permit a classical interpretation, and is no longer meaningful near strong discontinuities. In this sense, peridynamics can be viewed as an extension of classical continuum theories.

In the original peridynamic formulation the classical equation of conservation of linear momentum is replaced by the bond-based peridynamic equation of motion:

$$\rho\ddot{\mathbf{u}}[\mathbf{x},t] = \int_{\mathcal{B}} \mathbf{f}\left(\mathbf{u}[\mathbf{x}',t] - \mathbf{u}[\mathbf{x},t], \mathbf{x}' - \mathbf{x}\right) dV_{\mathbf{x}'} + \mathbf{b}[\mathbf{x},t] \tag{1.1}$$

where the ρ is the density of the material at the point $\mathbf{x}$ in the reference configuration, $\mathbf{u}$ the displacement field, $\mathbf{b}$ is a prescribed body force density, and $\mathcal{B}$ the domain of the body under consideration in the reference configuration. Each pair of particles in the body interacts through the vector valued function $\mathbf{f}\left(\mathbf{u}[\mathbf{x}',t] - \mathbf{u}[\mathbf{x},t], \mathbf{x}' - \mathbf{x}\right)$. The

integral term should be interpreted as the force per unit reference volume which is due to its interaction with other particles in the body. It is typically assumed that the function $\mathbf{f}$ has spherical compact support of radius δ centered at $\mathbf{x}$. This peridynamic horizon radius can be tuned to capture the relevant physical length scale. In the limit of this radius going the zero, the theory in 3D reduces to classical elasticity with $\nu = 0.25$ [96].

While advantageous for problems involving nonlocal effects and discontinuities, bond-based peridynamics is limited to pairwise interactions via central acting forces. This leads to a limitation on the Poisson's ratio and means that any plasticity formulation will require permanent volumetric deformations. This imposes a strong limitation on the variety of materials which can be accurately modeled using the theory.

To address these issues, Silling *et al.* developed a new formulation of peridynamics called *state-based peridynamics* [98] (reviewed in Chapter 2). This formulation is a significant generalization of the peridynamic framework which allows the response of the material at a given point to depend on the collective deformation of all points in the neighborhood, leading to a nonlocal measure of deformation analogous to the deformation gradient tensor of classical continuum mechanics (e.g., [65]). As a result, in state-based peridynamics it is in principle possible to consider a much broader class of constitutive models. In particular, it allows for inelastic materials and elastic materials with Poisson's ratio other than 0.25 to be modeled. The ability of this state-based peridynamics theory to model viscoplasticity has been demonstrated and validated using a Taylor impact test [52].

It therefore appears that the state-based formulation of peridynamics possesses many of the features required to model extreme material response. However, it is also clear that significant developments are necessary for formulating specific constitutive models within the state-based framework. In particular, it remains unclear how to

incorporate the description of material damage and fracture in a manner that is consistent with established models of brittle and ductile material failure. In addition, there have been reports of numerical issues in particle discretizations of this theory [21, 81] which need to be addressed before the method can have widespread use.

1.2 Objectives and thesis outline

In this thesis, we explore the state-based formulation of peridynamics as a potential candidate for modeling the failure response of materials subject to intense loadings. The end goal is to formulate a sound computational framework which ideally has the following properties:

- robustly produces simulation results which do not exhibit numerical instabilities, such as zero-energy modes, common to many meshless approaches
- can represent and accurately predict the onset of fracture and crack propagation, and can reliably compute the energy dissipated in this process
- produces simulation results in which fracture paths and dissipated energies are relatively insensitive to the discretization, and ideally converge to a fixed value for small mesh sizes
- can use both classical constitutive models as well as specialized peridynamic constitutive models
- scalable so that small-scale features of fracture may be sufficiently resolved

The organization of this thesis is as follows. For completeness and in order to fix notation, we provide an overview of the state-based theory of peridynamics in Chapter 2. In addition, we discuss the kinematic constraint of peridynamics and the issue of matter interpenetration, which plays a key role in developments of Chapters 3–5.

An additional constitutive condition is suggested which enables a natural enforcement of the kinematic constraint.

In Chapter 3, we focus on numerical discretizations of state-based peridynamics. We first provide an overview of the common particle discretization, and validate our C++ implementation using a Taylor impact test. However, we then show simple examples which exhibit unphysical instabilities when using the *constitutive correspondence* version of peridynamics. In order to eliminate the possibility of numerical zero-energy modes associated with under-integration, we introduce a novel finite element discretization of state-based peridynamics. Even after addressing the numerical issues, we find that the instabilities still persist for discretizations of *constitutive correspondence*. This suggests that the observed instabilities are due to issues with the theoretical framework of the original *constitutive correspondence* formulation. Chapters 4 and 5 are devoted to developing two different theoretical extensions of the peridynamic theory which address this issue.

In Chapter 4, we propose an extension of the *constitutive correspondence* framework of peridynamics. The main motivation for this development is to address unphysical deformation modes (i.e. matter interpenetration and zero-energy modes). We show analytically that these modes are present in the original formulation and are the likely cause of the numerical instabilities observed in Chapter 3. We believe that this limitation may have inadvertently mired a wider application of peridynamics methods [81]. The basic approach we propose is to introduce nonlocal peridynamic strain tensors which are in turn based on corresponding bond-level Seth-Hill strain measures. These bond-strain measures inherently avoid violations of the matter interpenetration constraint. Several examples are used to show that the modified theory avoids issues of matter interpenetration in cases where the original theory fails. The resulting *extended constitutive correspondence* framework supports general classic constitutive laws as originally intended. It is shown that the formulation also belongs to

a specific class of peridynamics constitutive models referred to as *ordinary* [98].

Another key contribution, which is discussed in Chapter 5, is an alternative approach for developing ordinary peridynamic constitutive models based on the nonlinear bond-strain measures first introduced in Chapter 4. It is shown that the proposed formulation extends the existing linear theory of ordinary peridynamics to large deformations. Unlike *constitutive correspondence*, the original linear theory does not exhibit zero-energy modes in simulations; however, we show that it does still allow for the possibility of matter interpenetration. Similar to the extended correspondence approach in Chapter 4, we overcome this limitation by using nonlinear bond-strain measures which preclude unphysical deformations on a bond-by-bond basis. Both analytical and numerical examples are provided to highlight the advantage of the nonlinear constitutive theory over its linear counterpart.

The issues of incorporating material damage in peridynamics, as is required for modeling materials subjected to intense loads, is discussed in Chapters 6 and 7. In Chapter 6, a general bond-failure criterion for brittle state-based peridynamic materials is introduced. This bond failure criterion is an extension of existing bond-failure criteria [94, 121, 39] with two essential new ingredients. The first ingredient is based on the observation that the bond-energy dissipated when severing bonds is difficult to estimate in state-based peridynamics (for materials which are not *bond-based*) due to the fact that this energy depends on the collective action of neighboring bonds and on whether other bonds are being severed simultaneously. We show that in the case of state-based peridynamic, the energy associated with cutting a single bond instantaneously (with all other bonds unchanged) can be easily quantified and thus constitutes a practical quantity on which to base a bond-failure criterion. In practice, we find that this assumption (that bonds are severed instantaneously with other bonds unchanged) accurately predicts the energy dissipated in numerical simulations. The second ingredient is a bond-energy failure function which determines the bond-

energy required to sever a bond as a function of the bond's reference length. Similar to existing approaches, the proposed bond-failure criterion is related to the classical fracture energy, G_c, of the material for the case when all bonds are severed across an interior 'fracture' surface.

In order to demonstrate the various theoretical advances and extensions proposed in this thesis, a scalable computational implementation of the improved peridynamic theory was developed. This development included incorporating the peridynamic discretization approach into a conventional finite element code, implementing algorithms and data structures to determine and update particle interactions, and implementing a ghost element parallelization strategy using C++/MPI. In addition, it required the implementation of discretized versions of various peridynamic constitutive models. The result of this effort is a numerical tool for investigating the types of problems which initially motivated the theoretical extensions proposed in this thesis.

The versatility and robustness of the developed framework is evaluated using two validation problems which are challenging benchmarks for numerical simulations of brittle fracture. These tests highlight the capability of the proposed framework to capture experimentally observed fracture patterns in brittle materials subjected to projectile impact loadings. The two tests we consider are: 1) an edge-on impact problem which results in Mode-I crack propagation and 2) the Kalthoff test which exhibits "mixed-mode" crack propagation. For the Mode-I impact problem, we demonstrate that the numerically computed dissipated fracture energy is consistent with the fracture energy, G_0, which is provided as an input parameter. We also show that the dissipated fracture energy for Mode-I fracture is remarkably insensitive to changes in mesh size. These results highlight a key advantages of the peridynamic fracture modeling approach over many existing approaches, which is that fracture energies and predicted crack paths can converge as the discretization is refined. We also qualitatively capture the experimentally observed transition from Mode-I crack propagation

to crack branching which occurs in experiments for increasing initial impact velocities. We also show that simulations of the Kalthoff test for brittle fracture are capable of predicting the experimentally observed angle of crack propagation.

An approach for incorporating classical continuum damage models in the state-based theory of peridynamics is proposed in Chapter 7. Currently, damage has only been incorporated in the peridynamics formulation via specialized bond-severing criteria, which may not reflect known fracture mechanisms for general brittle or ductile solids. The proposed approach has the advantage of enabling the description of the damage evolution processes in peridynamics according to well-established models. The main idea is to modify the peridynamic influence function according to the state of accumulated damage. As a result, peridynamic bonds between nonlocal material points are severed in accordance with the damage law. The proposed peridynamic damage formulation is implemented for the particular case of a well established ductile damage model for metals. The model is then applied to the simulation of ballistic impact of extruded corrugated aluminum panels and compared with experiments.

We conclude in Chapter 8 with a summary of the results and some suggestions for future research.

1.3 Summary of thesis contributions

- Investigated numerical instabilities in particle discretizations of the constitutive correspondence version of state-based peridynamics.

- Developed and implemented a finite element discretization of state-based peridynamics.

- Showed that instabilities in the constitutive correspondence theory of peridynamics are due to flaws in the theory, namely that there is no mechanism for preventing matter interpenetration.

- Suggested an additional constitutive condition to naturally enforce the kinematic constraint of peridynamics and thereby prevent matter interpenetration.
- Proposed an extension of the constitutive correspondence formulation of peridynamics based on nonlinear bond-strain measure which naturally prevent matter interpenetration.
- Showed that the linear ordinary solids formulation of peridynamics is also not guaranteed to prevent matter interpenetration.
- Proposed a nonlinear extension of linear ordinary solids based on bond-strain measures which naturally prevent matter interpenetration.
- Conducted numerical simulations which demonstrate that the nonlinear ordinary theory prevents matter interpenetration in cases where the linear theory fails.
- Proposed a generalized bond-failure criterion for brittle state-based peridynamic materials, calibrated to dissipate a specified fracture energy of G_c per unit area.
- Developed a parallel computational framework in C++/MPI for simulating brittle peridynamic materials and showed that simulated results can capture experimentally observed fracture patterns and dissipated energies which are remarkably insensitive to discretization size.
- Proposed an approach for incorporated classical damage models in peridynamics which was validated using a ballistic impact test.
- Provided an alternative derivation of the peridynamic equations of motion and the *nonpolar* constraint based on virtual power and frame-invariance arguments.

Chapter 2

The theory of state-based peridynamics

For completeness and in order to fix notation, in this chapter we briefly review the basic notation and concepts related to state-based peridynamics, primarily following the notation and approach in [98, 97]. In addition, we include a discussion of the issue of matter interpenetration and the kinematic constraint, which plays a key role in Chapters 3-5. An additional constitutive condition is proposed which naturally ensures that the kinematic constraint holds.

State-based peridynamics is a nonlocal continuum theory which describes the dynamics of a continuum body which occupies the region $\mathcal{B}_0 \subset \mathbb{R}^3$ in the reference configuration at time $t = 0$ and the region $\mathcal{B}_t \subset \mathbb{R}^3$ at time t. It can be viewed as a generalization of the bond-based peridynamics theory and also generalizes classical continuum mechanics to include nonlocal material point interactions.

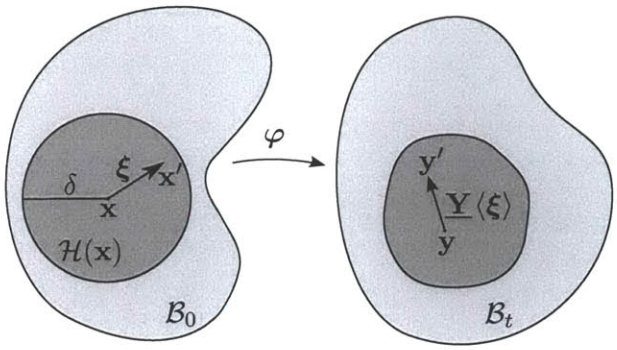

Figure 2-1: Schematic representation of a body $\mathcal{B}_0$ and the family $\mathcal{H}(\mathbf{x})$ under the mapping $\boldsymbol{\varphi}$.

2.1 Peridynamic states

Consider material points in the reference configuration $\mathbf{x}, \mathbf{x}' \in \mathcal{B}_0$. From the perspective of point $\mathbf{x}$, the *bond* to $\mathbf{x}'$ is the vector

$$\boldsymbol{\xi} := \mathbf{x}' - \mathbf{x}.$$

Under the deformation mapping $\boldsymbol{\varphi} : \mathcal{B}_0 \to \mathcal{B}_t$, points $\mathbf{x}$ and $\mathbf{x}'$ map to

$$\mathbf{y} = \boldsymbol{\varphi}(\mathbf{x}) \text{ and } \mathbf{y}' = \boldsymbol{\varphi}(\mathbf{x}'),$$

respectively. Following the definition from [97], a *family* $\mathcal{H}$ at $\mathbf{x}$ is given by

$$\mathcal{H}(\mathbf{x}) := \left\{ \boldsymbol{\xi} \in \mathbb{R}^3 \mid (\boldsymbol{\xi} + \mathbf{x}) \in \mathcal{B}_0,\ |\boldsymbol{\xi}| < \delta \right\},$$

where δ provides a physical length scale. A schematic of a peridynamic body and the family at $\mathbf{x}$ is shown in Figure 2-1.

The state-based theory of peridynamics is formulated in terms of mathematical objects called peridynamics states which are used to express peridynamic constitutive relations and peridynamic equations of motion in a compact notation. In peridynamic theory they play a role analogous to tensors in classical continuum theories [97].

A peridynamic vector-state $\underline{\mathbf{A}}\,[\mathbf{x}] \in \mathcal{V}^3(\mathbf{x})$ at a point $\mathbf{x} \in \mathcal{B}_0$ is a function

$$\underline{\mathbf{A}}[\mathbf{x}]\,\langle\cdot\rangle : \mathcal{H}(\mathbf{x}) \to \mathbb{R}^3,$$

where $\mathcal{V}^3(\mathbf{x}) := \mathcal{H}(\mathbf{x}) \times \mathbb{R}^3$ is the space of vector-states at $\mathbf{x}$. Note the analogy to a tensor $\mathbf{A} \in \mathbb{R}^3 \times \mathbb{R}^3$. Similarly, a peridynamic scalar-state $\underline{\mathbf{a}}\,[\mathbf{x}] \in \mathcal{V}^1(\mathbf{x})$ is a function

$$\underline{\mathbf{a}}[\mathbf{x}]\,\langle\cdot\rangle : \mathcal{H}(\mathbf{x}) \to \mathbb{R},$$

where $\mathcal{V}^1(\mathbf{x}) := \mathcal{H}(\mathbf{x}) \times \mathbb{R}$ is the space of scalar-states. Peridynamic vector-states are denoted in this thesis using bold type-faced capital letters with an underscore, while scalar-states are denoted using standard type-faced lowercase letters with an underscore.

Following the standard peridynamic conventions [98, 97], we use square brackets to indicate the field dependence over space $\mathbf{x}$ and time t, we use angle brackets to express dependence on the bonds $\boldsymbol{\xi} \in \mathcal{H}(\mathbf{x})$, and we use parentheses to express dependence on other variables and vector-states. We will often suppress the field dependence on $\mathbf{x}$ and t to simplify notation, when there are no ambiguities. For a functional

$$f(\underline{\mathbf{A}}) : \mathcal{V}^d \to \mathbb{R},$$

with $d = 1$, $d = 2$, or $d = 3$, we denote its Fréchet derivative with respect to the vector-state $\underline{\mathbf{A}}$ by $f_{,\underline{\mathbf{A}}}$. We refer the reader to [97] for a definition of the Fréchet derivative used in this context, noting that our notation differs slightly in that we also add a comma before the vector-state. Note that the Fréchet derivative of a functional of a vector-state is itself a vector-state [97]. The inner product between

peridynamic vector-states $\underline{\mathbf{A}}$, $\underline{\mathbf{B}} \in \mathcal{V}^d$, is defined by the operation $\bullet : \mathcal{V}^d \times \mathcal{V}^d \to \mathbb{R}$,

$$\underline{\mathbf{A}} \bullet \underline{\mathbf{B}} := \int_{\mathcal{H}(\mathbf{x})} \underline{\mathbf{A}} \langle \boldsymbol{\xi} \rangle \cdot \underline{\mathbf{B}} \langle \boldsymbol{\xi} \rangle \, d\boldsymbol{\xi},$$

where $\cdot$ denotes the standard inner-product between vectors in $\mathbb{R}^d$. For two vector-states $\underline{\mathbf{A}}$, $\underline{\mathbf{B}} \in \mathcal{V}^d$, vector-state addition, which maps $\mathcal{V}^d \times \mathcal{V}^d \to \mathcal{V}^d$ is defined bond-wise by

$$(\underline{\mathbf{A}} + \underline{\mathbf{B}}) \langle \boldsymbol{\xi} \rangle := \underline{\mathbf{A}} \langle \boldsymbol{\xi} \rangle + \underline{\mathbf{B}} \langle \boldsymbol{\xi} \rangle, \quad \forall \boldsymbol{\xi} \in \mathcal{H}.$$

Similarly, for two scalar-states $\underline{\mathbf{a}}$, $\underline{\mathbf{b}} \in \mathcal{V}^1$, scalar-state multiplication, which maps $\mathcal{V}^1 \times \mathcal{V}^1 \to \mathcal{V}^1$ is defined bond-wise by

$$(\underline{\mathbf{ab}}) \langle \boldsymbol{\xi} \rangle := \underline{\mathbf{a}} \langle \boldsymbol{\xi} \rangle \, \underline{\mathbf{b}} \langle \boldsymbol{\xi} \rangle, \quad \forall \boldsymbol{\xi} \in \mathcal{H}.$$

An simple example of a scalar-state is the identity state $\underline{1}[\mathbf{x}] \in \mathcal{V}^1(\mathbf{x})$ with

$$\underline{1}[\mathbf{x}] \langle \boldsymbol{\xi} \rangle := 1, \quad \forall \boldsymbol{\xi} \in \mathcal{H}(\mathbf{x}).$$

An important example of a vector-state is the deformation vector-state $\underline{\mathbf{Y}}[\mathbf{x}] \in \mathcal{V}^3(\mathbf{x})$, which is defined as

$$\underline{\mathbf{Y}}[\mathbf{x}] \langle \boldsymbol{\xi} \rangle := \mathbf{y}' - \mathbf{y} = \boldsymbol{\varphi}(\mathbf{x} + \boldsymbol{\xi}) - \boldsymbol{\varphi}(\mathbf{x}), \quad \forall \boldsymbol{\xi} \in \mathcal{H}(\mathbf{x}). \tag{2.1}$$

The deformation vector-state is the primary deformation measure in peridynamics, and it assigns every bond to its deformed image. A critical, physically motivated, kinematic constraint in continuum mechanics is that distinct material points in the reference configuration remain distinct in the deformed configuration, or in other words, the deformation mapping must be one-to-one. In classical mechanics, a nec-

essary condition for this constraint is

$$\det(\mathbf{F}) > 0, \tag{2.2}$$

which ensures that the material density remains positive and finite, and, in turn, that the material can not fully collapse or invert to obtain negative volume. The condition that the mapping is one-to-one in peridynamics can be expressed directly in terms of the deformation vector-state [98, 97]:

$$\underline{\mathbf{Y}}[\mathbf{x}]\langle\boldsymbol{\xi}\rangle \neq \mathbf{0}, \quad \forall \boldsymbol{\xi} \neq \mathbf{0} \in \mathcal{H}(\mathbf{x}), \quad \forall \mathbf{x} \in \mathcal{B}_0. \tag{2.3}$$

The peridynamic equations of motion are written in terms of the force vector-state $\underline{\mathbf{T}}$, where $\underline{\mathbf{T}}\langle\boldsymbol{\xi}\rangle$ is a bond-force with units of force per unit volume-squared which acts as an interaction force between nearby materials points. In peridynamics, the force vector-state plays an analogous role to the stress tensor in classical continuum theories. The peridynamic equations of motion are [98]:

$$\rho_0 \ddot{\mathbf{y}} = \int_{\mathcal{H}(\mathbf{x})} \underline{\mathbf{T}}\langle\boldsymbol{\xi}\rangle - \underline{\mathbf{T}}'\langle\boldsymbol{\xi}'\rangle \, d\boldsymbol{\xi} + \mathbf{b}, \tag{2.4}$$

where $\underline{\mathbf{T}}'\langle\boldsymbol{\xi}'\rangle = \underline{\mathbf{T}}[\mathbf{x}']\langle -\boldsymbol{\xi}\rangle$, $\mathbf{b}$ is an externally applied body force, and ρ_0 is the reference material density. This equation expresses conservation of linear momentum. Angular momentum is conserved provided that the material is non-polar and the following constitutive condition holds [98]:

$$\int_{\mathcal{H}(\mathbf{x})} \underline{\mathbf{T}}\langle\boldsymbol{\xi}\rangle \times \underline{\mathbf{Y}}\langle\boldsymbol{\xi}\rangle \, d\boldsymbol{\xi} = \mathbf{0}, \quad \forall \mathbf{x} \in \mathcal{B}_0. \tag{2.5}$$

A derivation of the peridynamic equations of motion based on the standard virtual power assumption is provided in A.1.

	Peridynamics	Classical Continuum
Deformation Measure	$\underline{\mathbf{Y}}$	$\mathbf{F}$
Conjugate Force	$\underline{\mathbf{T}}$	$\mathbf{P}$
Internal Power	$\underline{\mathbf{T}} \bullet \dot{\underline{\mathbf{Y}}}$	$\mathbf{P} : \dot{\mathbf{F}}$
Linear Momentum	$\rho_0 \ddot{\mathbf{y}} = \int_{\mathcal{H}} \underline{\mathbf{T}}\langle \boldsymbol{\xi} \rangle - \underline{\mathbf{T}}'\langle -\boldsymbol{\xi} \rangle \, d\boldsymbol{\xi}$	$\rho_0 \ddot{\mathbf{y}} = \nabla \cdot \mathbf{P}$
Angular Momentum	$\mathbf{0} = \int_{\mathcal{H}} \underline{\mathbf{T}}\langle \boldsymbol{\xi} \rangle \times \underline{\mathbf{Y}}\langle \boldsymbol{\xi} \rangle \, d\boldsymbol{\xi}$	$\mathbf{P}\mathbf{F}^T = \mathbf{F}\mathbf{P}^T$
Elastic Material	$\underline{\bar{\mathbf{T}}}(\underline{\mathbf{Y}}) = \bar{\psi}_{,\underline{\mathbf{Y}}}(\underline{\mathbf{Y}})$	$\hat{\mathbf{P}}(\mathbf{F}) = \nabla \hat{\psi}(\mathbf{F})$
Kinematics	$\underline{\mathbf{Y}}\langle \boldsymbol{\xi} \rangle \neq 0, \text{ for } \lvert \boldsymbol{\xi} \rvert \neq 0$	$\det(\mathbf{F}) > 0$

Table 2.1: Analogies between peridynamics and classical continuum mechanics.

The standard constitutive assumption of state-based peridynamics is that the force vector-state is given by a constitutive law $\underline{\bar{\mathbf{T}}}$ of the form:

$$\underline{\mathbf{T}} = \underline{\bar{\mathbf{T}}}\left(\underline{\mathbf{Y}}, \dot{\underline{\mathbf{Y}}}, \underline{\mathbf{q}}, \mathbf{q}\right),$$

where $\mathbf{q}$ are internal field variables such as temperature or damage, and $\underline{\mathbf{q}}$ are internal vector-state field variables.

When formulating new concepts in peridynamics, it is often helpful to focus on its similarities with classical continuum mechanics. Table 2.1 shows the analogies between the two theories, where ψ is the elastic energy density and ∇ is the gradient operator.

What differentiates peridynamics from classical continuum mechanics in an essential way is that the theory is inherently nonlocal in the sense that material points interact through long-range forces represented by the force vector-state $\underline{\mathbf{T}}$, whose bond-wise components $\underline{\mathbf{T}}\langle \boldsymbol{\xi} \rangle$ can be loosly interpreted as a force per unit reference volume-squared at point $\mathbf{x}$ due to interactions with the point $\mathbf{x}'$.

2.2 Constitutive formulations

Within the state-based formulation, two distinct approaches to formulate peridynamic constitutive models have been proposed, the so-called: 1) *constitutive correspondence* framework which uses a nonlocal approximation of the local deformation gradient tensor, $\bar{\mathbf{F}}$, and 2) *ordinary peridynamic materials* in which the elastic energy is formulated in terms of the magnitude of deformed bond lengths. While even more general constitutive models are allowed by the state-based formulation [114], in this thesis we focus exclusively on the constitutive correspondence and ordinary peridynamic formulations.

2.2.1 Constitutive correspondence

One of the original material models proposed for state-based peridynamics is the so-called constitutive correspondence formulation. A peridynamic material model is said to *correspond* to a classical material model when the strain energy density of both the classical and peridynamic material are equal under affine deformations. For this purpose, an approximate deformation gradient $\bar{\mathbf{F}} \in \mathbb{R}^3 \times \mathbb{R}^3$ was introduced [98]:

$$\bar{\mathbf{F}}\left(\underline{\mathbf{Y}}\right) := \left[\int_{\mathcal{H}} \underline{\omega}\left\langle \boldsymbol{\xi} \right\rangle \left(\underline{\mathbf{Y}}\langle \boldsymbol{\xi} \rangle \otimes \boldsymbol{\xi}\right) d\boldsymbol{\xi}\right] \bar{\mathbf{K}}^{-1}, \tag{2.6}$$

where $\underline{\omega}$ is called the influence scalar-state which must satisfy

$$\underline{\omega}\left\langle \boldsymbol{\xi} \right\rangle > 0, \quad \forall \boldsymbol{\xi} \in \mathcal{H},$$

and is assumed in this thesis to be spherical, meaning

$$\underline{\omega}\left\langle \boldsymbol{\xi} \right\rangle = \omega(|\boldsymbol{\xi}|), \tag{2.7}$$

for some influence function ω. The nonlocal shape tensor $\bar{\mathbf{K}} \in \mathbb{R}^3 \times \mathbb{R}^3$ is defined

$$\bar{\mathbf{K}} := \int_{\mathcal{H}} \underline{\omega}\langle \boldsymbol{\xi} \rangle \, (\boldsymbol{\xi} \otimes \boldsymbol{\xi}) \, d\boldsymbol{\xi}. \tag{2.8}$$

It has been shown that the approximate deformation gradient obtained in this way is identical to the classical deformation gradient (i.e., the continuous gradient of the deformation mapping, $\mathbf{F}$) for affine deformations [98]. It can be seen from Equation (2.6) that the constitutive correspondence form of $\bar{\mathbf{F}}$ provides a description of the state of deformation at point $\mathbf{x}$ which is based on a weighted average of the deformation of all the neighboring bonds.

Given a classical constitutive model with strain energy density $\hat{\psi}(\mathbf{F})$, the corresponding peridynamic model has strain energy density:

$$\bar{\psi}(\underline{\mathbf{Y}}) = \hat{\psi}(\bar{\mathbf{F}}(\underline{\mathbf{Y}})). \tag{2.9}$$

The resulting force vector-state for constitutive correspondence, which follows from work conjugacy, is

$$\underline{\mathbf{T}}\langle \boldsymbol{\xi} \rangle = \underline{\omega}\langle \boldsymbol{\xi} \rangle \, \bar{\mathbf{P}} \bar{\mathbf{K}}^{-1} \boldsymbol{\xi}, \tag{2.10}$$

where $\bar{\mathbf{P}} = \mathbf{P}(\bar{\mathbf{F}})$ is the first Piola-Kirchhoff stress tensor obtained from a classical constitutive law as a function of the approximate deformation gradient. This form of the force vector-state leads to a peridynamic formulation which conserves angular momentum provided that the classical constitutive model used is one which ensures conservation of angular momentum and is non-polar. This is the case if the resulting Cauchy stress $\bar{\boldsymbol{\sigma}}$ is symmetric, i.e.,

$$\bar{\boldsymbol{\sigma}} = \bar{J}^{-1} \bar{\mathbf{P}} \, \bar{\mathbf{F}}^T = \bar{\boldsymbol{\sigma}}^T, \quad \bar{J} = \det \bar{\mathbf{F}}. \tag{2.11}$$

2.2.2 Ordinary peridynamic materials

An alternative constitutive modeling approach called ordinary state-based peridynamics was also proposed in [98]. A peridynamic material model $\underline{\hat{\mathbf{Y}}}$ is said to be ordinary if, for all $\underline{\mathbf{Y}} \in \mathcal{V}^3$,

$$\underline{\mathbf{T}}\langle\boldsymbol{\xi}\rangle \times \underline{\mathbf{Y}}\langle\boldsymbol{\xi}\rangle = \mathbf{0}, \forall \boldsymbol{\xi} \in \mathcal{H},$$

where $\underline{\mathbf{T}} = \underline{\hat{\mathbf{T}}}(\underline{\mathbf{Y}})$. This condition simply states that the force vector-state must be parallel to the deformation vector-state, which automatically ensures that the angular momentum constraint, Equation (2.5), is satisfied. For elastic materials, this condition is equivalent to requiring the elastic energy to depend only on the distance between neighboring material points in the deformed configuration (not on angles between deformed material points, for example). While this imposes an added restriction on possible constitutive models, ordinary peridynamic materials have been shown to be capable of modeling nonlocal isotropic elasticity [98], as well as nonlocal isotropic plasticity [40].

While in principal ordinary peridynamic material models can be quite general, in practice they are typically formulated in terms of bond-extensions:

$$\underline{e}\langle\boldsymbol{\xi}\rangle := |\underline{\mathbf{Y}}\langle\boldsymbol{\xi}\rangle| - |\boldsymbol{\xi}|, \tag{2.12}$$

where $\underline{e}$ is called the extension scalar-state. The bond-extension measures the change in distance between material points relative to their initial separation distance in the reference configuration. The original and most common example of an ordinary peridynamics constitutive model, called a linear ordinary elastic solid or a linear

peridynamic solid [98], has a strain energy density of the form:

$$\psi(\underline{\mathbf{Y}}) = \frac{k\theta^2}{2} + \frac{\alpha}{2}\int_{\mathcal{H}} \underline{\tilde{\omega}}\,\langle\boldsymbol{\xi}\rangle\,\underline{e}^{dev}\,\langle\boldsymbol{\xi}\rangle\,\underline{e}^{dev}\,\langle\boldsymbol{\xi}\rangle\; d\boldsymbol{\xi}, \tag{2.13}$$

where the deviatoric extension is defined as

$$\underline{e}^{dev}\,\langle\boldsymbol{\xi}\rangle := \underline{e}\,\langle\boldsymbol{\xi}\rangle - \frac{\theta\,|\boldsymbol{\xi}|}{3},$$

the volumetric dilatation θ is

$$\theta := \frac{3}{\gamma}\int_{\mathcal{H}} \underline{\tilde{\omega}}\,\langle\boldsymbol{\xi}\rangle\,\underline{e}\,\langle\boldsymbol{\xi}\rangle\,|\boldsymbol{\xi}|\; d\boldsymbol{\xi}, \quad \text{with } \gamma := \int_{\mathcal{H}} \underline{\tilde{\omega}}\,\langle\boldsymbol{\xi}\rangle\,\boldsymbol{\xi}\cdot\boldsymbol{\xi}\, d\boldsymbol{\xi},$$

and $\underline{\tilde{\omega}}$ is the standard *spherical* influence function [98], $\underline{\tilde{\omega}}\,\langle\boldsymbol{\xi}\rangle = \tilde{\omega}(|\boldsymbol{\xi}|)$. The force vector-state for a linear ordinary elastic solid is

$$\underline{\mathbf{T}}\,\langle\boldsymbol{\xi}\rangle = \left(\frac{3k\theta}{\gamma}\,|\boldsymbol{\xi}| + \alpha\,\underline{e}^{dev}\,\langle\boldsymbol{\xi}\rangle\right)\underline{\tilde{\omega}}\,\langle\boldsymbol{\xi}\rangle\,\underline{\mathbf{M}}\,\langle\boldsymbol{\xi}\rangle\,, \text{ where } \underline{\mathbf{M}}\,\langle\boldsymbol{\xi}\rangle := \frac{\underline{\mathbf{Y}}\,\langle\boldsymbol{\xi}\rangle}{|\underline{\mathbf{Y}}\,\langle\boldsymbol{\xi}\rangle\,|}. \tag{2.14}$$

For uniform infinitesimal strains, the energy density of an ordinary elastic peridynamic solid is identical to its corresponding classical isotropic elastic solid, provided that the constitutive parameters used are bulk parameter $k = \kappa$, and shear parameter $\alpha = 15\,\mu/\gamma$, where κ and μ are the classical bulk and shear modulus respectively.

2.3 Kinematic constraint

In addition to frame invariance, and the first and seconds laws of thermodynamics (see A.2 for a discussion of the thermodynamics of state-based peridynamics), an additional important physically motivated assumption of general continuum theories is that the deformation mapping $\varphi : \mathcal{B}_0 \to \mathcal{B}_t$ is one-to-one. This means that distinct material points in the reference configuration remain distinct in the deformed

configuration, i.e. material points can never overlap: for $\mathbf{x},\ \mathbf{x}' \in \mathcal{B}_0$: if $\mathbf{x} \neq \mathbf{x}'$, then $\varphi(\mathbf{x}) \neq \varphi(\mathbf{x}')$. As it has been pointed out [98, 97], using the definition of the peridynamic deformation vector-state, Equation (2.1), a necessary condition for the mapping to be one-to-one is[1]

$$\underline{\mathbf{Y}}[\mathbf{x}]\langle\boldsymbol{\xi}\rangle \neq \mathbf{0}, \quad \forall \boldsymbol{\xi} \in \mathcal{H}(\mathbf{x}),\ \boldsymbol{\xi} \neq \mathbf{0},\ \ \forall \mathbf{x} \in \mathcal{B}_0. \tag{2.15}$$

Solutions to the peridynamic equations of motion are valid only if they satisfy this constraint. In practice, this suggests an additional constitutive constraint which ensures solutions to the peridynamic equations of motion naturally satisfy the kinematic constraint. Until now, this consideration has been neglected in peridynamic constitutive modeling.

2.4 Constitutive constraint for preventing matter interpenetration

We propose an additional constitutive assumption which naturally prevents matter interpenetration, namely:

$$\underline{\mathbf{Y}}\langle\boldsymbol{\xi}\rangle \to \mathbf{0}, \quad \text{for some } \boldsymbol{\xi} \in \mathcal{H}(\mathbf{x}) \implies \psi(\underline{\mathbf{Y}}) \to \infty.$$

However, due to the integral nature of the peridynamic theory, strict enforcement of this constraint Equation (2.15) is not possible in general, as violation for a single bond occurs over a region of zero-measure. This suggests a somewhat relaxed constitutive

[1]This condition, Equation (2.15), is not always sufficient as particles which are not within each others' family may be allowed to overlap. This limitation can be alleviated by taking $\delta \to \infty$.

restriction:

$$\underline{\mathbf{Y}}\langle\boldsymbol{\xi}\rangle \to 0, \quad \forall \boldsymbol{\xi} \in \Omega \subset \mathcal{H}(\mathbf{x}) \implies \psi(\underline{\mathbf{Y}}) \to \infty, \tag{2.16}$$

where Ω is some measurable subset of $\mathcal{H}(\mathbf{x})$. We caution that this may not be a sufficiently strong condition in all cases, as even point-wise infinite strain energy densities may still result in finite total strain energy density over the entire body. We do note, however, that Equations (2.9), and (2.13) both fail to satisfy this condition.

This constitutive constraint is analogous to an assumption which is common in classical nonlinear elasticity theories:

$$\det \mathbf{F} \to 0 \implies \psi(\mathbf{F}) \to \infty.$$

Such restrictions, together with the assumption of poly-convexity of the elastic energy, and other technical assumptions have been shown to be sufficient to establish the existence of solutions in non-linear elasticity [47]. We anticipate that constraints of the form Equation (2.16) may similarly play a critical role in the development of existence proofs for nonlinear peridynamic elasticity.

Enforcing the kinematic constraint of peridynamics through the constitutive response plays a fundamental role in later developments in this thesis. For completeness, we also suggest a possible alternative constitutive restriction for the force vector-state:

$$\underline{\mathbf{Y}}\langle\boldsymbol{\xi}\rangle \to \mathbf{0} \implies \underline{\mathbf{T}}\langle\boldsymbol{\xi}\rangle \cdot \underline{\mathbf{Y}}\langle\boldsymbol{\xi}\rangle \to -\infty.$$

This condition is in a sense more general as it does not require the existence of an elastic energy. It is analogous to the classical condition: $\det \mathbf{F} \to 0 \implies P \to \infty$, where P is the pressure.

Chapter 3

Numerical discretizations of peridynamics

In this chapter, we discuss various discretization approaches for state-based peridynamics and examine their potential limitations. Specifically, we review the particle discretization of constitutive correspondence proposed in [52], and demonstrate the existence of instabilities using this approach. Numerical instabilities are common to many particle-based discretizations of continuum mechanics [90, 9]. We argue that the instabilities observed here are not solely due to the particle nature of the discretization, but actually indicate the presence of zero-energy mode instabilities in the theory itself (which are described analytically in Chapter 4). In order to confirm that these instabilities are indeed due to the theory and not the discretization, we introduce a novel finite element discretization of state-based peridynamics which allows for full integration of the weak form (energy) so that numerical zero-energy modes can be alleviated. However, even with this fully integrated finite element formulation, instabilities continue to manifest themselves for discretizations of the constitutive correspondence formulation. On the other hand, it will also be shown that these instabilities do not arise in finite element discretizations of ordinary peri-

dynamics materials (see Section 2.2.2), indicating that it is a failing of the particular formulation of constitutive correspondence, and not the discretization approach or the general peridynamic theory itself.

3.1 Particle discretization

A straightforward and natural discretization approach for peridynamics which results in a particle method was proposed in [52]. In this approach, the initial configuration of the problem domain is discretized into a set of N particles which represent the volume of the Voronoi cells. Displacement degrees of freedom and other field and internal variable data are associated with each particle, which in effect implies a piecewise-constant interpolation supported on the Voronoi diagram. Particles located at $\mathbf{x}_i \in \mathcal{B}_0$ in the reference configuration map to positions $\mathbf{y}_i \in \mathcal{B}_t$ in the deformed configuration at time t. Integrals in the peridynamic formulation are naturally discretized as volume-weighted sums over the Voronoi cells.

We begin by investigating the constitutive correspondence formulation, as its discretization is now relatively common [51, 52, 21, 69]. Thus, for the constitutive correspondence formulation, the nonlocal deformation gradient is obtained from Equation (2.6) as

$$\bar{\mathbf{F}}_j = \sum_{i=1}^{N} V_i \, \omega(|\mathbf{x}_i - \mathbf{x}_j|) \left(\mathbf{y}_i - \mathbf{y}_j\right) \otimes \left(\mathbf{x}_i - \mathbf{x}_j\right) \bar{\mathbf{K}}_j^{-1},$$

$$\bar{\mathbf{K}}_j = \sum_{i=1}^{N} V_i \, \omega(|\mathbf{x}_i - \mathbf{x}_j|) \left(\mathbf{x}_i - \mathbf{x}_j\right) \otimes \left(\mathbf{x}_i - \mathbf{x}_j\right),$$

where V_i is the volume represented by particle i. The stress and internal state corresponding to this state of deformation is computed for each particle by direct applica-

tion of the classical constitutive update $\bar{\mathbf{P}}_j(\bar{\mathbf{F}}_j, \mathbf{q}_j)$. Integrating the force state (2.10) and replacing in (2.4) leads to the following semi-discrete equations of motion:

$$\rho_0 \ddot{\mathbf{y}}_j = \sum_{i=1}^{N} V_i \, \omega(|\mathbf{x}_j - \mathbf{x}_i|) \left\{ \bar{\mathbf{P}}_i \bar{\mathbf{K}}_i^{-1} (\mathbf{x}_j - \mathbf{x}_i) - \bar{\mathbf{P}}_j \bar{\mathbf{K}}_j^{-1} (\mathbf{x}_i - \mathbf{x}_j) \right\}.$$

These equations of motion are integrated in time using the Newmark time stepping algorithm, with Newmark parameters chosen for explicit time integration and second order accuracy [107], $\beta = 0$ and $\gamma = \frac{1}{2}$.

The resulting method can be interpreted as a nodally based "meshless" discretization of continuum mechanics. Such discretization approaches are known to exhibit zero-energy mode instabilities [90, 9] and similar instabilities have been reported in numerical implementations of the peridynamic correspondence formulation [21, 81]. Despite the potential limitations, this approach has previously been successfully used to model viscoplastic behavior [52], as well as ductile fracture [51, 69] (see also Chapter 7). In order to validate our implementation of the peridynamic particle discretization we simulate the Taylor impact test, which has become a standard benchmark for computational approaches to viscoplasticity.

3.1.1 Validation using a Taylor impact test

The Taylor impact test [30] has been extensively used for characterizing the dynamic plastic response of materials as well as for validating numerical methods, e.g. [49, 42]. The test consists of a cylindrical metallic bar impacting a rigid wall at a high velocity. In the case of peridynamics, a Taylor impact test has been used to demonstrate a numerical implementation of the state-based formulation without damage [52]. This test consisted of a 0.0324 m long 6061-T6 aluminum cylinder with a diameter of 0.00635 m impacting a rigid wall at 363 m/s. Instead of using this test, we chose to adopt the specific configuration of the numerical test presented in [42] in order to

Properties	Values
Initial density	8930 kg/m^3
Bulk modulus	1.3×10^{11} N/m^2
Shear modulus	4.3×10^{10} N/m^2
Initial yield stress	4.0×10^{8} N/m^2
Linear hardening modulus	1.0×10^{8} N/m^2

Table 3.1: Material properties used in Taylor impact test simulations.

compare with alternative discretization approaches from the literature [1, 123, 35, 4]. In this case, the cylinder material is copper, which is modeled as elastic-plastic with linear isotropic hardening. The cylinder length is $l = 0.0324$ m and its radius $r = 0.0032$ m. The impact velocity is 227 m/s. The material properties of the cylinder are shown in Table 3.1. Three different discretizations of 2394 (D1), 16929 (D2) and 130536 (D3) peridynamic particles are used in calculations. Similarly to the approach in [52], for each discretization the horizon size, δ, was chosen to be $3.01 \cdot \Delta x$, where Δx is the approximate average distance between neighboring discrete particles.

The final configurations of the bar and contours of equivalent plastic strain are shown in Figure 3-1. The final radius of the impacting face of the cylinder r_{max}, the cylinder length l_f, and the maximum equivalent plastic strain ϵ^p_{max} are compared to results obtained with finite element calculations [1, 123, 35] and the optimal-transportation method (OTM) [4] in Table 3.2. With the exception of the results computed by means of the OTM method, the other calculations used for comparison were carried out in axisymmetric mode. It can be seen that the peridynamic simulation results compare reasonably well with results obtained using other numerical methods. These computational results provide an initial verification of the theory, the discretization method, and its computer implementation. However, in the following, we demonstrate a few simple cases in which the peridynamic particle discretization approach appears to break down and exhibit instabilities.

Figure 3-1: Simulated final configurations of a Taylor impact test for discretizations D1 (left), D2 (center), and D3 (right).

	l_f (mm)	r_{max} (mm)	ϵ^p_{max}
Kamoulakos [1]	22	7.0-7.1	2.5-3.2
Zhu and Cescotto [123]	21	6.9-7.2	2.5-3.2
Camacho and Ortiz [35]	21	7.2	3.0-3.0
Li et al. [4]	21	6.8	3.0
Peridynamics, D1	22	7.1	2.7
Peridynamics, D2	21	7.5	2.9
Peridynamics, D3	21	7.4	3.3

Table 3.2: Comparison of Taylor impact test using different numerical methods.

3.1.2 Numerical instabilities in constitutive correspondence

Instabilities resulting from peridynamic discretizations have previously been reported in [21], where it was suggested that they can be alleviated using a numerical stabilization approach. Here we expand on this observation, and highlight some cases in which instabilities occurs, as a means of diagnosing and resolving this issue.

Again using the discretization approach described above, we return to the simulation of the Taylor impact test in Section 3.1.1, where reasonable accuracy was found using a fixed peridynamic horizon length to discretization size ratio δ/h. However, for δ/h sufficiently small or large, instabilities emerge, as are demonstrated in Figure 3-2. Figure 3-2 (left) shows that for very small horizon sizes (relative to the discretization length scale) instabilities may occur. This can be readily explained by the fact that for small horizon sizes, it is possible that an insufficient number of particles fall within the peridynamic horizon δ; for instance, it is impossible to form a full rank discrete $\bar{\mathbf{F}}$ if there are less than 3 neighboring particles. For a peridynamic horizon of roughly 3 times the typical element size as shown in Figure 3-2 (middle), the approach enters a regime where the solution is stable and has accuracy commiserate with other discretization approaches (as shown in Section 3.1.1). However, Figure 3-2 (right) indicates that as the horizon size is further increased, instabilities again emerges. This is evidence of a zero-energy mode instability, similar to what has been observed numerically in [21, 81], and which will be shown to exist analytically (i.e., in the peridynamic theory itself) in Chapter 4.

Zero-energy mode instabilities are common to many particle based continuum discretizations [90, 9] and ultimately result from under-integration of the weak form. A common explanation for this type of instability is that smaller wavelength deformation modes are unable to be fully integrated, leading to high frequency, small wavelength numerical instabilities. Adding more particles to the discretization does not alleviate this issue, as expanding the solution space allows for ever smaller wave-

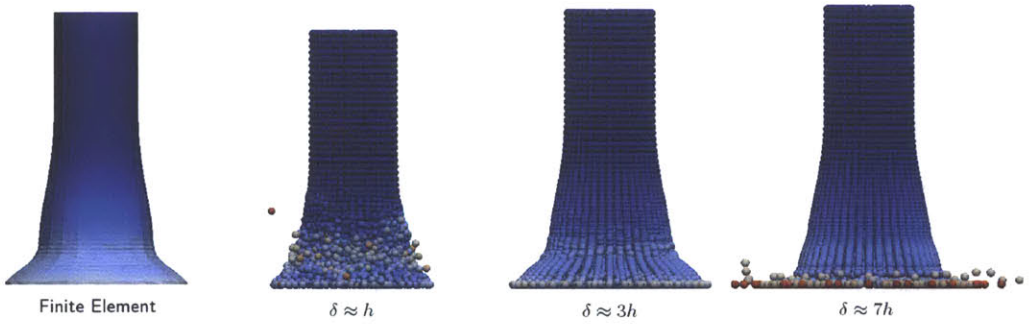

Figure 3-2: Instabilities in Taylor impact for varying peridynamic horizon size and a fixed discretization size.

lengths to be resolved which, in turn, are not properly integrated by the numerical scheme. The most straightforward approach to resolve this issue is to improve the background quadrature rule by adding integration points which do not contribute to the displacement field approximation. In this way, the small length-scale energy modes can be fully integrated for any given discretization size.

In order to investigate the presence of zero-energy modes in a more controlled setting, we propose the use of a finite element discretization of peridynamics, which is derived below. The particle discretization assumes that field variables are piece-wise constant over the Voronoi cells, which renders it effectively an under-integrated discontinuous Galerkin (DG) discretization with piece-wise linear shape functions. In this sense, a DG finite element approach can be viewed as a natural extension of the particle approach to more general quadrature rules and field approximants.

3.2 Ruling out numerical instabilities: finite element discretization

We propose a general discretization approach for state-based peridynamics which is based on standard field approximants (e.g., finite elements) and quadrature rules. Finite element discretizations of peridynamics have been previously proposed [24, 89, 119], though they have been limited to bond-based peridynamic constitutive models (typically linear). Our approach can be viewed as a generalization of the approach proposed in [119] (where both continuous Galerkin and discontinuous Galerkin discretizations were presented for 1D bond-based peridynamics) to the case of state-based peridynamics in higher dimensions.

We approximate the 3D deformation field by $3N$ deformation degrees of freedom $\mathbf{y}_a \in \mathbb{R}^3$, and N global shape functions N_a (for $a = 1, ..., N$) as:

$$\mathbf{y}^h(\mathbf{x}) = \sum_{a=1}^{N} N_a(\mathbf{x})\, \mathbf{y}_a,$$

where the partition of unity requires the ability to exactly represent rigid body modes: $\sum_a N_a(\mathbf{x}) = 1$, for all $\mathbf{x} \in \mathcal{B}_0$. Integration over the reference body is approximated via a quadrature rule in which the integrals are replaced by a sums over quadrature points $\mathbf{x}_q$ with weights w_q as

$$\int_{\mathcal{B}_0} f(\mathbf{x})\, d\mathbf{x} \approx \sum_q w_q\, f(\mathbf{x}_q).$$

Here we derive the equations of motion using a standard Galerkin procedure, where we introduce a test function $\mathbf{v}(\mathbf{x})$ and integrate against the strong form, Equation (2.4), to obtain the weak form of the state-based peridynamic equations of mo-

tion:

$$\int_{\mathcal{B}_0} \left[\rho_0(\mathbf{x})\, \ddot{\mathbf{y}}(\mathbf{x}) - \int_{\mathcal{H}(\mathbf{x})} \Big(\underline{\mathbf{T}}\left[\mathbf{x}\right] \langle \boldsymbol{\xi} \rangle - \underline{\mathbf{T}}\left[\mathbf{x}+\boldsymbol{\xi}\right] \langle -\boldsymbol{\xi} \rangle \Big)\, d\boldsymbol{\xi} \right] \cdot \mathbf{v}(\mathbf{x})\ d\mathbf{x} = 0,$$

where for simplicity we leave out the body force $\mathbf{b}$, as its discretization is standard. The corresponding discretized weak form is

$$\sum_q w_q \left(\rho_0(\mathbf{x}_q) \sum_b \ddot{\mathbf{y}}_b N_b(\mathbf{x}_q) - \sum_r w_r \Big(\underline{\mathbf{T}}^h\left[\mathbf{x}_q\right] \langle \mathbf{x}_r - \mathbf{x}_q \rangle - \underline{\mathbf{T}}^h\left[\mathbf{x}_r\right] \langle \mathbf{x}_q - \mathbf{x}_r \rangle \Big) \right) \cdot \sum_a \mathbf{v}_a N_a(\mathbf{x}_q) = 0, \tag{3.1}$$

which we require to hold for all $\mathbf{v}_a$ and leads to the semi-discrete equations of motion:

$$\ddot{\mathbf{y}}_{bi} = \mathbf{M}^{-1}_{ab} \mathbf{f}_{ai},$$

where the standard symmetric mass matrix $\mathbf{M}$ has components

$$\mathbf{M}_{ab} = \sum_q w_q\, \rho_0(\mathbf{x}_q)\, N_b(\mathbf{x}_q)\, N_a(\mathbf{x}_q),$$

and the nodal forces are

$$\mathbf{f}_a = \sum_q \sum_r \Big(\underline{\mathbf{T}}^h\left[\mathbf{x}_q\right] \langle \mathbf{x}_r - \mathbf{x}_q \rangle - \underline{\mathbf{T}}^h\left[\mathbf{x}_r\right] \langle \mathbf{x}_q - \mathbf{x}_r \rangle \Big) w_q\, w_r\, N_a(\mathbf{x}_q).$$

To complete the formulation it is necessary to provide a discretized constitutive law $\underline{\mathbf{T}}^h = \bar{\underline{\mathbf{T}}}^h \left(\underline{\mathbf{Y}}^h \right)$ for the force vector-state, where the shape function approximation implies a discrete deformation vector-state of

$$\underline{\mathbf{Y}}^h\left[\mathbf{x}\right] \langle \mathbf{x}' - \mathbf{x} \rangle = \sum_a \mathbf{y}_a \big(N_a(\mathbf{x}') - N_a(\mathbf{x}) \big).$$

We use the term discretized constitutive law to emphasize that $\underline{\bar{\mathbf{T}}}^h\left(\underline{\mathbf{Y}}^h\right)$ is itself a discretized functional, requiring integrals over the peridynamic horizon which must be evaluated using a quadrature rule. If the same quadrature rule is used for both the integration over the body and integration over the peridynamic horizon, such a discretization approach is variational for elastic peridynamic materials in the sense that the nodal forces $\mathbf{f}_a$ are work conjugate to the nodal deformations $\mathbf{y}_a$.

To show this we first assume that the discrete elastic (potential) energy V^h for the entire body is of the form

$$V^h = \sum_q w_q \, \psi^h\left(\underline{\mathbf{Y}}^h\left[\mathbf{x}_q\right]\right),$$

where the weights w_q and location $\mathbf{x}_q$ fully define the quadrature rule, then the work conjugate nodal forces are

$$\begin{aligned}
\mathbf{f}_a^{\text{wc}} &= -\sum_q w_q \frac{\partial \psi_q^h\left(\underline{\mathbf{Y}}^h\left[\mathbf{x}_q\right]\right)}{\partial \mathbf{y}_a} \\
&= -\sum_q w_q \int_{\mathcal{B}_0} \psi_{q,\underline{\mathbf{Y}}}^h\langle\boldsymbol{\xi}\rangle \, \frac{d\,\underline{\mathbf{Y}}^h[\mathbf{x}_q]\langle\boldsymbol{\xi}\rangle}{d\mathbf{y}_a} \, d\boldsymbol{\xi} \\
&= -\sum_q w_q \int_{\mathcal{B}_0} \underline{\mathbf{T}}^h\left[\mathbf{x}_q\right]\langle\mathbf{x}_r - \mathbf{x}_q\rangle\left\{N(\mathbf{x}_r) - N(\mathbf{x}_q)\right\} d\mathbf{x}_r
\end{aligned}$$

If we assume that the constitutive law functional uses the same quadrature rule as the one used for integrating the weak form, we find

$$\begin{aligned}
\mathbf{f}_a^{\text{wc}} &= -\sum_q \sum_r w_q \, w_r \, \underline{\mathbf{T}}^h\left[\mathbf{x}_q\right]\langle\mathbf{x}_r - \mathbf{x}_q\rangle\left\{N(\mathbf{x}_r) - N(\mathbf{x}_q)\right\} \\
&= \sum_q \sum_r w_q \, w_r \, \left(\underline{\mathbf{T}}^h\left[\mathbf{x}_q\right]\langle\mathbf{x}_r - \mathbf{x}_q\rangle - \underline{\mathbf{T}}^h\left[\mathbf{x}_r\right]\langle\mathbf{x}_q - \mathbf{x}_r\rangle\right) N(\mathbf{x}_q) = \mathbf{f}_a,
\end{aligned}$$

meaning that the discretization approach based on the weak form (3.1) is variational for elastic peridynamic constitutive laws.

A mass lumping scheme is used in simulations instead of the consistent mass matrix, as is common for finite element discretizations with explicit dynamic time integration. While more generally time integrators are possible, we typically use the Newmark time stepping algorithm, with Newmark parameters chosen for explicit time integration and second order accuracy [107], $\beta = 0$ and $\gamma = \frac{1}{2}$.

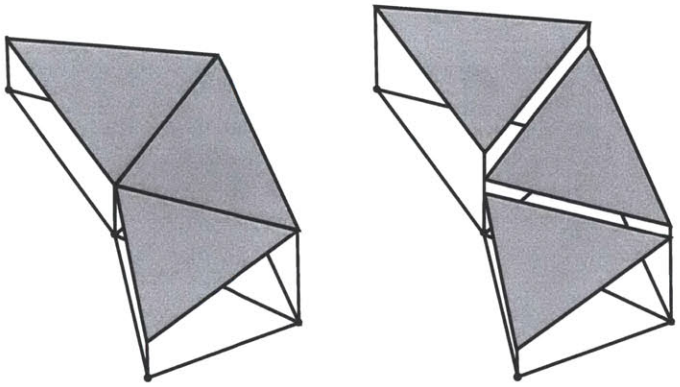

Figure 3-3: Schematic of continuous Galerkin (left) and discontinuous Galerkin (right) approximants.

We point out that up to this point we have not chosen a specific field approximant. Additionally, we note that there are no field gradients in the formulation of peridynamics, which means that no integration by parts is necessary when deriving the discretized equations of motion. This seemingly benign observation has an important implication for peridynamic discretizations using discontinuous Galerkin elements (see Figure 3-3), which is that no interface element integration terms arise. Inter-element compatibility is handled solely by the nonlocal peridynamic force interactions as there are no flux terms across element interfaces. Discontinuities can naturally arise without the need for any additional discretization considerations. This means that discontinuous Galerkin finite-elements based discretizations are a natural choice for peridynamics, as both the interpolation and formulation allow for the possibility of jumps in the deformation field from the onset.

3.2.1 Finite element discretizations of constitutive correspondence: instabilities persist

In this section, we investigate the stability behavior of finite element discretizations of state-based peridynamics using a few simple examples. For simplicity, we restrict attention to 2D discretizations based on linear triangular finite element interpolants (with nodal unknowns at the corners of the triangles), and consider both continuous Galerkin (CG) and discontinuous Galerkin (DG) discretizations (see Figure 3-3).[1] In order to fully alleviate the possibility of numerical zero-energy modes, we use a Gaussian quadrature rule over each triangular element which is capable of exactly integrating 5^{th} order polynomials even though the interpolation is piece-wise linear. This higher order quadrature rule is chosen to be sufficient to fully integrate the linear peridynamic constitutive theories, recalling that a (possibly nonlinear) double integral is required to compute the total elastic energy of a peridynamic body.

The example we consider consists of a 2D peridynamic bar of length $L = 0.2\text{m}$ and height $h = 0.2\text{m}$. For simplicity we fix the peridynamic horizon size at $\delta = 0.02\text{m}$ throughout. The boundary conditions are such that the bar is fully constrained over a region of one horizon length δ on the left end (i.e., $u(x) = 0$ for $x < \delta$), and we apply a uniform body force of a region on the right end ($b(x) = \bar{b}$ for $x > L - \delta$). We assume that the material behavior is a constitutive correspondence material (Section 2.2.1) with a classical constitutive law corresponding to a neo-Hookean material extended to the compressible range, with strain energy density:

$$\psi = \left(\frac{\lambda}{2}\log J - \mu\right)\log J + \frac{\mu}{2}(I_1 - 3)\ ,$$

where λ and μ are the Lamé constants, $J = \det(\mathbf{F})$, and $I_1 = \text{tr}(\mathbf{C})$ for $\mathbf{F} = \nabla_0\boldsymbol{\varphi}$ and $\mathbf{C} = \mathbf{F}^{\text{T}}\mathbf{F}$. This constitutive behavior has the important property that as $J \to 0$,

[1] See, for example, [113] for more on CG discretizations of classical mechanics and [111, 71, 72] for more on DG discretizations of classical mechanics.

$\psi \to \infty$, meaning it has an equation of state behavior sufficient to prevent material collapse. The Lamé constants used are $\lambda = 1.0$ and $\mu = 0.3$ (the properties were chosen essentially arbitrarily, as this is only meant as a demonstration of the stability behavior and need not be physically realistic). The constitutive behavior is elastic, so we can solve the static problem via energy minimization. We use a conjugate gradient optimization routine [91] to minimize the discrete elastic energy over all possible nodal displacements subject to the imposed constraints.

The resulting static solution using a continuous Galerkin mesh is shown in Figure 3-4, with varying applied body forces. The corresponding results using a discontinuous Galerkin mesh is shown in Figure 3-5, but with lower applied body forces. These solution results clearly indicate instabilities in the approach. For the CG finite element case, the instabilities start out as relatively minor, but continue to grow unabated for larger applied loads. The DG case is *highly* unstable from the outset, possible due to the proliferation of degrees of freedom inherent in the DG approach.

It is reasonably to question whether these results may simply be due to a poor implementation, or a misinterpretation of the formulation. We do not believe that this is the case, as we provide physically reasonable results based on an alternative constitutive formulation of peridynamics in Section 3.2.2 using the exact same discretization approach. The extreme instability of the DG approach may seem surprising at first, as it is simply a generalization of the relatively successful particle discretization (which exhibits instabilities, but not nearly as severe as observed here). Indeed, at the outset, we expected that a DG discretization (as compared to CG finite elements) would be closer to the true solution of peridynamics where discontinuities are allowed. We even carefully chose a classical constitutive model with equation of state behavior sufficient to prevent matter interpenetration to rule out the macroscopic constitutive behavior as a possible cause of instability. Having ruled out both the discretization and the macroscopic constitutive behavior as possible causes of instability, the only remaining

plausible explanation for these observations is that there are instabilities inherent to the constitutive correspondence theory of peridynamics. This conclusion is consistent with the analytic results presented in Chapter 4, which show the existence of deformation modes which are not detectable by the nonlocal deformation gradient $\bar{\mathbf{F}}$. In fact, we speculate that the relative success of the standard particle discretizations is due to under-integration of the unstable energy modes, i.e. increased quadrature in this case leads to improved integration of unstable modes which might otherwise have gone undetected!

3.2.2 Finite element discretizations of linear ordinary solids: instabilities suppressed

In the previous section, it was suggested that by over-integrating the weak form of the peridynamic equations of motion, the numerical zero-energy instabilities can be eliminated. It was then shown using a simple numerical example that zero-energy modes are still present. This apparent contradiction makes it essential for us to ensure that these instabilities are not a result of the discretization process, or from errors in the implementation. Towards this end, and to illustrate the viability of finite element approaches for state-based peridynamics, we provide a simple example using an alternative peridynamic constitutive law. Specifically, we use the identical discretization approach, problem set up, and optimization solver from Section 3.2.1, but model the material behavior as a linear (isotropic) peridynamic solid[98, 97] (see Equation (5.2) in Section 2.2.2 with $m = 1/2$). The material constants used in this 2D case are $\bar{\lambda} = 1$ and $\bar{\mu} = 0.5$. Figure 3-6 depicts the static solution using a CG finite element mesh with body forces $b = 1$ (left) and $b = 4$ (right), while Figure 3-7 depicts the same results using a DG mesh. These results indicate that finite element discretizations of peridynamics are stable and do no exhibit zero-energy modes, provided that the an appropriate peridynamic constitutive model is

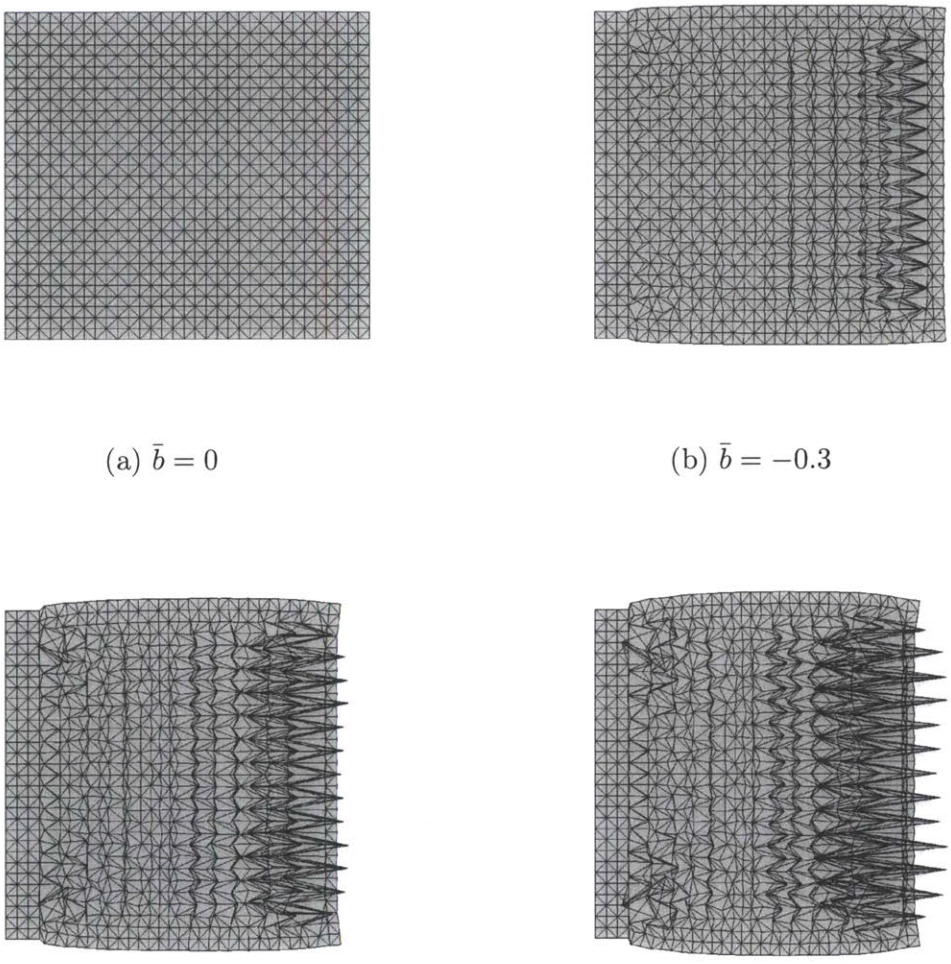

(a) $\bar{b} = 0$

(b) $\bar{b} = -0.3$

(c) $\bar{b} = -0.6$

(d) $\bar{b} = -0.9$

Figure 3-4: Static solution for constitutive correspondence using a CG mesh, where $\bar{b}$ is the applied body force on the right side of the specimen.

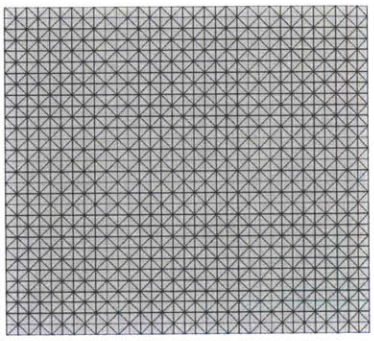

(a) $\bar{b} = 0$

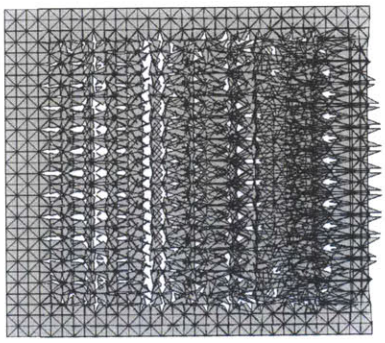

(b) $\bar{b} = -0.02$

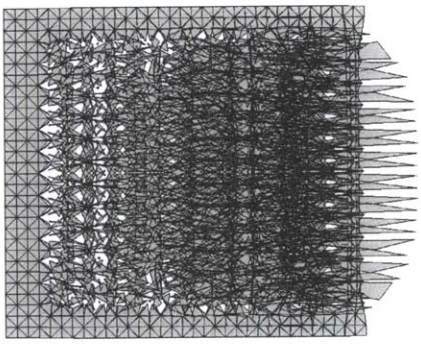

(c) $\bar{b} = -0.04$

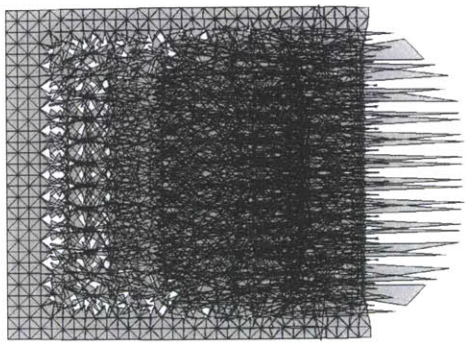

(d) $\bar{b} = -0.06$

Figure 3-5: Static solution for constitutive correspondence using a DG mesh, where $\bar{b}$ is the applied body force on the right side of the specimen.

used.[2] This further suggests that the observed instabilities in Chapter 3.2.1 are due to issues with the theoretical framework of the original *constitutive correspondence* formulation.

3.3 Chapter summary

In this chapter, instabilities in peridynamics discretizations of the constitutive correspondence formulation of peridynamics were found to be prevalent. It was suggested that the problem could be alleviated by fully integrating the peridynamic equations of motion in space using traditional quadrature rules and finite element interpolations. In order to test this idea, we introduced a general finite element discretization approach for state-based peridynamics using both CG and DG finite element interpolations. The discretization approach was shown to be variational for elastic constitutive models, provided that the same quadrature rule was used for both evaluating the constitutive model and for integrating the weak form over the spatial domain. Contrary to our initial motivation for this development, it was found that improved integration led to increased *instability*, an apparent contradiction. We argued that these observed instabilities are a manifestation of the theoretical limitations of constitutive correspondence (which will be investigated in Chapter 4) and that our efforts only provided an improved discretization approach for a theory with inherent instabilities. Finally, to demonstrate the feasibility of the proposed discretization approach using sound peridynamics theories, we provide examples based on the linear theory of ordinary peridynamics (sometimes called a linear peridynamic solid, see Section 2.2.2). These solutions were found to be stable for a fairly wide range of loading conditions. While this alternative constitutive theory appears to fix the instabilities observed

[2]We caution, however, that while this alternative constitutive theory appears to fix the instabilities observed here, it will be shown in Chapter 5 that the linear theory also fails to prevent matter interpenetration under impact conditions. For example, simulations based on the linear ordinary theory of peridynamics are shown to exhibit instabilities in Figure 5-3.

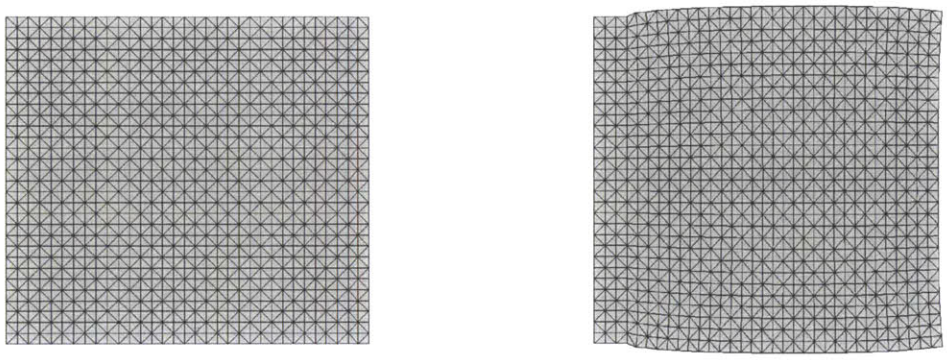

(a) $\bar{b} = 0$

(b) $\bar{b} = -0.2$

(c) $\bar{b} = -0.4$

(d) $\bar{b} = -0.6$

Figure 3-6: Static solution for a linear ordinary elastic solid using a CG mesh, where $\bar{b}$ is the applied body force on the right side of the specimen.

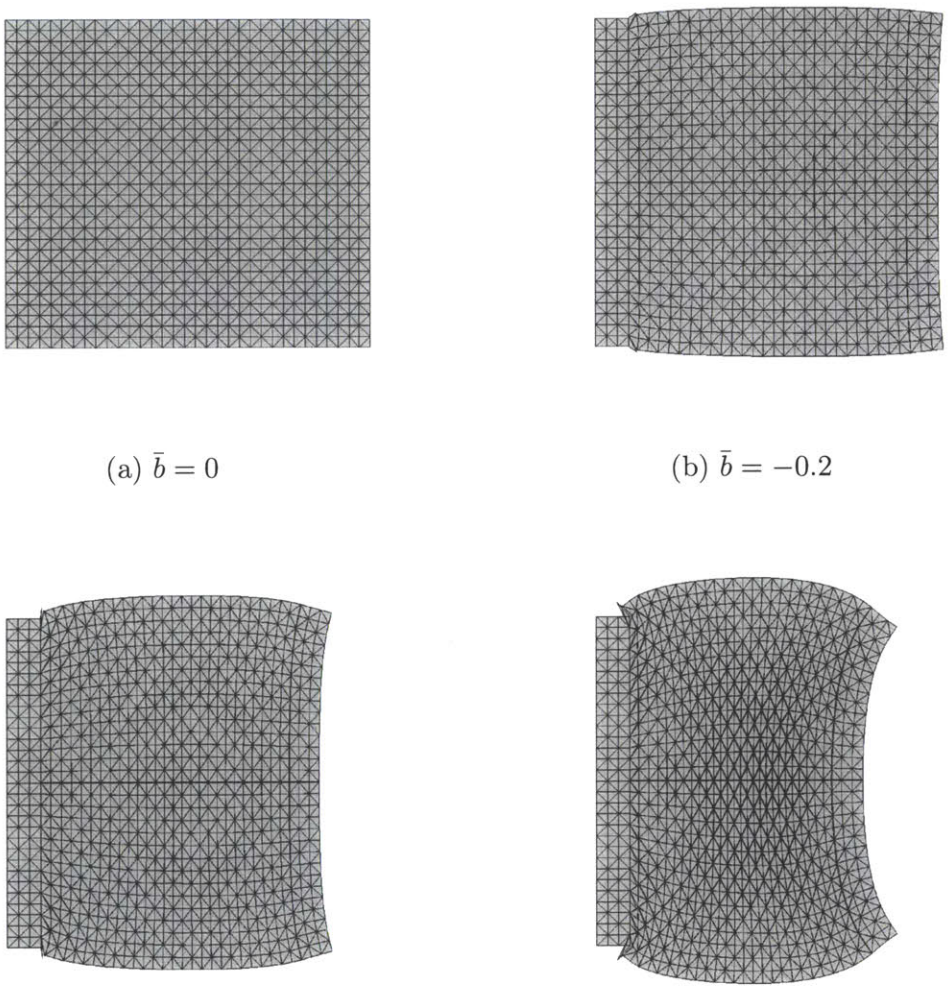

(a) $\bar{b} = 0$

(b) $\bar{b} = -0.2$

(c) $\bar{b} = -0.4$

(d) $\bar{b} = -0.6$

Figure 3-7: Static solution for a linear ordinary elastic solid using a DG mesh, where $\bar{b}$ is the applied body force on the right side of the specimen.

in the simulations conducted here, we caution that the linear theory also allows for unphysical matter interpenetration, as will be discussed in Chapter 5.

Further investigation is still needed to provide insight into the advantages and convergence behavior of the proposed finite element discretization approach.

Chapter 4

An extended constitutive correspondence formulation of peridynamics based on nonlinear bond-strain measures

In this chapter, we propose an *extended constitutive correspondence* formulation of peridynamics which addresses fundamental limitations in the original correspondence theory and generalizes the constitutive framework to models expressed in terms of generalized strain tensors and their work-conjugate stresses. Towards this end, we introduce nonlinear measures of bond elongation which are inherently singular when the matter interpenetration constraint is violated and, thus, avoid unphysical deformations.

As discussed in Section 2.2, two essential peridynamic constitutive modeling frameworks have been proposed: 1) *constitutive correspondence* and 2) *ordinary peridynamic materials*. The constitutive correspondence formulation is particularly appealing as classical nonlinear constitutive models can be incorporated using the nonlocal

approximation of the deformation gradient tensor $\bar{\mathbf{F}}$. For clarify we repeat here Equations (2.6) and (2.8):

$$\bar{\mathbf{F}}\left(\underline{\mathbf{Y}}\right) := \left[\int_{\mathcal{H}} \underline{\omega}\left\langle\boldsymbol{\xi}\right\rangle \left(\underline{\mathbf{Y}}\langle\boldsymbol{\xi}\rangle \otimes \boldsymbol{\xi}\right) d\boldsymbol{\xi}\right] \bar{\mathbf{K}}^{-1},$$

where

$$\bar{\mathbf{K}} := \int_{\mathcal{H}} \underline{\omega}\left\langle\boldsymbol{\xi}\right\rangle \left(\boldsymbol{\xi} \otimes \boldsymbol{\xi}\right) d\boldsymbol{\xi}.$$

In principle, general constitutive laws can be formulated based on nonlocal versions of classical nonlinear strain measures which are computed from this nonlocal $\bar{\mathbf{F}}$. However, it will be shown below that the nonlocal deformation gradient allows for modes of deformation which are physically impossible and yet undetectable by the theory, irrespective of the chosen strain measure. We note that this observation also provides a explanation for the instabilities observed in the computational results in Chapter 3.

To overcome this limitation, the proposed *extended constitutive correspondence* formulation is expressed in terms of generalized nonlocal Seth-Hill strain tensors [13, 82] which are shown to be exact in the uniform infinitesimal limit and which are in turn formulated in terms of corresponding bond-level strain measures. It is also shown that the extended constitutive correspondence framework is *ordinary* and supports general inelastic anisotropic materials models.

In Section 4.1, we provide examples which demonstrate the kinematic deficiency of the original correspondence formulation. Section 4.2 is devoted to the new peridynamic bond-strain measures, the corresponding family of nonlocal strain tensors and their properties, including a demonstration that the new formulation fixes the violation of the matter interpenetration constraint in cases where the original version fails. In Section 4.3, the *extended constitutive correspondence* formulation is then stated and shown to be ordinary. We conclude the chapter with a brief summary in

Section 4.4.

4.1 Limitation in the kinematics of constitutive correspondence

In this section, we investigate a basic fundamental limitation of the kinematic assumption of the constitutive correspondence formulation. Specifically, we demonstrate using several examples how unphysical deformation modes may be undetectable by the nonlocal deformation gradient $\bar{\mathbf{F}}$.

1. **Sub-horizon material collapse**: Consider the extreme situation depicted in Figure 4-1 where a small volume of material $\mathcal{G} \subset \mathcal{B}_0$ collapses to a single point $\mathbf{z} \in \mathcal{B}_t$. The peridynamic deformation vector-state in this case is $\underline{\mathbf{Y}}[\mathbf{x}]\langle\boldsymbol{\xi}\rangle = \mathbf{0}$ for $\mathbf{x}, \mathbf{x}' \in \mathcal{G}$, where $\mathbf{x}' = \mathbf{x} + \boldsymbol{\xi}$. This deformation is clearly unphysical as it violates the matter interpenetration constraint (2.3).

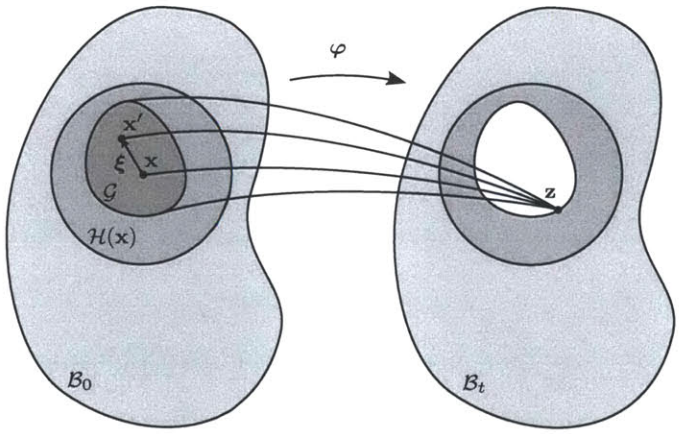

Figure 4-1: Schematic showing a region $\mathcal{G} \subset \mathcal{B}_0$ collapsing to a single point $\mathbf{z} \in \mathcal{B}_t$.

However, it is easy to see that the nonlocal deformation gradient $\bar{\mathbf{F}}(\mathbf{x})$ remains positive-definite at a point $\mathbf{x}$ whose horizon $\mathcal{H}(\mathbf{x})$ contains the collapsed region $\mathcal{G}$, i.e. $\mathcal{G} \subset \mathcal{H}(\mathbf{x})$. In other words, $\bar{\mathbf{F}}$ is unable to detect this localized unphysical deformation, because violating the kinematic constraint (2.3) on the bond-level

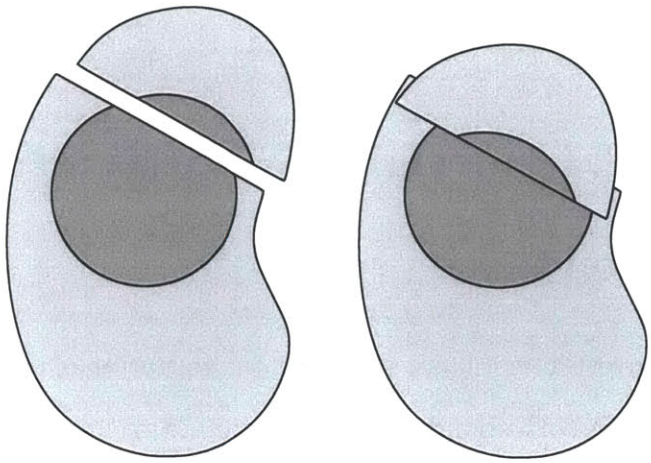

a) opening b) interpenetrating

Figure 4-2: Schematic of surface discontinuities, with both an opening deformation discontinuity (left) and an interpenetrating deformation discontinuity (right).

does not imply that the resulting nonlocal deformation gradient violates the tensor-level kinematic constraint (2.2).

2. **Jump discontinuities in 1D**: Another example consists of a displacement jump discontinuity with a displacement field of $y(x) = a+x$ for $x > 0$ and $y(x) = x$ for $x < 0$. A schematic showing the nature of this discontinuity is shown in Figure 4-2 for $a > 0$ on the left (which is physically acceptable), and $a < 0$ on the right (which is physically impossible). For the opening displacement case, $a > 0$, the nonlocal scalar deformation gradient $\bar{F}(x)$ obtained from the 1D version of Equation (2.6) satisfies the classical kinematic constraint (2.2), with $\bar{F}(x) > 1$ for $|x| < \delta$. This means opening jump displacements are kinematically admissible deformation modes for the constitutive correspondence formulation, as desired.

   However, a value of $a < 0$ which corresponds to unphysical interpenetration (and violates the peridynamic kinematic constraint (2.3)) results in $\bar{F} > 0$ for $|a| \ll \delta$. In other words, the constitutive correspondence formulation admits deformations that are physically inadmissible.

This example highlights an important consideration when formulating peridynamic models: whereas one of the basic premises of peridynamics is that it contemplates the presence of discontinuities in a natural way, it actually goes too far and allows for discontinuities that are unphysical. Based on this consideration we argue that in any valid peridynamic formulation suitable for finite deformations, discontinuities leading to matter interpenetration should be kinematically inadmissible. We have therefore shown that constitutive correspondence, as currently formulated, does not satisfy this criterion.

3. **Zero-energy modes in 1D**: In this example we demonstrate the presence of zero-energy modes[1] in the constitutive correspondence formulation. Consider the 1D case and an influence function of the form $\omega(|x'-x|) = |x'-x|^{-1}$ for $|x'-x| < \delta$. By Equation (2.6) this influence function results in a nonlocal scalar deformation gradient given by:

$$\begin{aligned}\bar{F}(x) &= \frac{1}{\delta^2}\int_{x-\delta}^{x+\delta} \operatorname{sign}(x'-x)(y(x')-y(x))\,dx' \\ &= \frac{1}{\delta^2}\int_{x}^{x+\delta} y(x')-y(x)\,dx' - \frac{1}{\delta^2}\int_{x-\delta}^{x} y(x')-y(x)\,dx' \\ &= \frac{1}{\delta^2}\int_{x}^{x+\delta} y(x')\,dx' - \frac{1}{\delta^2}\int_{x-\delta}^{x} y(x')\,dx'.\end{aligned}$$

For deformations of the form $y(x) = x + a\sin(2\pi kx/\delta + \phi)$, the corresponding

[1]It should be emphasized that here we refer to zero-energy modes that exist in the mathematical formulation of the peridynamics correspondence theory, which should not be confused with those appearing in numerical discretizations. We point out that the issue of zero-energy modes has been observed in numerical discretizations of peridynamics and can be alleviated using numerical stabilization techniques [21].

deformation gradient is

$$\begin{aligned}\bar{F}(x) &= \frac{1}{\delta^2}\int_x^{x+\delta} x' + a\sin\left(2\pi k x'/\delta + \phi\right)\, dx' \\ &\quad - \frac{1}{\delta^2}\int_{x-\delta}^{x} x' + a\sin\left(2\pi k x'/\delta + \phi\right)\, dx' \\ &= \frac{2}{\delta^2}\int_x^{x+\delta} x'\, dx' = 1,\end{aligned}$$

for any integer $k > 0$ and all $a, \phi \in \mathbb{R}$. In other words, there exist periodic deformation mappings for which the nonlocal deformation measure $\bar{F}$ is unable to describe the state of deformation of the material and, thus, they do not contribute to the elastic energy of the material irrespective of the constitutive model.

4. **Vanishing-energy modes in 1D**: A related example demonstrates how more general influence functions allow for the existence of deformation modes with vanishing energy in the short wavelength limit. Consider ω functions which satisfy

$$\int_{\mathcal{H}} \left| \frac{d}{d\xi}\left(\xi\,\omega(|\xi|)\right) \right| d\xi < \infty. \tag{4.1}$$

A deformation of $y(x) = x + a\sin(bx)$ results in

$$\begin{aligned}
\bar{F}(x) &= \frac{1}{\bar{K}(x)} \int_{\mathcal{H}} \omega(|\xi|)\,[y(x+\xi) - y(x)]\,\xi\,d\xi \\
&= 1 + \frac{a}{\bar{K}} \int_{\mathcal{H}} \xi\,\omega(|\xi|)\sin(bx + b\xi)\,d\xi - \frac{a}{\bar{K}} \underbrace{\int_{\mathcal{H}} \xi\,\omega(|\xi|)\,\sin(bx) d\xi}_{0} \\
&= 1 + \frac{a}{\bar{K}} \int_{\mathcal{H}} \xi\,\omega(|\xi|)\cos(bx)\sin(b\xi)\,d\xi \\
&\quad + \frac{a}{\bar{K}} \underbrace{\int_{\mathcal{H}} \xi\,\omega(|\xi|)\cos(b\xi)\sin(bx)\,d\xi}_{0} \\
&= 1 - \frac{a\cos(bx)}{b\bar{K}} \int_{\mathcal{H}} \frac{d}{d\xi}\left(\xi\,\omega(|\xi|)\right)\cos(b\xi)\,d\xi,
\end{aligned}$$

where we've used standard trigonometric identities, the fact that ω is an even function and the last step results from an integration by parts using $\omega = 0$ on $\partial\mathcal{H}$. Taking the limit of vanishingly-small wavelengths by increasing b for fixed oscillation amplitude a gives

$$\lim_{b\to\infty} \left| \frac{a}{b} \int_{\mathcal{H}} \frac{d}{d\xi}\left(\xi\,\omega(|\xi|)\right)\cos(b\xi)\,d\xi \right| \leq \lim_{b\to\infty} \left|\frac{a}{b}\right| \int_{\mathcal{H}} \left| \frac{d}{d\xi}\left(\xi\,\omega(|\xi|)\right) \right| d\xi = 0,$$

and we find $\lim_{b\to\infty} \bar{F}(x) = 1$.

This shows that for sufficiently well behaved influence functions, Equation (4.1), rapidly oscillating displacement fields contribute negligibly to the nonlocal deformation gradient $\bar{\mathbf{F}}$. It should be noted that this example also embodies the case of local matter interpenetration for large values of the amplitude a.

This example has important implications for numerical discretizations of the constitutive correspondence formulation: for a fixed peridynamic horizon size, as the discretization is refined such that high-frequency oscillations become

increasingly resolved within the horizon, additional zero-energy modes emerge, which inevitably leads to instability.

As is known, [21], numerical implementations of peridynamic correspondence formulations are mired with instabilities commonly attributed to artifacts in particle-based discretizations of continuum mechanics [90, 9]. This chapter demonstrates that even when the numerical issues are properly addressed, more fundamental instabilities of a theoretical nature remain in the peridynamic correspondence formulation, as currently stated.

4.2 Finite deformation peridynamic bond-strain measures

In the previous section, we concluded that in the existing constitutive correspondence framework unphysical deformations may result in a kinematically admissible $\bar{\mathbf{F}}$. In other words, violating the kinematic constraint (2.3) on the bond-level does not imply that the resulting nonlocal deformation gradient violates the tensor-level kinematic constraint (2.2), i.e.

$$\underline{\mathbf{Y}}\,[\mathbf{x}]\,\langle\boldsymbol{\xi}\rangle = \mathbf{0} \text{ for some } \boldsymbol{\xi} \in \mathcal{H}(\mathbf{x}) \;\not\Longrightarrow\; \det\left(\bar{\mathbf{F}}(\mathbf{x})\right) \leq 0.$$

The source of this limitation is that $\bar{\mathbf{F}}$ averages the material deformation over the horizon in such a way that localized misbehavior may contribute negligibly or be compensated for elsewhere in the integral. In order to fix this issue, we propose a nonlocal measure of strain which is sensitive to any violation of the bond-level kinematic constraint (2.3).[2] To achieve this, we introduce strain measures on a bond-by-bond basis which have the appropriate kinematic behavior in the fully compressed

[2]The intuition here is that any violation of the matter interpenetration constraint should immediately gives rise to infinities in the integrand for the nonlocal deformation gradient.

limit.

We propose a family of bond-strain measures inspired by the Seth-Hill[3] strain measures [13, 82]:

$$\underline{\varepsilon}_{(m)}\langle\boldsymbol{\xi}\rangle := \frac{1}{2m}\left[\underline{c}\langle\boldsymbol{\xi}\rangle^{m} - 1\right], \tag{4.2}$$

where

$$\underline{c}\langle\boldsymbol{\xi}\rangle := \frac{\underline{\mathbf{Y}}\langle\boldsymbol{\xi}\rangle \cdot \underline{\mathbf{Y}}\langle\boldsymbol{\xi}\rangle}{\boldsymbol{\xi}\cdot\boldsymbol{\xi}},$$

is the Cauchy-Green deformation scalar-state which measures the bond elongation. We call $\underline{\varepsilon}_{(m)}$ the strain scalar-state, which is parameterized by the strain measure parameter m.

For the degenerate case $m = 0$, we obtain:

$$\underline{\varepsilon}_{(0)}\langle\boldsymbol{\xi}\rangle := \frac{1}{2}\log(\underline{c}\langle\boldsymbol{\xi}\rangle),$$

which we define as the logarithmic (also Hencky or true) strain scalar-state. For infinitesimal bond strains all of these measures reduce to the same scalar-state. For $m \leq 0$, these strain measures have the proper kinematic behavior in the fully compressed limit, i.e.

$$\underline{\mathbf{Y}}\langle\boldsymbol{\xi}\rangle \to \mathbf{0} \implies \underline{\varepsilon}_{(m)}\langle\boldsymbol{\xi}\rangle \to -\infty.$$

As a result, these bond-strain measures for $m \leq 0$ naturally allow for the enforcement of non-interpenetration (2.3) on a bond-by-bond basis. This is in contrast to constitutive correspondence, which only allows for an averaged enforcement of the tensorial

[3]Recall the classical Seth-Hill strain tensors, $\mathbf{E}_{(m)} = \frac{1}{2m}(\mathbf{C}^m - \mathbf{1})$, and right Cauchy-Green deformation tensor $\mathbf{C} = \mathbf{F}^T\mathbf{F}$.

kinematic constraint (2.2).

4.2.1 Nonlocal peridynamic strain tensor

In order to use established constitutive models formulated in terms of a strain tensor, it is convenient to formulate a tensorial measure of the nonlocal strain. This is accomplished by defining a nonlocal peridynamic strain tensor $\bar{\mathbf{E}}_{(m)} \in \mathbb{R}^3 \times \mathbb{R}^3$ parametrized by m as

$$\bar{\mathbf{E}}_{(m)} := \int_{\mathcal{H}} \underline{\omega}\,\langle \boldsymbol{\xi} \rangle\; \underline{\varepsilon}_{(m)} \langle \boldsymbol{\xi} \rangle\; \underline{\mathbf{H}}\,\langle \boldsymbol{\xi} \rangle \; d\boldsymbol{\xi}, \tag{4.3}$$

where we define the shape tensor-state $\underline{\mathbf{H}} \in \mathcal{H} \times \mathbb{R}^3 \times \mathbb{R}^3$ by

$$\underline{\mathbf{H}}\,\langle \boldsymbol{\xi} \rangle := \frac{5}{2} \frac{\boldsymbol{\xi} \otimes \boldsymbol{\xi}}{\boldsymbol{\xi} \cdot \boldsymbol{\xi}} - \frac{1}{2}\mathbf{1}, \tag{4.4}$$

and without loss of generality we normalize the influence function in 3D as follows:

$$\int_{\mathcal{H}} \underline{\omega}\,\langle \boldsymbol{\xi} \rangle \, d\boldsymbol{\xi} = 3. \tag{4.5}$$

4.2.2 Properties of the family of nonlocal strain tensors $\bar{\mathbf{E}}_{(m)}$

1. **Correspondence for infinitesimal strains:** The specific forms of (4.4) and (4.5) ensure that the nonlocal strain tensor $\bar{\mathbf{E}}_{(m)}$ reduces to the classical value for infinitesimal uniform strains. This can be shown as follows. Start by noting that in this case $\underline{\varepsilon}_{(m)} \langle \boldsymbol{\xi} \rangle = \epsilon_{ij}\, \xi_i\, \xi_j / |\boldsymbol{\xi}|^2$ for any m, where $\epsilon_{ij} = \frac{1}{2}\left(\frac{\partial u_i}{\partial x_j} + \frac{\partial u_j}{\partial x_i} \right)$ are components of the classical infinitesimal strain tensor. Here we drop the m subscript, as in this limit the strain measures are all identical. Using index notation and the summation convention, the nonlocal strain tensor for uniform

infinitesimal strains is

$$\bar{E}_{ij} = \mathcal{I}_{ijkl}\,\epsilon_{kl} - \mathcal{J}_{kl}\,\epsilon_{kl}\,\delta_{ij},$$

where

$$\mathcal{I}_{ijkl} := \frac{5}{2}\int_{\mathcal{H}} \underline{\omega}\,\langle\boldsymbol{\xi}\rangle\,\frac{\xi_i\xi_j\xi_k\xi_l}{|\boldsymbol{\xi}|^4}\,d\boldsymbol{\xi} \text{ and } \mathcal{J}_{kl} := \frac{1}{2}\int_{\mathcal{H}} \underline{\omega}\,\langle\boldsymbol{\xi}\rangle\,\frac{\xi_k\xi_l}{|\boldsymbol{\xi}|^2}\,d\boldsymbol{\xi}.$$

These integrals can be computed analytically using symmetry arguments and by transforming to spherical coordinates, as in [98].[4] It follows from the symmetry of the influence function (2.7) that terms like $\mathcal{I}_{1112}$, $\mathcal{I}_{1233}$ and $\mathcal{J}_{12}$, where any index appears an odd number of times, are zero. Also by symmetry, $\mathcal{I}_{1122} = \mathcal{I}_{1221} = \mathcal{I}_{2233}$, $\mathcal{I}_{1111} = \mathcal{I}_{2222}$, $\mathcal{J}_{11} = \mathcal{J}_{22}$, etc.

To compute the nonzero terms of $\boldsymbol{\mathcal{J}}$, note that

$$\mathcal{J}_{ii} = \frac{1}{2}\int_{\mathcal{H}} \underline{\omega}\,\langle\boldsymbol{\xi}\rangle\,\frac{\xi_i\xi_i}{|\boldsymbol{\xi}|^2}\,d\boldsymbol{\xi} = \frac{1}{2}\int_{\mathcal{H}} \underline{\omega}\,\langle\boldsymbol{\xi}\rangle\,d\boldsymbol{\xi} = \frac{3}{2},$$

where we have used the normalization constraint (4.5), and therefore

$$\mathcal{J}_{11} = \mathcal{J}_{22} = \mathcal{J}_{33} = \frac{1}{3}\mathcal{J}_{ii} = \frac{1}{2}. \tag{4.6}$$

The nonzero terms of $\boldsymbol{\mathcal{I}}$ can be found by noting that

$$5\,\mathcal{J}_{11} = \frac{5}{2}\int_{\mathcal{H}} \underline{\omega}\,\langle\boldsymbol{\xi}\rangle\,\frac{\xi_1\xi_1|\boldsymbol{\xi}|^2}{|\boldsymbol{\xi}|^4}\,d\boldsymbol{\xi} = \mathcal{I}_{1111} + \mathcal{I}_{1122} + \mathcal{I}_{3311},$$

[4]These calculations are only valid in the interior of the body, far from boundaries.

and

$$\mathcal{I}_{3333} = \frac{5}{2}\int_0^{2\pi}\int_0^{\pi}\int_0^{\delta} \omega(r)\cos^4\phi\,\sin\phi\,r^2\,dr\,d\phi\,d\theta$$
$$= \left(\frac{5}{4}\int_{\mathcal{H}} \underline{\omega}\,\langle\boldsymbol{\xi}\rangle\,d\boldsymbol{\xi}\right)\int_0^{\pi}\cos^4\phi\,\sin\phi\,d\phi = \frac{15}{4}\frac{2}{5},$$

to find

$$\mathcal{I}_{1111} = \mathcal{I}_{2222} = \mathcal{I}_{3333} = \frac{3}{2} \text{ and } \mathcal{I}_{1122} = \mathcal{I}_{2233} = \mathcal{I}_{3311} = \frac{1}{2}.$$

The off-diagonal terms of the nonlocal strain tensor evaluate as

$$\bar{E}_{12} = \bar{E}_{21} = \mathcal{I}_{1212}\,\epsilon_{12} + \mathcal{I}_{1221}\,\epsilon_{21} = \frac{\epsilon_{12}}{2} + \frac{\epsilon_{21}}{2} = \epsilon_{12},$$

and similarly for $\bar{E}_{23}$ and $\bar{E}_{31}$. We find for the diagonal terms that

$$\bar{E}_{11} = \mathcal{I}_{1111}\,\epsilon_{11} + \mathcal{I}_{1122}\,\epsilon_{22} + \mathcal{I}_{1133}\,\epsilon_{33} - \mathcal{J}_{11}\,\epsilon_{11} - \mathcal{J}_{22}\,\epsilon_{22} - \mathcal{J}_{33}\,\epsilon_{33} = \epsilon_{11},$$

and similarly for $\bar{E}_{22}$ and $\bar{E}_{33}$. We conclude that in the limit of uniform infinitesimal strains, the nonlocal strain tensor is identical to the actual (classical) strain tensor, $\bar{\mathbf{E}} = \boldsymbol{\epsilon}$.

2. **Correspondence of the nonlocal log strain tensor for pure dilatation:** In addition to being exact in the limit of infinitesimal strains, we show that for the case $m = 0$, $\bar{\mathbf{E}}_{(0)}$ is exactly the log strain tensor for large uniform volumetric deformations. Consider a uniform volumetric strain with deformation gradient $\mathbf{F} = J^{\frac{1}{3}}\mathbf{R}$, where $\mathbf{R}$ is a rotation vector, $\mathbf{R}\mathbf{R}^T = \mathbf{R}^T\mathbf{R} = \mathbf{1}$, and J represents the volume change between reference and deformed configurations. The actual

log strain tensor $\mathbf{E}_{(0)}$ for this deformation gradient is

$$\mathbf{E}_{(0)} = \frac{1}{2}\log(\mathbf{F}^T\mathbf{F}) = \frac{1}{2}\log(J^{\frac{2}{3}}\mathbf{R}^T\mathbf{R}) = \frac{1}{3}\log(J)\mathbf{1}.$$

For this case, the peridynamic deformation vector-state is:

$$\underline{\mathbf{Y}}\langle\boldsymbol{\xi}\rangle = \mathbf{F}\boldsymbol{\xi} = J^{\frac{1}{3}}\mathbf{R}\boldsymbol{\xi},$$

which results in the log bond-strain:

$$\underline{\varepsilon}_{(0)}\langle\boldsymbol{\xi}\rangle = \log(J^{\frac{1}{3}}) = \frac{1}{3}\log(J), \quad \forall\boldsymbol{\xi} \in \mathcal{H},$$

and the nonlocal strain tensor:

$$\begin{aligned}\bar{\mathbf{E}}_{(0)} &= \frac{1}{3}\log(J)\int_{\mathcal{H}} \underline{\omega}\langle\boldsymbol{\xi}\rangle\left(\frac{5}{2}\frac{\boldsymbol{\xi}\otimes\boldsymbol{\xi}}{\boldsymbol{\xi}\cdot\boldsymbol{\xi}} - \frac{1}{2}\mathbf{1}\right) d\boldsymbol{\xi} \\ &= \frac{1}{3}\log(J)\left(5\,\mathcal{J}_{11}\mathbf{1} - \frac{3}{2}\mathbf{1}\right) \\ &= \frac{1}{3}\log(J)\mathbf{1} = \mathbf{E}_{(0)},\end{aligned}$$

where the integral $\mathcal{J}_{11}$ is given by Equation (4.6).

4.2.3 A fix to the issue of matter interpenetration

We revisit the issue of matter interpenetration and explore how the nonlocal strain tensor in Equation (4.3) behaves for some of the examples described in Section 4.1.

1. **Sub-horizon material collapse:** Consider again Figure 4-1, which depicts a small finite volume of material $\mathcal{G} \subset \mathcal{B}_0$ collapsing to a single point $\mathbf{z} \in \mathcal{B}_t$. For $m \leq 0$, it is easy to see from Equation (4.2) that at a point $\mathbf{x} \in \mathcal{G}$,

$\underline{\varepsilon}_{(m)}[\mathbf{x}]\,\langle\boldsymbol{\xi}\rangle \to -\infty$ for $\mathbf{x}+\boldsymbol{\xi} \in \mathcal{G}$, and therefore

$$\operatorname{tr}\left(\bar{\mathbf{E}}_{(m)}(\mathbf{x})\right) = \int_{\mathcal{H}} \underline{\omega}\langle\boldsymbol{\xi}\rangle\, \underline{\varepsilon}_{(m)}[\mathbf{x}]\,\langle\boldsymbol{\xi}\rangle\, d\boldsymbol{\xi} \to -\infty,$$

which follows from (4.3) provided that $|\underline{\mathbf{Y}}\,\langle\boldsymbol{\xi}\rangle\,| < \infty,\ \forall\boldsymbol{\xi} \in \mathcal{H}$. This shows that if any finite volume $\mathcal{G}$ collapses to a single point, the nonlocal strain tensor $\bar{\mathbf{E}}_{(m)}$ exhibits the expected behavior.

2. **Interpenetrating jump discontinuities in 1D:** In this example, we consider a displacement jump discontinuity with a deformation field of the form $y(x) = x + a$ for $x > 0$ and $y(x) = x$ for $x < 0$. The nonlocal strain in 1D is

$$\begin{aligned}\bar{E}_{(m)}(x) :=& \int_{\mathcal{H}} \omega(|\xi|)\, \underline{\varepsilon}_{(m)}\,[x]\,\langle\xi\rangle\, d\xi \\ =& \frac{1}{2m}\int_{\mathcal{H}} \omega(|\xi|)\left[\left(\frac{|y(x+\xi)-y(x)|}{|\xi|}\right)^{2m} - 1\right] d\xi,\end{aligned}$$

where in 1D we constrain the influence function by $\int_{\mathcal{H}} \omega(|\xi|)\, d\xi = 1$. We consider the case $a < 0$, $|a| < \delta$, corresponding to a small interpenetrating jump discontinuity. The nonlocal strain at a point $x \le 0$ for $|x| < |a|$ is

$$\begin{aligned}2m\,\bar{E}_{(m)}(x) &= \int_{-x}^{\delta} \omega(\xi)\left(\frac{|\xi+a|}{\xi}\right)^{2m} d\xi - \int_{-x}^{\delta} \omega(\xi)\ d\xi \\ &= \int_{-x}^{-a} \frac{\omega(\xi)}{\xi^{2m}}\,(-\xi-a)^{2m}\ d\xi + \int_{-a}^{\delta} \frac{\omega(\xi)}{\xi^{2m}}\,(\xi+a)^{2m}\ d\xi \\ &\quad - \int_{-x}^{\delta} \omega(\xi)\ d\xi.\end{aligned}$$

This shows that for $m < {}^{-1}/_{2}$, matter interpenetration near surfaces of discontinuity results in an unbounded nonlocal strain scalar, at least in 1D, i.e. $\bar{E}_{(m)}(x) \to -\infty$ for $-|a| < x \le 0$ and by symmetry for $-|a| < x < |a|$.

3. **Opening jump discontinuities in 1D:** In addition, we consider the case

$a > 0$, corresponding to an opening displacement jump discontinuity as would occur in the presence of fracture. In this case, the nonlocal strain tensor at $x \leq 0$, $|x| < \delta$ is

$$2m\,\bar{E}(x) = \int_{-x}^{\delta} \omega(|\xi|) \left(\frac{|\xi + a|}{\xi} \right)^{2m} - \omega(|\xi|)\ d\xi$$
$$< \infty,$$

provided that

$$\omega(|\xi|) < C|\xi|^{2m-1}, \quad \forall \xi \in \mathcal{H}, \text{ for some } C > 0.$$

This example shows that for sufficiently well behaved influence functions, opening fracture-type discontinuities are allowed and result in a finite nonlocal strain scalar.

These previous examples show that use of appropriate bond-strain measures ensures that unphysical deformations are ruled out from the peridynamic theory, i.e. the nonlocal strains become undefined, as expected. This is accomplished without sacrificing the key advantage of peridynamics for problems involving physically admissible discontinuities such as those which occur during fracture.

4.3 Constitutive models based on the nonlocal strain tensor

A straightforward approach for formulating constitutive models in terms of the proposed strain measures is based on the peridynamic correspondence concept: the classical strain energy density function $\hat{\psi}\left(\mathbf{E}_{(m)}\right)$ as originally formulated in terms of a classical strain tensor $\mathbf{E}_{(m)}$ must be evaluated using the corresponding nonlocal strain

tensor $\bar{\mathbf{E}}_{(m)}$, i.e. $\bar{\psi}(\underline{\mathbf{Y}}) = \hat{\psi}(\bar{\mathbf{E}}_{(m)}(\underline{\mathbf{Y}}))$. The work-conjugate stress measure then follows as:

$$\bar{\boldsymbol{\sigma}}_{(m)} := \hat{\boldsymbol{\sigma}}\left(\bar{\mathbf{E}}_{(m)}\right) = \nabla\hat{\psi}\left(\bar{\mathbf{E}}_{(m)}\right).$$

Finally, the peridynamic force vector-state follows from work conjugacy and using Equations (4.2), (4.3) and (4.4) as:

$$\begin{aligned}
\underline{\mathbf{T}}_{(m)}\langle\boldsymbol{\xi}\rangle &= \bar{\psi}_{,\underline{\mathbf{Y}}}\langle\boldsymbol{\xi}\rangle\left(\bar{\mathbf{E}}_{(m)}(\underline{\mathbf{Y}})\right) \\
&= \nabla\hat{\psi}\left(\bar{\mathbf{E}}_{(m)}\right) : \bar{\mathbf{E}}_{(m),\underline{\mathbf{Y}}}\langle\boldsymbol{\xi}\rangle \\
&= \left(\bar{\boldsymbol{\sigma}}_{(m)} : \underline{\mathbf{H}}\langle\boldsymbol{\xi}\rangle\right)\underline{\omega}\langle\boldsymbol{\xi}\rangle\,\underline{c}\langle\boldsymbol{\xi}\rangle^{m-1}|\boldsymbol{\xi}|^{-2}\underline{\mathbf{Y}}\langle\boldsymbol{\xi}\rangle\,. \qquad (4.7)
\end{aligned}$$

It should be noted that this extended correspondence formulation generalizes to materials exhibiting anisotropy and inelasticity as long as they are formulated within an internal variable framework. Another important observation is that the resulting material models are *ordinary* (which can be clearly seen by noting that the force vector-state is parallel to the deformation vector-state, i.e. $\underline{\mathbf{T}}\langle\boldsymbol{\xi}\rangle \times \underline{\mathbf{Y}}\langle\boldsymbol{\xi}\rangle = \mathbf{0}$, $\forall\boldsymbol{\xi} \in \mathcal{H}$), and therefore conserve angular momentum. It is also interesting to note that in this correspondence formulation only the symmetric part of the stress tensor contributes to the force vector-state. This follows from (4.7) and the symmetry of $\underline{\mathbf{H}}\langle\boldsymbol{\xi}\rangle$, see Equation (4.4).

In summary, the proposed *extended constitutive correspondence* formulation shares the main features of the original version: it enables the direct use of classical constitutive models and is formulated entirely in terms of integrals of deformation, so that derivatives need not exist and no special treatment is required in the presence of discontinuities. In addition, the new formulation addresses the fundamental issues discussed in Section 4.1: 1) it avoids unphysical deformation modes present in the original formulation by introducing generalized bond-level strain measures, and

2) the formulation is extended in the sense that constitutive models are formulated directly in terms of generalized nonlocal peridynamic strain tensors $\bar{\mathbf{E}}_{(m)}$ and their corresponding work-conjugate stress measures.

4.4 Chapter summary

The ability to naturally handle field discontinuities has previously been put forward as a key advantage of the peridynamic theory over classical continuum theories [98, 97], however, without careful consideration this flexibility may go to far and result in peridynamic formulations in which highly unphysical deformation modes (i.e. matter interpenetration) are allowed. We have shown by way of example that the *constitutive correspondence* framework of peridynamics [98] fails to enforce the kinematic invertibility constraint and thus allows for a variety of unphysical deformation modes including material collapse, matter interpenetrating surfaces of discontinuity and zero-energy modes. To overcome this limitation, the constitutive correspondence framework of peridynamics [98] has been extended to a class of constitutive models which are formulated in terms of generalized nonlocal Seth-Hill strain tensors and their work-conjugate stresses. These nonlocal strain tensors are in turn based on nonlinear bond-strain measures which enforce the kinematic constraint at the individual bond level by design. Several examples are used to show that the modified theory avoids the associated issues of matter interpenetration in cases where the original theory fails. The resulting *extended constitutive correspondence* framework supports general classic constitutive laws as originally intended and is also shown to be *ordinary*.

Chapter 5

Ordinary elastic solids based on nonlinear bond-strain measures

One of the main conclusions of Chapters 3 and 4 was that the existing constitutive correspondence formulation of peridynamics allows for unphysical deformations, irrespective of the classical constitutive model used. To overcome this limitation, an extension of the constitutive correspondence theory based on nonlinear bond-strain measures was proposed in Chapter 4. As an alternative approach to overcome limitations in existing peridynamics constitutive theories, in this chapter we extend the linear theory of ordinary peridynamics (sometimes called a linear peridynamic solid) [98] to nonlinear elastic behavior. This extension is motivated, in part, by the success of finite element discretizations of linear ordinary solids, which were shown in Section 3.2.2 to not exhibit zero-energy modes. However, it will be demonstrated below that this constitutive theory still allows for the possibility of matter interpenetration.

To overcome this limitation, we formulate the ordinary constitutive models directly in terms of the nonlinear bond-strain measures proposed in Section 4.2. By construction, these nonlinear measures of bond elongation are inherently singular when the matter interpenetration constraint is violated and, thus, avoid unphysical

deformations. As a result, the approach naturally furnishes constitutive models with the correct limiting behavior under material collapse, in stark contrast with the standard linear theory [98] where interaction forces remain finite even when the matter interpenetration constraint is violated.

In the following, we derive the proposed nonlinear theory and provide analytic examples which demonstrate its advantages over the existing approach. Specifically, in Section 5.2, concrete analytical examples are provided which demonstrate how the nonlinear version of the theory overcomes limitation of the original linear theory. Numerical results are provided in Section 5.3 using the standard peridynamic particle discretization approach[52, 69]. Specifically, we conduct numerical simulations of a peridynamic analog of the Riemann problem, which serves as a simplified model for the initial stage of ballistic impact events, and provides a good test of the behavior of peridynamic constitutive models and their discretizations under impact conditions. These computational results further highlight the advantage of formulating the constitutive response in terms of nonlinear bond-strain measures and confirm that numerical instabilities are suppressed by the modified theory.

5.1 Nonlinear ordinary elastic solids

We propose a generalized constitutive modeling framework for ordinary peridynamic solids which generalizes the linear ordinary elastic solids approach reviewed in Section 2.2.2. A basic issue with the linear theory is that it suffers from a similar limitation found in infinitesimal elasticity: in the limit when the material is compressed to zero volume ($\underline{\mathbf{Y}}\langle\boldsymbol{\xi}\rangle \to \mathbf{0}$), we have $\underline{e}\langle\boldsymbol{\xi}\rangle \to -|\boldsymbol{\xi}|$, which implies a bond-strain of

$$\underline{\varepsilon}\langle\boldsymbol{\xi}\rangle = \frac{\underline{e}\langle\boldsymbol{\xi}\rangle}{|\boldsymbol{\xi}|} = -1,$$

and, in turn, a finite bond-force (2.14) which is unable to prevent matter interpenetration. The source of the problem is that the deformation measure $\underline{e}$ does not have the appropriate kinematic response under large compression. However, as will be demonstrated below, it is possible to formulate nonlinear ordinary elastic solids in terms of bond-strain measures which do not suffer from this limitation.

The constitutive models developed in this chapter are formulated in terms of the nonlinear bond-strain measures introduced in [70] and described in Section 4.2:

$$\underline{\varepsilon}_{(m)}\langle\boldsymbol{\xi}\rangle := \frac{1}{2m}\left[\underline{c}\langle\boldsymbol{\xi}\rangle^{m} - 1\right],$$

where

$$\underline{c}\langle\boldsymbol{\xi}\rangle := \frac{\underline{\mathbf{Y}}\langle\boldsymbol{\xi}\rangle \cdot \underline{\mathbf{Y}}\langle\boldsymbol{\xi}\rangle}{\boldsymbol{\xi}\cdot\boldsymbol{\xi}}.$$

We propose nonlinear ordinary elastic solids with strain energy density:

$$\psi = \bar{\psi}\big(\underline{\varepsilon}_{(m)}\big) = \frac{\bar{\lambda}}{2}\theta_{(m)}^{2} + \bar{\mu}\,\mathrm{tr}_{\omega}\big(\underline{\varepsilon}_{(m)}^{2}\big), \tag{5.1}$$

where $\theta_{(m)} := \mathrm{tr}_{\omega}\big(\underline{\varepsilon}_{(m)}\big)$ is a nonlinear measure of the volumetric dilatation, $\bar{\lambda}$ and $\bar{\mu}$ are peridynamic Lamé constants, and we introduce the ω-trace operator $\mathrm{tr}_{\omega}(\cdot) : \mathcal{V}^{1} \to \mathbb{R}$, where the ω-trace of a scalar-state $\underline{a}$ is defined as

$$\mathrm{tr}_{\omega}(\underline{a}) := \int_{\mathcal{H}} \underline{\omega}\langle\boldsymbol{\xi}\rangle\,\underline{a}\langle\boldsymbol{\xi}\rangle\; d\boldsymbol{\xi}.$$

For consistency with the trace of the identity tensor in 3D, we constrain the influence function to satisfy $\mathrm{tr}_{\omega}(\underline{1}) = \int_{\mathcal{H}} \underline{\omega}\langle\boldsymbol{\xi}\rangle\; d\boldsymbol{\xi} = 3$, where we use the identity scalar-state: $\underline{1}\langle\boldsymbol{\xi}\rangle := 1$. The force vector-state for a nonlinear ordinary elastic solid follows from

work conjugacy as

$$\underline{\mathbf{T}}_{(m)}\langle\boldsymbol{\xi}\rangle = \bar{\psi}_{,\underline{\mathbf{Y}}}\langle\boldsymbol{\xi}\rangle\left(\underline{\varepsilon}_{(m)}\right) = \left(\bar{\lambda}\,\theta_{(m)} + 2\,\bar{\mu}\,\underline{\varepsilon}_{(m)}\langle\boldsymbol{\xi}\rangle\right)\underline{\omega}\langle\boldsymbol{\xi}\rangle\,\underline{c}\langle\boldsymbol{\xi}\rangle^{m-1}\,|\boldsymbol{\xi}|^{-2}\underline{\mathbf{Y}}\langle\boldsymbol{\xi}\rangle\,.$$

One could in principal apply a similar approach to even more general strain energy densities based on peridynamic analogs of deformation (strain) invariants [75, 37].

The elastic energy density can alternatively be written as the sum of a volumetric and a deviatoric term:

$$\tilde{\psi}\left(\underline{\varepsilon}_{(m)}\right) = \frac{\bar{\kappa}}{2}\,\theta_{(m)}^2 + \bar{\mu}\,\mathrm{tr}_\omega\left(\underline{\varepsilon}_{(m)}^{dev}\,\underline{\varepsilon}_{(m)}^{dev}\right), \tag{5.2}$$

where the ω-traceless deviatoric scalar-state $\underline{\varepsilon}_{(m)}^{dev}$ is defined as

$$\underline{\varepsilon}_{(m)}^{dev} := \underline{\varepsilon}_{(m)} - \mathrm{tr}_\omega\left(\underline{\varepsilon}_{(m)}\right)\underline{1}/3,$$

and $\bar{\kappa} = \bar{\lambda} + \frac{2}{3}\bar{\mu}$.[1]

It can be shown that the extension scalar-state (2.12) can be written in terms of the strain scalar-state with $m = 1/2$, as $\underline{e}\langle\boldsymbol{\xi}\rangle = \underline{\varepsilon}_{(1/2)}\langle\boldsymbol{\xi}\rangle \cdot |\boldsymbol{\xi}|$. Furthermore, it is easy to show from Equation (5.2) that nonlinear ordinary solids with $m = 1/2$ are equivalent to linear ordinary peridynamic solids with unnormalized influence function

[1]Note the analogy with classical hyperelastic isotropic materials with Lamé parameters μ and λ which can equivalently be written in terms of κ and μ, where $\kappa = \lambda + \frac{2}{3}\mu$.

$\underline{\tilde{\omega}}\langle\boldsymbol{\xi}\rangle = \frac{1}{3}\gamma\,\underline{\omega}\langle\boldsymbol{\xi}\rangle\,|\boldsymbol{\xi}|^{-2}$, bulk parameter $k = \bar{\kappa}$, and shear parameter $\alpha = 6\bar{\mu}/\gamma$:

$$\begin{aligned}
\tilde{\psi}\big(\underline{\varepsilon}_{(1/2)}\big) &= \frac{\bar{\kappa}}{2}\,\theta_{(1/2)}^2 + \bar{\mu}\,\mathrm{tr}_\omega\big(\underline{\varepsilon}_{(1/2)}^{dev}\,\underline{\varepsilon}_{(1/2)}^{dev}\big) \\
&= \frac{k}{2}\theta_{(1/2)}^2 + \gamma\frac{\alpha}{6}\int_{\mathcal{H}}\frac{3}{\gamma}\,\underline{\tilde{\omega}}\langle\boldsymbol{\xi}\rangle\,|\boldsymbol{\xi}|^2\left(\underline{\varepsilon}_{(1/2)}\langle\boldsymbol{\xi}\rangle - \frac{1}{3}\theta_{(1/2)}\right)^2 d\boldsymbol{\xi} \\
&= \frac{k}{2}\theta^2 + \frac{\alpha}{2}\int_{\mathcal{H}}\underline{\tilde{\omega}}\langle\boldsymbol{\xi}\rangle\left(\underline{e}\langle\boldsymbol{\xi}\rangle - \frac{1}{3}\theta|\boldsymbol{\xi}|\right)^2 d\boldsymbol{\xi} \\
&= \frac{k}{2}\theta^2 + \frac{\alpha}{2}\int_{\mathcal{H}}\underline{\tilde{\omega}}\langle\boldsymbol{\xi}\rangle\,\underline{e}^{dev}\langle\boldsymbol{\xi}\rangle\,\underline{e}^{dev}\langle\boldsymbol{\xi}\rangle\,d\boldsymbol{\xi},
\end{aligned}$$

which is identical to the energy for the linear peridynamic solids, as defined in Equation (2.13), and where we use the fact that

$$\theta_{(1/2)} = \int_{\mathcal{H}}\underline{\omega}\langle\boldsymbol{\xi}\rangle\,\underline{\varepsilon}_{(1/2)}\,d\boldsymbol{\xi} = \frac{3}{\gamma}\int_{\mathcal{H}}\underline{\tilde{\omega}}\langle\boldsymbol{\xi}\rangle\,\underline{e}\langle\boldsymbol{\xi}\rangle\,|\boldsymbol{\xi}|\,d\boldsymbol{\xi} = \theta.$$

In this sense, the proposed nonlinear theory is a direct generalization of the linear ordinary peridynamic solids model [98].

It follows that for $\bar{\kappa} = \kappa$ and $\bar{\mu} = \alpha\gamma/6 = \frac{5}{2}\,\mu$, the energy density of a nonlinear ordinary elastic peridynamic solid is identical to its corresponding classical isotropic elastic solid for uniform infinitesimal strain fields. In terms of the classical Lamé constants, the peridynamic Lamé constant $\bar{\lambda}$ follows as $\bar{\lambda} = \bar{\kappa} - \frac{2}{3}\bar{\mu} = \kappa - \frac{5}{3}\mu = \lambda - \mu$. The relationship between the peridynamic Lamé constants and their classical values are summarized as:

$$\begin{aligned}
\bar{\kappa} &= \kappa, \\
\bar{\mu} &= \frac{5}{2}\mu, \\
\bar{\lambda} &= \lambda - \mu, \\
\text{also } \bar{\kappa} &= \bar{\lambda} + \frac{2}{3}\bar{\mu}.
\end{aligned}$$

These results can also be derived directly by equating the expression for the strain

energy density, Equation (5.1), for uniform infinitesimal strains with the strain energy density of classical isotropic elastic materials (see also [98, 70]).

Another interesting feature of this formulation is that a material with $\bar{\lambda} = 0$ has elastic energy density

$$\bar{\psi}(\underline{\varepsilon}_{(m)}) = \bar{\mu} \int_{\mathcal{H}} \underline{\omega} \langle \boldsymbol{\xi} \rangle \, \underline{\varepsilon}^2_{(m)} \, d\boldsymbol{\xi}, \tag{5.3}$$

which directly satisfies the definition of a bond-based peridynamic material [100]. Consistent with this observation, one finds that $\bar{\lambda} = 0$ implies $\lambda = \mu$ and therefore $\nu = 1/4$, as expected for bond-based peridynamics.

We point out that these materials share features with the extended constitutive correspondence materials discussed in Sections 4.2-4.3, in that they are based on bond-level nonlinear strain measures and are both *ordinary*. However, these material models are distinctly different due to the fact that the isotropic materials described here explicitly include a *bond-based* term which is absent in the extended constitutive correspondence formulation.

5.2 Limitations and fixes for ordinary elastic solids

In this section, we seek to demonstrate how the generalized theory of ordinary peridynamic solids proposed above overcomes fundamental limitations of the original linear theory (alluded to in Section 2.2.2). Specifically, we provide concrete examples which expose these limitation in the linear ordinary elastic theory [98] and demonstrate the advantages of the proposed generalized nonlinear theory. The examples we use are the same as those in Section 4.2.

5.2.1 Unphysical behavior of the linear theory under degenerate deformations

1. **Sub-horizon material collapse**: We first consider the situation depicted in Figure 5-1 where a small volume of material $\mathcal{G} \subset \mathcal{B}_0$ collapses to a single point $\mathbf{z} \in \mathcal{B}_t$. The peridynamic deformation vector-state in this case is assumed to be $\underline{\mathbf{Y}}[\mathbf{x}]\langle\boldsymbol{\xi}\rangle = \mathbf{0}$ for $\mathbf{x} \in \mathcal{G}$, $\mathbf{x}+\boldsymbol{\xi} \in \mathcal{G}$ and $\underline{\mathbf{Y}}[\mathbf{x}]\langle\boldsymbol{\xi}\rangle = \boldsymbol{\xi}$ otherwise. This deformation is clearly unphysical as it violates the matter interpenetration constraint (2.3) and, in fact, does so over a finite region.

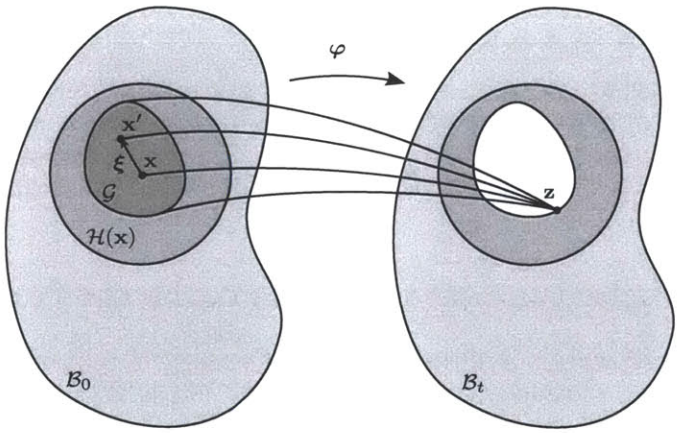

Figure 5-1: Schematic showing a region $\mathcal{G} \subset \mathcal{B}_0$ collapsing to a single point $\mathbf{z} \in \mathcal{B}_t$.

Computing the elastic energy density functional at $\mathbf{x}$, Equation (5.1), for this examples with $m = 1/2$ (which corresponds to the linear case), we find

$$\begin{aligned} |\theta| &= \left| \int_{\mathcal{H}(\mathbf{x})} \underline{\omega}\langle\boldsymbol{\xi}\rangle\, |\boldsymbol{\xi}|^{-1} \left(|\underline{\mathbf{Y}}\langle\boldsymbol{\xi}\rangle| - |\boldsymbol{\xi}| \right) d\boldsymbol{\xi} \right| \\ &= \left| \int_{\mathcal{G}(\mathbf{x})} -\underline{\omega}\langle\boldsymbol{\xi}\rangle\, d\boldsymbol{\xi} \right| < \infty, \end{aligned}$$

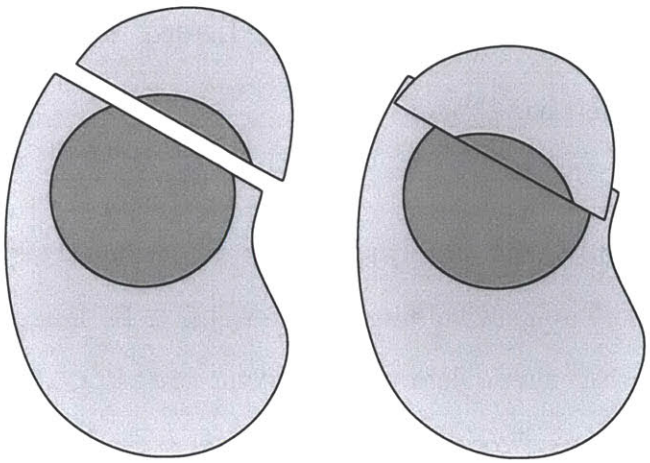

a) opening b) interpenetrating

Figure 5-2: Schematic of surface discontinuities, with both an opening deformation discontinuity (left) and an interpenetrating deformation discontinuity (right).

where $\mathcal{G}(\mathbf{x}) := \{\boldsymbol{\xi} \mid \mathbf{x} + \boldsymbol{\xi} \in \mathcal{G}\}$. We therefore find that the energy is bounded:

$$\begin{aligned}\psi(\underline{\mathbf{Y}}) &= \frac{k\theta^2}{2} + \frac{\alpha}{2}\int_{\mathcal{H}(\mathbf{x})} \underline{\omega}\,\langle\boldsymbol{\xi}\rangle\,|\boldsymbol{\xi}|^{-2}\left(\,|\underline{\mathbf{Y}}\,\langle\boldsymbol{\xi}\rangle| - |\boldsymbol{\xi}|\,\right)^2 d\boldsymbol{\xi} \\ &= \frac{k\theta^2}{2} + \frac{\alpha}{2}\int_{\mathcal{G}(\mathbf{x})} \underline{\omega}\,\langle\boldsymbol{\xi}\rangle\; d\boldsymbol{\xi} < \infty.\end{aligned}$$

This indicates that the linear ordinary theory fails to prevent local matter collapse. In other words, a finite amount of energy is required to force the body into an unphysical deformation mode. This is consistent with the observation in Section 2.2.2 that the bond-force remains finite in the presence of matter interpenetration.

2. **Interpenetrating jump discontinuities in 1D**: Another illustrative example consists of a displacement jump discontinuity in 1D with a displacement field of $y(x) = a + x$ for $x > 0$ and $y(x) = x$ for $x < 0$. A schematic showing the nature of this discontinuity is shown in Figure 5-2 for $a > 0$ on the left (which is physically acceptable), and $a < 0$ on the right (which is physically impossible).

We consider the strain energy density functional, Equation (5.1), and for simplicity restrict attention to the 1D and the bond-based case, $\bar{\lambda} = 0$, as in the limit of matter interpenetration, the bond-based term typically dominates the dilatation term for the cases considered here. Additionally, for $a < 0$ with $|a| < \delta$, we find at a point $x < 0$ with $|x| < |a|$ that

$$\begin{aligned}
\frac{1}{\bar{\mu}}\psi(x) &= \int_{x-\delta}^{x+\delta} \omega(|x'-x|)\, \underline{\varepsilon}^2_{(1/2)}\langle\xi\rangle\, dx' \\
&= \int_{0}^{x+\delta} \omega(|x'-x|)\, |x'-x|^{-2} \left(|x'+a-x| - |x'-x|\right)^2 dx' \\
&= \int_{0}^{x-a} \frac{\omega(|x'-x|)}{|x'-x|^2} \left(2x-2x'-a\right)^2 dx' + \int_{x-a}^{x+\delta} \frac{\omega(|x'-x|)}{|x'-x|^2} a^2\, dx' \\
&< \infty,
\end{aligned}$$

provided that

$$\int_{0}^{x+\delta} \omega(|x'-x|)|x'-x|^{-2}\, dx' < \infty. \tag{5.4}$$

This indicates that for sufficiently smooth influence functions, the energy required to create a surface of discontinuity involving matter interpenetration is finite.

We note that in principal it is possible to use influence functions which are sufficiently singular as $\xi \to 0$ to prevent matter interpenetration due to jump discontinuities. However, this has two unacceptable limitations: 1) uniform crushing, as in the first example, is still allowed, and 2) as will be shown below, singular influence function would also prevent opening (crack-like) jump discontinuities, whose existence is often regarded as a key advantage of the peridynamic theory over existing continuum models.

3. **Opening jump discontinuities in 1D:** We next consider the case $a > 0$,

corresponding to an opening displacement jump discontinuity (as would occur for fracture). The goal here is to confirm that the constitutive behavior is reasonable in the presence of physically allowable discontinuities, as the ability to handle such discontinuities is regarded as one of the key features of the peridynamic theory. At a point $x < 0$ with $|x| < \delta$, we find

$$\begin{aligned}\frac{1}{\bar{\mu}}\psi(x) &= \int_{x-\delta}^{x+\delta} \omega(|x'-x|)\, \underline{\varepsilon}^2_{(1/2)}\langle\xi\rangle\, dx' \\ &= \int_{0}^{x+\delta} \omega(|x'-x|)\, |x'-x|^{-2} \left(|x'+a-x| - |x'-x|\right)^2\, dx' \\ &= a^2 \int_{0}^{x+\delta} \omega(|x'-x|)\, |x'-x|^{-2}\, dx'.\end{aligned}$$

This shows that the elastic energy density is finite for sufficiently *smooth* influence functions, as desired. However, it is interesting to note that for *poorly* behaved influence functions with $\int_{-\delta}^{\delta} \omega(|\xi|)\, |\xi|^{-2}\, d\xi \to \infty$, the elastic energy density is undefined at the surface of discontinuity, $x = 0$. This indicates that the regularity of the influence function dictates the smoothness of the possible solutions to the peridynamic equations.[2] In particular, in order for physically realistic opening discontinuities (e.g., Figure 5-2, left) to be admissible, the influence function must be sufficiently smooth that Equation (5.4) is satisfied.

To summarize, when using the linear theory of ordinary peridynamic solids one is faced with two options regarding the choice of influence function. The first option is to allow for crack-like discontinuities (using sufficiently smooth influence functions), but this choice would also allow for matter interpenetration due to jump discontinuities. The other alternative is to choose influence functions which are sufficiently non-smooth to prevent matter interpenetration due to jump discontinuities. However, this would necessarily also prevent the

[2] A related observation that the smoothness of the influence function (in the form of the bond-based micro-modulus) impacts the smoothness of the solution has previously been made in [99].

possibility of opening crack-like discontinuities (which are highly desirable). It appears that the only other feasible option is to modify the strain measures so that matter interpenetration is strictly prohibited, while opening crack-like discontinuities are still allowed, as desired.

5.2.2 Behavior of the nonlinear theory under degenerate deformations

Here we now show how the generalized nonlinear ordinary elastic theory, as presented in Section 5.1, properly addresses the issues with the linear theory. In particular, the new formulation strictly precludes matter interpenetrating deformations, yet allows for physically admissible crack-like surfaces of discontinuity. We repeat the examples above to investigate the behavior of the nonlinear theory under unphysical deformations.

1. **Sub-horizon material collapse**: We again consider the unphysical situation in which $\underline{\mathbf{Y}}[\mathbf{x}]\langle\boldsymbol{\xi}\rangle = \mathbf{0}$ for $\mathbf{x} \in \mathcal{G}$, $\mathbf{x}+\boldsymbol{\xi} \in \mathcal{G}$. The nonlinear dilatation for this example is

$$\begin{aligned}\theta_{(m)} &= \int_{\mathcal{H}(\mathbf{x})} \underline{\omega}\langle\boldsymbol{\xi}\rangle \underline{\varepsilon}_{(m)}\, d\boldsymbol{\xi} \\ &= \frac{1}{2m}\int_{\mathcal{H}(\mathbf{x})} \underline{\omega}\langle\boldsymbol{\xi}\rangle |\boldsymbol{\xi}|^{-2m} |\underline{\mathbf{Y}}\langle\boldsymbol{\xi}\rangle|^{2m}\, d\boldsymbol{\xi} - \frac{3}{2m},\end{aligned}$$

It follow immediately that $\theta_{(m)} \to -\infty$ for $m < 0$. It is straightforward to show that this is also true for $m = 0$. In turn, this implies that for any $\mathbf{x} \in \mathcal{G}$, $\psi(\mathbf{x}) \to \infty$, provided that $\bar{\lambda} > 0$.

For completeness we also consider the case in which the constitutive model is that of a nonlinear bond-based material, $\bar{\lambda} = 0$, $\bar{\mu} > 0$. In this case, the elastic

energy density functional is

$$\psi_{(m)}(\underline{\mathbf{Y}}) = \frac{\bar{\mu}}{4m^2} \int_{\mathcal{H}(\mathbf{x})} \underline{\omega}\,\langle \boldsymbol{\xi} \rangle\, |\boldsymbol{\xi}|^{-4m} \left(|\underline{\mathbf{Y}}\,\langle \boldsymbol{\xi} \rangle|^{2m} - |\boldsymbol{\xi}|^{2m} \right)^2 d\boldsymbol{\xi}$$

and again we find that both for $m < 0$ and $m = 0$, an infinite amount of energy is required to fully collapse the material, i.e., $\psi_{(m)}(\mathbf{x}) \to \infty$ for $\mathbf{x} \in \mathcal{G}$.

2. **Interpenetrating jump discontinuities in 1D**: We return to the displacement jump discontinuity example which assumes an imposed deformation field of $y(x) = a + x$ for $x > 0$ and $y(x) = x$ for $x < 0$. A schematic showing the nature of this discontinuity is shown in Figure 5-2 for $a > 0$ on the left (which is physically acceptable), and $a < 0$ on the right (which is physically impossible).

   We consider the strain energy density functional, Equation (5.1), and for simplicity restrict attention to the bond-based limit, $\bar{\lambda} = 0$. First considering the matter interpenetrating case, $a < 0$, with $|a| < \delta$, we find at a point $x < 0$ with $|x| < |a|$ that

$$\begin{aligned}
\psi_{(m)}(x) &= \frac{\bar{\mu}}{4m^2} \int_0^{x+\delta} \frac{\omega(|x'-x|)}{|x'-x|^{4m}} \left(|x'+a-x|^{2m} - |x'-x|^{2m} \right)^2 dx' \\
&= \frac{\bar{\mu}}{4m^2} \int_0^{x-a} \frac{\omega(x'-x)}{(x'-x)^{4m}} \left((x-a-x')^{2m} - (x'-x)^{2m} \right)^2 dx' \\
&\quad + \frac{\bar{\mu}}{4m^2} \int_{x-a}^{x+\delta} \frac{\omega(x'-x)}{(x'-x)^{4m}} \left((x'+a-x)^{2m} - (x'-x)^{2m} \right)^2 dx',
\end{aligned}$$

   and $\psi_{(m)}(x) \to \infty$ for $4m < -1$. It follows from symmetry that $\psi(x) \to \infty$ for $a < x < -a$, $m < \frac{1}{4}$.[3]

3. **Opening jump discontinuities in 1D:** Lastly, we return to the case $a > 0$,

[3]This result is similar to that in Section 4.2.3, where is was shown that the nonlocal strain tensor becomes infinite near interpenetrating jump discontinuities for $m < 1/2$. The fact that the result here is slightly stronger results from the fact that isotropic ordinary materials contain a *bond-based* term which provides stricter enforcement of the kinematic constraint than an integral measure of strain (provided, of course, that a nonlinear bond-strain measure is used).

corresponding to an opening displacement jump discontinuity (as would occur during fracture). At a point $x < 0$ with $|x| < \delta$, we find

$$\psi(x) = \frac{\bar{\mu}}{4m^2} \int_0^{x+\delta} \frac{\omega(|x'-x|)}{|x'-x|^{4m}} \left(|x'+a-x|^{2m} - |x'-x|^{2m} \right)^2 dx',$$

and we find that $\psi(x) < \infty$, provided that $\int_{x-\delta}^{x+\delta} \omega(|x'-x|)\,|x'-x|^{-4m}\, d\xi < \infty$. This indicates that for a nonlinear ordinary elastic model (with $m < -1/4$ and a sufficiently smooth influence function) prevents matter interpenetrating surfaces of discontinuity (at least in 1D) and simultaneously allows for physically reasonably opening jump discontinuities. We speculate that the situation is similar for $m \in [-1/4, 0]$, and interpenetrating discontinuities require infinite work and are therefore inadmissible. In lieu of analytic results, in Section 5.3 we support this claim using numerical examples which compare the material behavior using a strain measure with $m = 0$ and the standard $m = 1/2$.

5.3 Numerical example: peridynamic Riemann problem

In order to further highlight the advantages of using nonlinear bond strain measures, we consider a peridynamic analog of the classical Riemann problem. For completeness, we note that an analytic solution to a version of the peridynamic Riemann problem has been solved in the context of linear bond-based peridynamics [23]; however, the issue of matter interpenetration was not considered, as it was not a focus of the paper. We note that because the problem was linear in the displacements, matter interpenetration was indeed allowed as a possible solution.

Here, we conduct simulations of a 2D peridynamic bar of length $l = 2\,\mathrm{m}$ and height $h = 1\,\mathrm{m}$. The numerical method we use is based on the particle discretization

approach reviewed in Chapter 3. The initial conditions for this problem are

$$v_1(\mathbf{x}, t=0) = \begin{cases} -1200 \text{ m/s} & \text{for } x_1 > 0 \\ 1200 \text{ m/s} & \text{for } x_1 < 0, \end{cases}$$

$$v_2(\mathbf{x}, t=0) = 0,$$

$$\mathbf{y}(\mathbf{x}, t=0) = \mathbf{x}.$$

This example provides a strenuous test of peridynamic constitutive theories when subjected to compressive loadings, as might occur during ballistic impact events. It was demonstrated in Section 5.2.2, that nonlinear ordinary elastic theories of peridynamics with strain measure parameters $m \leq 0$ have the appropriate limiting behavior to prevent localized volumetric material collapse. Furthermore, for $m < -1/4$ it was shown that matter interpenetrating surfaces of discontinuities are also disallowed (at least in 1D). It is possible that this last property also holds more generally, for $m \leq 0$, but we have yet to demonstrate this analytically. Instead, here we conduct numerical examples using $m = 0$ and $m = 1/2$, respectively, in order to demonstrate the advantage of using a logarithmic bond-strain measure in computations.

For the simulations in this section, the material properties are taken to be $\bar{\lambda} =$ 10 GPa, $\bar{\mu} =$ 10 GPa, $\rho =$ 1180 kg/m^3, and $\delta =$ 0.05 m. Also, the 2D influence function we use is given by Equation (6.6). Using the standard peridynamic particle discretization (Sections 3.1), we first consider the peridynamic Riemann problem for a relatively coarse mesh of 20,000 particles and 80 neighbors within the horizon of each (interior) particles. The results using a strain measure with $m = 1/2$ at several different times are shown in Figure 5-3, where the half of the specimen initially on the left with velocity $v_1(t = 0) =$ 1200 m/s is colored red and the right half with $v_1(t = 0) = -1200$ m/s is colored blue. The surface between the two halves is modeled to be pre-fractured so that it cannot support tensile loadings, but particle

interactions are maintained in compression. This is done in order to simulate contact in a more natural way, but the conclusions of this section are insensitive to this particular modeling assumption. The corresponding results for $m = 0$ are shown in Figure 5-4.

These results indicate that in certain situations (e.g., sufficiently high impact velocities), the traditional linear peridynamic solids, $m = 1/2$, are unable to prevent matter interpenetration in simulations. On the other hand, for the case using a log-strain measure, $m = 0$, no appreciable matter interpenetration is observed for the same initial conditions (Figure 5-4). This is a direct result of the fact that as neighboring particles approach each other, the repulsive force between them increases arbitrarily in the limit of complete contact. We note that for sufficiently low velocities (not shown in this thesis as it is a more standard peridynamic result), the simulation results remain physical using either of the two strain measures.[4]

While the use of nonlinear strain measures appears to be critical for preventing matter interpenetration during impact events, we point out that there are some potential drawbacks to the approach. The first drawback is that computing nonlinear strain measures is more computationally expensive than the constitutive evaluations in the linear version of the theory. A second limitation is that for even higher initial impact velocities, discretization errors can still lead to matter interpenetration in simulations. However, in practice this limitation can be overcome by further refining the discretization and having more neighboring particle in the horizon, but this may become computationally prohibitive. The final and most significant drawback is that as particles approach each other, the nonlinear behavior is such that the elastic "bond-stiffness" increases, meaning that the simulation stable time-step often has to decrease substantially under compressive loadings. This is in contrast to

[4]Our observation has been that for fixed elastic constants and horizon size there is a critical energy barrier (impact velocity) which must be overcome in order for matter interpenetration (as shown in Figure 5-3) to occur in linear peridynamic solids.

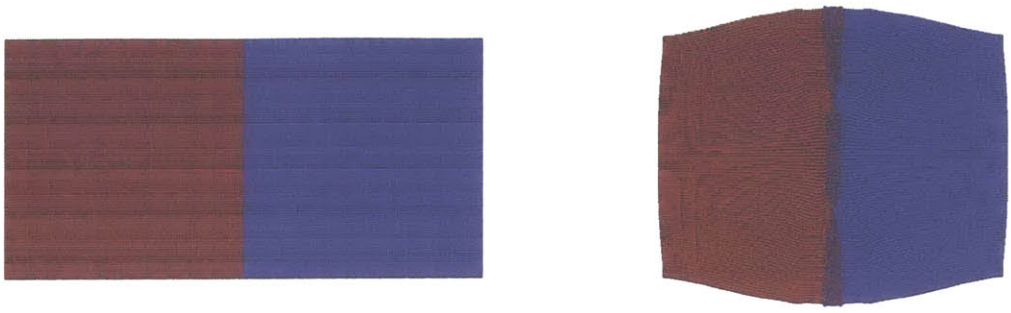

(a) $t = 0\ \mu s$

(b) $t = 50\ \mu s$

(c) $t = 100\ \mu s$

(d) $t = 150\ \mu s$

Figure 5-3: Self impact for 20,000 particle mesh with $|\mathbf{v}_0| = 1200$ and $m = 1/2$.

the case $m = 1/2$, where the stable time-step does not appear to change appreciably throughout the course of the simulation.

To show that these conclusions are insensitive to the discretization size, we provide additional results using a slightly finer mesh of 34,000 particles and 120 neighbors for each (interior) material point. The results for $m = 1/2$ are shown in Figure 5-5, and those using $m = 0$ are shown in Figure 5-6. Once again, we conclude that using a nonlinear strain measure ($m \leq 0$) is critical for preventing matter interpenetration in simulation. In fact, our experience suggests that as the discretization is further refined, matter interpenetration issues become more pervasive for $m = 1/2$, while with $m = 0$, finer meshes are better able to prevent matter interpenetration for fixed initial velocity, horizon and elastic constants. This is likely due to the fact that we are better resolving the highly localized nonlinear response. Additionally, we point out that the

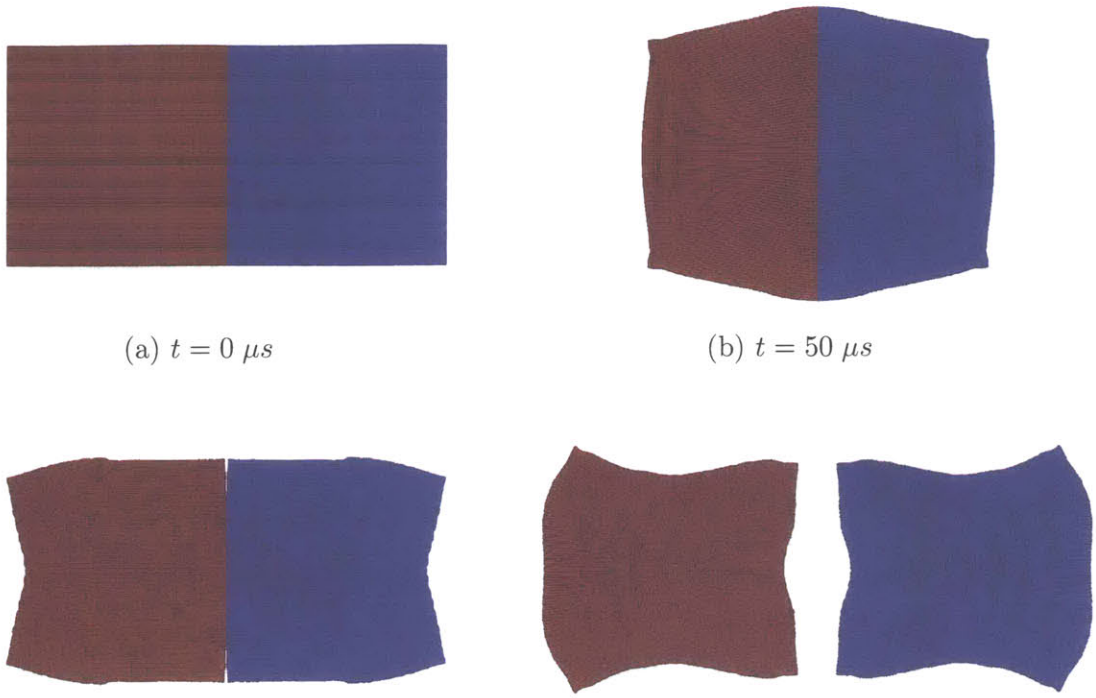

(a) $t = 0\ \mu s$ (b) $t = 50\ \mu s$

(c) $t = 100\ \mu s$ (d) $t = 150\ \mu s$

Figure 5-4: Self impact for 20,000 particle mesh with $|\mathbf{v}_0| = 1200$ and $m = 0$.

results in Figures 5-4 and 5-6 show solutions which are relatively insensitive to the mesh size, an indication of convergence.

5.4 Chapter summary

A nonlinear extension to the existing linear elastic theory of ordinary peridynamics (linear peridynamic solids) was proposed. Although the ability to naturally handle field discontinuities has been suggested as an important advantage of the peridynamic theory over classical continuum theories, [98, 97], in some situations this flexibility may go to far and result in peridynamic formulations in which highly unphysical deformation modes (i.e. matter interpenetration) are allowed. The proposed nonlinear generalization is shown to overcome limitations in existing peridynamic theories in the limit of matter interpenetration. The is accomplished by formulating the ordinary

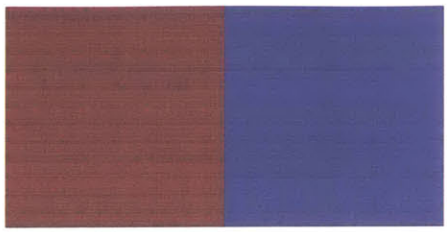

(a) $t = 0\ \mu s$

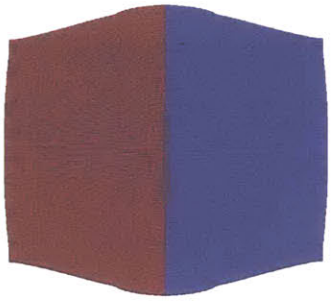

(b) $t = 50\ \mu s$

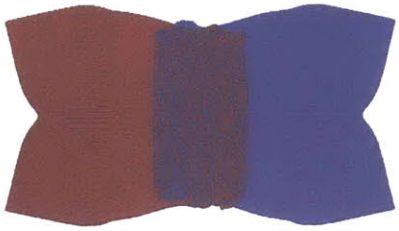

(c) $t = 100\ \mu s$

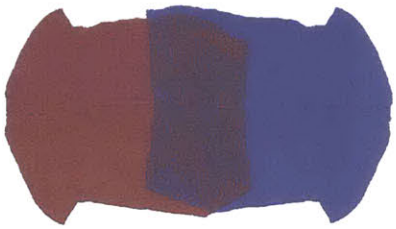

(d) $t = 150\ \mu s$

Figure 5-5: Self impact for 35,912 particle mesh with $|\mathbf{v}_0| = 1200$ and $m = 1/2$.

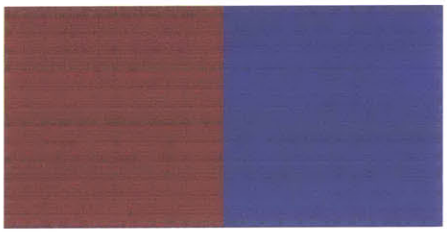

(a) $t = 0\ \mu s$

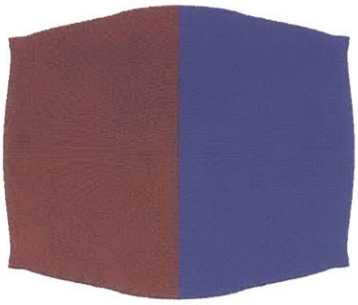

(b) $t = 50\ \mu s$

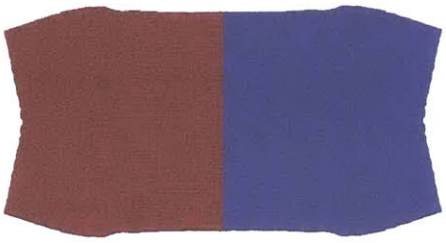

(c) $t = 100\ \mu s$

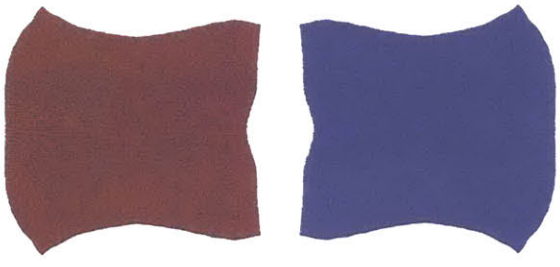

(d) $t = 150\ \mu s$

Figure 5-6: Self impact for 35,912 particle mesh with $|\mathbf{v}_0| = 1200$ and $m = 0$.

constitutive theory directly in terms of nonlinear bond-strain measures which are capable of enforcing the matter interpenetration constraint of peridynamics (2.3) on a bond-by-bond basis. Several analytical examples are provided which demonstrate how unphysical behavior is prevented by this nonlinear generalization. Numerical examples based on a peridynamic analog of the Riemann problem were used to further highlight the advantages of the proposed nonlinear theory. In particular, it was demonstrated that the linear version of the theory exhibits matter interpenetration for sufficiently high initial impact velocities, and that this issue is alleviated by using a logarithmic bond-strain measure.

Chapter 6

Brittle damage modeling in state-based peridynamics

In this chapter, a generalized bond-failure criterion for brittle state-based peridynamic materials is proposed. This approach extends several previous approaches to peridynamic damage modeling in which bonds are severed based on either a maximum bond-stretch criterion [94] or a critical bond-energy criterion [39] to more general cases in which the critical bond-energy at failure is allowed to vary with bond length. As with previous approaches, the proposed damage model is constructed such that the classical linear elastic fracture energy, G_c, is dissipated when all of the bonds are broken across an interior fracture surface of unit area.

The damage formulation is derived using a bond-energy type of criterion, similar to that in [39]. However, it will be shown that the concept of *bond-energy* is ambiguous due to the fact that the energy dissipated by severing a single bond depends on the order in which neighboring bonds are severed. To circumvent this difficulty, we introduce the *instantaneous bond-energy*, an unambiguous quantity which corresponds to the energy dissipated per unit volume-squared when a single bond is cut instantaneously (i.e. all other bonds remain unchanged during the bond-severing

process). The bond-failure criterion which we propose here is formulated in terms of this instantaneous bond-energy. In order to validate this bond-failure criterion, we conduct numerical simulations of brittle elastic peridynamic materials, where the elastic part of the constitutive response is based on the nonlinear generalization of ordinary elastic solids proposed in Chapter 5.

In Section 6.1, we derive the proposed bond-failure criterion for general state-based peridynamic materials. We specialize the failure criterion for a specific peridynamic influence functions and demonstrate that the resulting constitutive model satisfies the laws of thermodynamics in Section 6.1.3. In Sections 6.2.1 and 6.2.2, we investigate the ability of the nonlinear ordinary elastic solids based approach to capture experimentally observed fracture patterns in brittle materials subjected to projectile impact loadings. In addition, we demonstrate the scalability of the C++/MPI implementation in Section 6.2.3, which is important for resolving small-scale features of fracture.

6.1 Bond failure criteria for brittle peridynamic materials

Existing approaches to damage modeling in peridynamic are typically based on severing bonds instantaneously when a bond-level criterion is satisfied [94, 121]. For the most part, these criteria have been restricted to the bond-based version of the theory; however, recent developments have begun to extend these strategies to the state-based theory of peridynamics [39].

These approaches are made to be consistent with linear elastic fracture mechanics (LEFM) and the classical Griffith criterion [34] in the appropriate limit. This is accomplished by calibrating the bond-severing criterion such that cutting all of the bonds which cross an interior "crack" surface results in a dissipated energy per area

of G_c, where G_c is the classic fracture energy (fracture energy release rate) of the bulk elastic material. The original demonstration of this correspondence between a bond-severing criterion and the classical fracture energy was presented in [94]. In the following, we use this idea and generalize to the case where the critical bond-energy is a generic function of initial bond-length.

6.1.1 Relationship between the dissipated bond energy and the fracture energy

Starting with the 3D case, suppose we have a fracture energy of G_c, with units of energy per unit area. We require the fracture energy to be identical to the energy dissipated by severing bonds across an interior surface of unit area. Furthermore, suppose that the energy dissipated per bond is in general a function of the initial bond length, $s_c(\xi)$ (which has units of energy per unit volume-squared), where $\xi := |\boldsymbol{\xi}|$. The total elastic energy per unit area dissipated on one side of the newly formed surface is (see also [94],[39]):

$$\int_0^{\delta}\int_0^{2\pi}\int_z^{\delta}\int_0^{\cos^{-1}(z/\xi)} s_c(\xi)\,\xi^2\sin(\phi)\,d\phi\,d\xi\,d\theta\,dz = \frac{1}{2}G_c, \tag{6.1}$$

where we use spherical coordinates. The intuition behind the form of this integral is depicted schematically in Figure 6-1. The factor of a half in front of G_c is due to the fact that we are only considering the energy dissipated in the lower half of the fractured body ($z > 0$).

Similarly in 2D:

$$\int_0^{\delta}\int_z^{\delta}\int_{-\cos^{-1}(z/\xi)}^{\cos^{-1}(z/\xi)} s_c(\xi)\,\xi\,d\theta\,d\xi\,dz = \frac{1}{2}G_c, \tag{6.2}$$

where G_c now has units of energy per unit length, $s_c(\xi)$ now has units of energy per

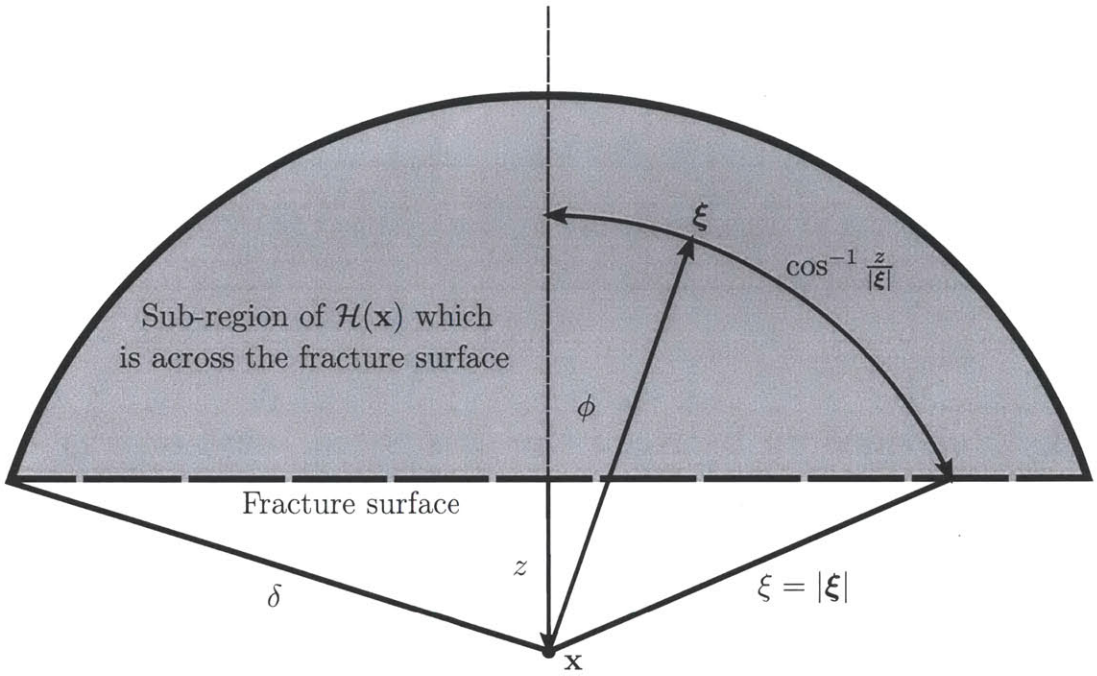

Figure 6-1: Schematic showing the region within the horizon $\mathcal{H}(\mathbf{x})$ and across the fracture surface from point $\mathbf{x}$. This figure (modified from [94]) depicts the domain of integration in Equations (6.2) and (6.1).

unit area-squared, and the integral is in polar coordinates.

The functional form of $s_c(\xi)$ is a constitutive choice which we call the bond-failure-energy function. The bond-failure-energy function weighs the relative failure strength of bonds depending on their initial lengths. For example, a reasonable first assumption might be that bonds corresponding to material points which are initially relatively far away from each other fail at lower bond-energies than material points which are initially closer to each other. This is in contrast to most existing approaches in which bonds are severed at the same energy independently of the distance between the material points [94, 121, 39].

For concreteness, in the remainder we consider a particular functional form for the bond failure-energy function:

$$s_c(|\boldsymbol{\xi}|) = \beta\, \underline{\omega}\langle\boldsymbol{\xi}\rangle\, |\boldsymbol{\xi}|^{-2}, \tag{6.3}$$

where $\underline{\omega}\langle\boldsymbol{\xi}\rangle$ is the normalized spherical influence function used for the nonlinear ordinary elastic material models in this thesis,[1] and β is a constitutive parameter which can be related to the fracture energy, G_c. This approach differs from existing approaches which are typically based on a maximum relative stretch (or strain) [94, 121] or a maximum bond-energy which is constant for all bonds in the family [39]. It will be shown in the applications later in this chapter that such an approach provides a feasible alternative to existing approaches and is capable of capturing physically realistic fracture patterns.

For the special case in which the material is bond-based with strain measure parameter $m = 1/2$, the bond-failure-energy function, Equation (6.3), is equivalent to a maximum relative bond-displacement criterion.[2] To demonstrate this, we consider a maximum bond displacement criterion: bonds are severed when $u(\boldsymbol{\xi}) \geq u_c$, where $u(\boldsymbol{\xi}) := |\underline{\mathbf{Y}}|\langle\boldsymbol{\xi}\rangle - |\boldsymbol{\xi}|$. This failure criterion can be rewritten in terms of bond strains as:

$$\underline{\varepsilon}_{(1/2)}\langle\boldsymbol{\xi}\rangle \geq \frac{u_c}{|\boldsymbol{\xi}|},$$

or alternatively

$$\bar{\mu}\,\underline{\omega}\langle\boldsymbol{\xi}\rangle\,\frac{u_c^2}{|\boldsymbol{\xi}|^2} < \bar{\mu}\,\underline{\omega}\langle\boldsymbol{\xi}\rangle\,\underline{\varepsilon}_{(1/2)}\langle\boldsymbol{\xi}\rangle\,\underline{\varepsilon}_{(1/2)}\langle\boldsymbol{\xi}\rangle = \underline{s}\langle\boldsymbol{\xi}\rangle\,,$$

where $\underline{s}\langle\boldsymbol{\xi}\rangle$ is the bond-energy in this case, as for bond-based materials

$$\int_{\mathcal{H}} \underline{s}\langle\boldsymbol{\xi}\rangle\; d\boldsymbol{\xi} = \psi,$$

where ψ is the elastic energy given by Equation (5.3) for $m = 1/2$. Taking $\beta = \bar{\mu}\,u_c^2$,

[1] In applications we used the influence functions in Equation (6.6) for 2D and Equation (6.7) for 3D.

[2] The use of a maximum relative bond displacement criterion is motivated by cohesive models of fracture [104] which typically have an analogous critical opening displacement.

this bond displacement criterion can be equivalently expressed as: bonds are severed when $\underline{s}\langle\boldsymbol{\xi}\rangle \geq s_c(|\boldsymbol{\xi}|)$, with $s_c(\xi)$ given by Equation (6.3).

6.1.2 Interpretation of the bond energy

In order to model brittle fracture problems in peridynamics, it is important to be able to calculate the elastic energy which is dissipated when breaking a single bond. For the case when the material is bond-based (as discussed above), the bond-energy is well defined, as the elastic energy is a direct integral of bond-energy, Equation (5.3). For more general elastic state-based materials, the energy per bond is not well defined. One proposal is to define a bond-energy by the integral of the work done on the bond [39]:

$$\underline{s}\langle\boldsymbol{\xi}\rangle(t) = \int_0^t \underline{\mathbf{T}}\langle\boldsymbol{\xi}\rangle \cdot \underline{\dot{\mathbf{Y}}}\langle\boldsymbol{\xi}\rangle \, dt.$$

However, this definition of bond-energy is not, in general, equal to the energy dissipated by severing the bond, as the dissipated energy for a particular bond depends on whether other bonds are severed simultaneously. To show this, we consider the case where the material is nonlinear ordinary elastic, Equation (5.2), modified appropriately to allow for severing bonds. The modified elastic energy is of the form:

$$\psi(\mathbf{x}) = \frac{1}{2}\bar{\lambda}\left(\int_{\mathcal{H}(\mathbf{x})} \underline{\phi}\langle\boldsymbol{\xi}\rangle \, \underline{\omega}\langle\boldsymbol{\xi}\rangle \, \underline{\varepsilon}\langle\boldsymbol{\xi}\rangle \, d\boldsymbol{\xi}\right)^2 + \bar{\mu}\int_{\mathcal{H}(\mathbf{x})} \underline{\phi}\langle\boldsymbol{\xi}\rangle \, \underline{\omega}\langle\boldsymbol{\xi}\rangle \, \underline{\varepsilon}\langle\boldsymbol{\xi}\rangle \, \underline{\varepsilon}\langle\boldsymbol{\xi}\rangle \, d\boldsymbol{\xi}, \tag{6.4}$$

where

$$\underline{\phi}\langle\boldsymbol{\xi}\rangle = \begin{cases} 1 & \text{for intact bonds,} \\ 0 & \text{for severed bonds,} \end{cases}$$

and $\underline{\varepsilon}\langle\boldsymbol{\xi}\rangle$ is the preferred bond-strain measure, Equation (4.2).

We first consider the case where all the bonds in the region $\mathcal{H}^\dagger \subset \mathcal{H}$ are broken simultaneously. The energy dissipated in this process is

$$\begin{aligned}
\Delta\psi^\dagger &= \frac{1}{2}\bar{\lambda}\left(\int_{\mathcal{H}} \underline{\omega}\langle\boldsymbol{\xi}\rangle\,\underline{\varepsilon}\langle\boldsymbol{\xi}\rangle\; d\boldsymbol{\xi}\right)^2 - \frac{1}{2}\bar{\lambda}\left(\int_{\mathcal{H}} \underline{\omega}\langle\boldsymbol{\xi}\rangle\,\underline{\varepsilon}\langle\boldsymbol{\xi}\rangle\; d\boldsymbol{\xi} - \int_{\mathcal{H}^\dagger} \underline{\omega}\langle\boldsymbol{\xi}\rangle\,\underline{\varepsilon}\langle\boldsymbol{\xi}\rangle\; d\boldsymbol{\xi}\right)^2 \\
&\quad + \bar{\mu}\int_{\mathcal{H}} \underline{\omega}\langle\boldsymbol{\xi}\rangle\,\underline{\varepsilon}\langle\boldsymbol{\xi}\rangle\,\underline{\varepsilon}\langle\boldsymbol{\xi}\rangle\; d\boldsymbol{\xi} - \bar{\mu}\left(\int_{\mathcal{H}} \underline{\omega}\langle\boldsymbol{\xi}\rangle\,\underline{\varepsilon}\langle\boldsymbol{\xi}\rangle\,\underline{\varepsilon}\langle\boldsymbol{\xi}\rangle\; d\boldsymbol{\xi} - \int_{\mathcal{H}^\dagger} \underline{\omega}\langle\boldsymbol{\xi}\rangle\,\underline{\varepsilon}\langle\boldsymbol{\xi}\rangle\,\underline{\varepsilon}\langle\boldsymbol{\xi}\rangle\; d\boldsymbol{\xi}\right) \\
&= \bar{\lambda}\left(\int_{\mathcal{H}} \underline{\omega}\langle\boldsymbol{\xi}\rangle\,\underline{\varepsilon}\langle\boldsymbol{\xi}\rangle\; d\boldsymbol{\xi}\right)\left(\int_{\mathcal{H}^\dagger} \underline{\omega}\langle\boldsymbol{\xi}\rangle\,\underline{\varepsilon}\langle\boldsymbol{\xi}\rangle\; d\boldsymbol{\xi}\right) - \frac{1}{2}\bar{\lambda}\left(\int_{\mathcal{H}^\dagger} \underline{\omega}\langle\boldsymbol{\xi}\rangle\,\underline{\varepsilon}\langle\boldsymbol{\xi}\rangle\; d\boldsymbol{\xi}\right)^2 \\
&\quad + \bar{\mu}\int_{\mathcal{H}^\dagger} \underline{\omega}\langle\boldsymbol{\xi}\rangle\,\underline{\varepsilon}\langle\boldsymbol{\xi}\rangle\,\underline{\varepsilon}\langle\boldsymbol{\xi}\rangle\; d\boldsymbol{\xi}.
\end{aligned}$$

We next consider the energy dissipated by cutting the bonds in some region $\mathcal{H}_a^\dagger$ and, in an independent experiment, the energy dissipated by cutting the bonds in $\mathcal{H}_b^\dagger$, with $\mathcal{H}_a^\dagger \cup \mathcal{H}_b^\dagger = \mathcal{H}^\dagger$, $\mathcal{H}_a^\dagger \cap \mathcal{H}_b^\dagger = \varnothing$. This results in

$$\begin{aligned}
\Delta\psi_a^\dagger + \Delta\psi_b^\dagger = \;& \bar{\mu}\int_{\mathcal{H}_a^\dagger} \underline{\omega}\langle\boldsymbol{\xi}\rangle\,\underline{\varepsilon}\langle\boldsymbol{\xi}\rangle\,\underline{\varepsilon}\langle\boldsymbol{\xi}\rangle\; d\boldsymbol{\xi} + \bar{\mu}\int_{\mathcal{H}_b^\dagger} \underline{\omega}\langle\boldsymbol{\xi}\rangle\,\underline{\varepsilon}\langle\boldsymbol{\xi}\rangle\,\underline{\varepsilon}\langle\boldsymbol{\xi}\rangle\; d\boldsymbol{\xi} \\
&+ \bar{\lambda}\left(\int_{\mathcal{H}} \underline{\omega}\langle\boldsymbol{\xi}\rangle\,\underline{\varepsilon}\langle\boldsymbol{\xi}\rangle\; d\boldsymbol{\xi}\right)\left(\int_{\mathcal{H}_a^\dagger} \underline{\omega}\langle\boldsymbol{\xi}\rangle\,\underline{\varepsilon}\langle\boldsymbol{\xi}\rangle\; d\boldsymbol{\xi}\right) - \frac{1}{2}\bar{\lambda}\left(\int_{\mathcal{H}_a^\dagger} \underline{\omega}\langle\boldsymbol{\xi}\rangle\,\underline{\varepsilon}\langle\boldsymbol{\xi}\rangle\; d\boldsymbol{\xi}\right)^2 \\
&+ \bar{\lambda}\left(\int_{\mathcal{H}} \underline{\omega}\langle\boldsymbol{\xi}\rangle\,\underline{\varepsilon}\langle\boldsymbol{\xi}\rangle\; d\boldsymbol{\xi}\right)\left(\int_{\mathcal{H}_b^\dagger} \underline{\omega}\langle\boldsymbol{\xi}\rangle\,\underline{\varepsilon}\langle\boldsymbol{\xi}\rangle\; d\boldsymbol{\xi}\right) - \frac{1}{2}\bar{\lambda}\left(\int_{\mathcal{H}_b^\dagger} \underline{\omega}\langle\boldsymbol{\xi}\rangle\,\underline{\varepsilon}\langle\boldsymbol{\xi}\rangle\; d\boldsymbol{\xi}\right)^2 \\
=\;& \Delta\psi^\dagger + \frac{1}{2}\bar{\lambda}\left(\int_{\mathcal{H}^\dagger} \underline{\omega}\langle\boldsymbol{\xi}\rangle\,\underline{\varepsilon}\langle\boldsymbol{\xi}\rangle\; d\boldsymbol{\xi}\right)^2 \\
&- \frac{1}{2}\bar{\lambda}\left(\int_{\mathcal{H}_a^\dagger} \underline{\omega}\langle\boldsymbol{\xi}\rangle\,\underline{\varepsilon}\langle\boldsymbol{\xi}\rangle\; d\boldsymbol{\xi}\right)^2 - \frac{1}{2}\bar{\lambda}\left(\int_{\mathcal{H}_b^\dagger} \underline{\omega}\langle\boldsymbol{\xi}\rangle\,\underline{\varepsilon}\langle\boldsymbol{\xi}\rangle\; d\boldsymbol{\xi}\right)^2 \\
=\;& \Delta\psi^\dagger + \bar{\lambda}\left(\int_{\mathcal{H}_a^\dagger} \underline{\omega}\langle\boldsymbol{\xi}\rangle\,\underline{\varepsilon}\langle\boldsymbol{\xi}\rangle\; d\boldsymbol{\xi}\right)\left(\int_{\mathcal{H}_b^\dagger} \underline{\omega}\langle\boldsymbol{\xi}\rangle\,\underline{\varepsilon}\langle\boldsymbol{\xi}\rangle\; d\boldsymbol{\xi}\right),
\end{aligned}$$

and for $\bar{\lambda} \neq 0$, $\Delta\psi^\dagger \neq \Delta\psi_a^\dagger + \Delta\psi_b^\dagger$.

This result shows that, in general, the dissipated bond-energy is not uniquely determined by the deformation state, as the elastic energy which is dissipated by breaking a particular bond depends on whether other neighboring bonds are cut

simultaneously (as well as which other bonds are being severed). This can be demonstrated in an even simpler manner by considering the two extreme limiting cases: 1) all bonds in the horizon are cut simultaneously, and 2) only a single bond is cut while all other bonds remain unchanged. In the first case, we have $\mathcal{H}_1^\dagger = \mathcal{H}(\mathbf{x})$, and the total energy dissipated is

$$\Delta\psi_1 = \frac{1}{2}\bar{\lambda}\left(\int_{\mathcal{H}} \underline{\omega}\langle\boldsymbol{\xi}\rangle\,\underline{\varepsilon}\langle\boldsymbol{\xi}\rangle\; d\boldsymbol{\xi}\right)\left(\int_{\mathcal{H}} \underline{\omega}\langle\boldsymbol{\xi}\rangle\,\underline{\varepsilon}\langle\boldsymbol{\xi}\rangle\; d\boldsymbol{\xi}\right) + \bar{\mu}\int_{\mathcal{H}} \underline{\omega}\langle\boldsymbol{\xi}\rangle\,\underline{\varepsilon}\langle\boldsymbol{\xi}\rangle\,\underline{\varepsilon}\langle\boldsymbol{\xi}\rangle\; d\boldsymbol{\xi},$$

and the dissipated energy associated with a particular bond $\boldsymbol{\xi}$ is

$$\underline{s}_1\langle\boldsymbol{\xi}\rangle = \frac{1}{2}\bar{\lambda}\,\underline{\omega}\langle\boldsymbol{\xi}\rangle\,\underline{\varepsilon}\langle\boldsymbol{\xi}\rangle\left(\int_{\mathcal{H}} \underline{\omega}\langle\boldsymbol{\xi}\rangle\,\underline{\varepsilon}\langle\boldsymbol{\xi}\rangle\; d\boldsymbol{\xi}\right) + \bar{\mu}\,\underline{\omega}\langle\boldsymbol{\xi}\rangle\,\underline{\varepsilon}\langle\boldsymbol{\xi}\rangle\,\underline{\varepsilon}\langle\boldsymbol{\xi}\rangle\,,$$

$$\text{. as } \int_{\mathcal{H}} \underline{s}_1\langle\boldsymbol{\xi}\rangle\; d\boldsymbol{\xi} = \Delta\psi_1.$$

In the second case, we have $\mathcal{H}^\dagger \to \{\boldsymbol{\xi}\}$ (which has zero-measure) and the energy dissipated due to cutting the bond $\boldsymbol{\xi}$ in isolation (i.e., with all other bonds unchanged) is

$$\underline{s}_2\langle\boldsymbol{\xi}\rangle = \bar{\lambda}\,\underline{\omega}\langle\boldsymbol{\xi}\rangle\,\underline{\varepsilon}\langle\boldsymbol{\xi}\rangle\left(\int_{\mathcal{H}} \underline{\omega}\langle\boldsymbol{\xi}\rangle\,\underline{\varepsilon}\langle\boldsymbol{\xi}\rangle\; d\boldsymbol{\xi}\right) + \bar{\mu}\,\underline{\omega}\langle\boldsymbol{\xi}\rangle\,\underline{\varepsilon}\langle\boldsymbol{\xi}\rangle\,\underline{\varepsilon}\langle\boldsymbol{\xi}\rangle\,.$$

Evidently, the energy dissipated per bond when cutting all bonds simultaneously, $\underline{s}_1\langle\boldsymbol{\xi}\rangle$, is not equal to the energy dissipated by cutting a single bond in isolation, $\underline{s}_2\langle\boldsymbol{\xi}\rangle$: $\underline{s}_1\langle\boldsymbol{\xi}\rangle \neq \underline{s}_2\langle\boldsymbol{\xi}\rangle$. In the numerical simulations conducted later in this chapter, we have found that it is typical for bonds to be severed in isolation (i.e., at different time-steps), so a reasonable approximation to the energy dissipated per bond is given by $\underline{s}_2\langle\boldsymbol{\xi}\rangle$ above. We call this particular bond energy the instantaneous bond-energy,

which in general is defined by the Fréchet derivative:

$$\underline{s}_{inst}\langle\boldsymbol{\xi}\rangle := \psi_{,\underline{\phi}}\langle\boldsymbol{\xi}\rangle, \tag{6.5}$$

where ψ is given by Equation (6.4).

6.1.3 Brittle peridynamic material model

The constitutive response for the brittle peridynamic materials simulated in this chapter are assumed to have strain energy density as given in Equation (6.4). For the 2D simulations in the chapter, we use a spherical peridynamic influence function, Equation (2.7), of

$$\omega_{2D}(|\boldsymbol{\xi}|) = \frac{10}{\pi}\delta^{-6}(3|\boldsymbol{\xi}| + \delta)(\delta - |\boldsymbol{\xi}|)^3, \tag{6.6}$$

which satisfies the conditions $\mathrm{tr}_\omega(\underline{1}) = \int_{\mathcal{H}_{2D}} \underline{\omega}_{2D}\langle\boldsymbol{\xi}\rangle\, d\boldsymbol{\xi} = 2$ (at least for material points which are far from the boundary), and $\omega > 0$ for $|\boldsymbol{\xi}| \in (0, \delta)$. Similarly, for 3D simulations we use the influence function:

$$\omega_{3D}(|\boldsymbol{\xi}|) = \frac{315}{16\pi}\delta^{-7}(3|\boldsymbol{\xi}| + \delta)(\delta - |\boldsymbol{\xi}|)^3, \tag{6.7}$$

which satisfies $\mathrm{tr}_\omega(\underline{1}) = \int_{\mathcal{H}_{3D}} \underline{\omega}_{3D}\langle\boldsymbol{\xi}\rangle\, d\boldsymbol{\xi} = 3$ at points far from the boundary of the body. We use the notation $\mathcal{H}_{2D}$ and $\mathcal{H}_{3D}$ to distinguish the dimension of the peridynamic horizon, when necessary.

We choose to use these (normalized) influence functions everywhere in the domain, even near boundaries of the body. A consequence of this decision is that near boundaries we have $\mathrm{tr}_\omega(\underline{1}) \neq 3$ in 3D and $\mathrm{tr}_\omega(\underline{1}) \neq 2$ in 2D, which in turn implies that the nonlocal dilatation near free surfaces will not be exact even for uniform infinitesimal strains. Despite this apparent drawback, we feel that this interpretation of the

peridynamic influence function is more natural as it does not artificially inflate the bond-energy/bond stiffness near surfaces. It also allows for a more consistent treatment of bond-damage, because the initial boundary surfaces have the same surface energy as ones created during the bond-failure/crack propagation process.

For a given influence function (2.7), the value of β from the bond-failure-energy function, Equation (6.3), can be computed analytically by evaluating the integrals (6.2), (6.1) for 2D and 3D respectively. For example, computing these integrals using (6.6) and (6.7), respectively, leads to:

$$\int_0^\delta \int_z^\delta \int_{-\cos^{-1}(z/\xi)}^{\cos^{-1}(z/\xi)} \beta \frac{\omega_{2D}(\xi)}{\xi^2} \xi \, d\theta \, d\xi \, dz = \beta \frac{8}{\pi\delta},$$

and

$$\int_0^\delta \int_0^{2\pi} \int_z^\delta \int_0^{\cos^{-1}(z/\xi)} \beta \frac{\omega_{3D}(\xi)}{\xi^2} \xi^2 \sin(\phi) \, d\phi \, d\xi \, d\theta \, dz = \beta \frac{63}{32\delta}.$$

By matching the energy dissipated when severing bonds to the classical fracture energy G_c using Equations (6.2) and (6.1), for 2D and 3D, respectively, we find

$$\beta_{2D} = \frac{\pi}{16} \delta G_c \text{ in 2D},$$

and

$$\beta_{3D} = \frac{16\pi}{63} \delta G_c \text{ in 3D}.$$

Model Summary: The constitutive response for the brittle peridynamic materials in this thesis are assumed to have a free energy given by Equation (6.4), which results

in a force vector-state of

$$\underline{\mathbf{T}}_{(m)}\langle\boldsymbol{\xi}\rangle = \left[\bar{\lambda}\left(\int_{\mathcal{H}(\mathbf{x})}\underline{\phi}\langle\boldsymbol{\xi}\rangle\,\underline{\omega}\langle\boldsymbol{\xi}\rangle\,\underline{\varepsilon}\langle\boldsymbol{\xi}\rangle\;d\boldsymbol{\xi}\right)+2\,\bar{\mu}\,\underline{\varepsilon}\langle\boldsymbol{\xi}\rangle\right]\underline{\phi}\langle\boldsymbol{\xi}\rangle\,\underline{\omega}\langle\boldsymbol{\xi}\rangle\,\underline{c}\langle\boldsymbol{\xi}\rangle^{m-1}\,|\boldsymbol{\xi}|^{-2}\,\underline{\mathbf{Y}}\,\langle\boldsymbol{\xi}\rangle\,, \tag{6.8}$$

with

$$\underline{\phi}\langle\boldsymbol{\xi}\rangle\,(t) = \begin{cases} 0 & \text{for } \underline{\varepsilon}\langle\boldsymbol{\xi}\rangle \geq 0 \text{ and the bond failure criterion, (6.10)} \\ & \text{or (6.11) for 2D and 3D, respectively, is satisfied at} \\ & \text{some time } 0 \leq t_0 \leq t, \\ 1 & \text{otherwise,} \end{cases} \tag{6.9}$$

and where the bond failure criterion is:

$$\bar{\lambda}\,\underline{\varepsilon}\langle\boldsymbol{\xi}\rangle\left(\int_{\mathcal{H}_{2D}}\underline{\phi}\langle\boldsymbol{\xi}\rangle\,\underline{\omega}_{2D}\langle\boldsymbol{\xi}\rangle\,\underline{\varepsilon}\langle\boldsymbol{\xi}\rangle\;d\boldsymbol{\xi}\right)+\bar{\mu}\,\underline{\varepsilon}\langle\boldsymbol{\xi}\rangle\,\underline{\varepsilon}\langle\boldsymbol{\xi}\rangle \geq \frac{\pi}{16}\frac{\delta G_c}{|\boldsymbol{\xi}|^2},\ \underline{\varepsilon}\langle\boldsymbol{\xi}\rangle > 0 \quad \text{in 2D} \tag{6.10}$$

and

$$\bar{\lambda}\,\underline{\varepsilon}\langle\boldsymbol{\xi}\rangle\left(\int_{\mathcal{H}_{3D}}\underline{\phi}\langle\boldsymbol{\xi}\rangle\,\underline{\omega}_{3D}\langle\boldsymbol{\xi}\rangle\,\underline{\varepsilon}\langle\boldsymbol{\xi}\rangle\;d\boldsymbol{\xi}\right)+\bar{\mu}\,\underline{\varepsilon}\langle\boldsymbol{\xi}\rangle\,\underline{\varepsilon}\langle\boldsymbol{\xi}\rangle \geq \frac{16\pi}{63}\frac{\delta G_c}{|\boldsymbol{\xi}|^2},\ \underline{\varepsilon}\langle\boldsymbol{\xi}\rangle > 0 \quad \text{in 3D.} \tag{6.11}$$

The bond failure criterion, (6.10) or (6.11), can be written generically as

$$\underline{s}_{inst}\langle\boldsymbol{\xi}\rangle \geq \underline{s}_c(\xi), \quad \underline{\varepsilon}\langle\boldsymbol{\xi}\rangle \geq 0.$$

In simulations, we use a slightly modified version of the bond failure criterion:

$$\underline{s}_{inst}[\mathbf{x}]\langle\boldsymbol{\xi}\rangle + \underline{s}_{inst}[\mathbf{x}']\langle-\boldsymbol{\xi}\rangle \geq 2\,\underline{s}_c(\xi), \quad \underline{\varepsilon}\langle\boldsymbol{\xi}\rangle \geq 0,$$

to ensure that the two bonds[3] connecting $\mathbf{x}$ and $\mathbf{x}'$ are severed simultaneously, without otherwise affecting the fracture criterion.

The model is formulated so that when broken bonds are under compression, their force contributions are still included. This allows for a naturally treatment of material recontact after fracture, and prevents matter interpenetration even in cases where the material is fully damaged. In addition, the model is constructed such that only bonds under tensile strains are allowed to fail. This model has the property that if all of the bonds are broken across a surface of unit area (in such a way that the bonds are severed asynchronously, i.e., at different times), then the dissipated energy required to create the new fracture surface is exactly the fracture energy, G_c.

A measure of the nonlocal damage at a material point $\mathbf{x}$ is defined by

$$D(\mathbf{x}) := 1 - \frac{1}{d} \int_{\mathcal{H}(\mathbf{x})} \underline{\omega}\langle \boldsymbol{\xi} \rangle \, \underline{\phi}\langle \boldsymbol{\xi} \rangle \, d\boldsymbol{\xi}, \tag{6.12}$$

where d is the dimension: 2 or 3, for 2D and 3D, respectively. This parameter is convenient for detecting the initiation and propagation of fracture surfaces, as it 'counts' the number of material points which are still interacting with the point $\mathbf{x}$. It can also be interpreted as a measure of the amount of free surface near the material point $\mathbf{x}$. Material points near newly created fracture surfaces will have a higher value of nonlocal damage D, as will points near external boundaries of the body.

For completeness, we show that the failure model proposed in this section also satisfies the second law of thermodynamics. In order to satisfy a version of the Clausius-Duhem inequality (as given in Appendix A.2), it is necessary that

$$-\psi_{,\underline{\phi}}\langle \boldsymbol{\xi} \rangle \, \dot{\underline{\phi}}\langle \boldsymbol{\xi} \rangle \geq 0, \quad \forall \boldsymbol{\xi},$$

[3]There is a bond at $\mathbf{x}$ to $\mathbf{x}'$, as well as a bond at $\mathbf{x}'$ to $\mathbf{x}$.

where the free energy ψ is given by Equation (6.4). From Equations (6.8) and (6.9):

$$\psi_{,\underline{\phi}}\langle\boldsymbol{\xi}\rangle = \underline{s}_{inst}\langle\boldsymbol{\xi}\rangle = \bar{\lambda}\,\underline{\omega}\langle\boldsymbol{\xi}\rangle\,\underline{\varepsilon}\langle\boldsymbol{\xi}\rangle\left(\int_{\mathcal{H}}\underline{\phi}\langle\boldsymbol{\xi}\rangle\,\underline{\omega}\langle\boldsymbol{\xi}\rangle\,\underline{\varepsilon}\langle\boldsymbol{\xi}\rangle\;d\boldsymbol{\xi}\right) + \bar{\mu}\,\underline{\omega}\langle\boldsymbol{\xi}\rangle\,\underline{\varepsilon}\langle\boldsymbol{\xi}\rangle\,\underline{\varepsilon}\langle\boldsymbol{\xi}\rangle\,,$$

for $\underline{\varepsilon}\langle\boldsymbol{\xi}\rangle > 0$ and $\psi_{,\underline{\phi}}\,\langle\boldsymbol{\xi}\rangle = 0$ otherwise. For $\underline{\varepsilon}\langle\boldsymbol{\xi}\rangle > 0$, we have $\dot{\phi}\langle\boldsymbol{\xi}\rangle \leq 0$ and $\dot{\phi}\langle\boldsymbol{\xi}\rangle < 0$ only if $\underline{s}_{inst}\langle\boldsymbol{\xi}\rangle \geq \underline{s}_c(|\boldsymbol{\xi}|) > 0$. This result establishes that the laws of thermodynamics are satisfied, and a rigorous accounting of the various energies (elastic, kinetic, and dissipation due to fracture) is therefore possible.

6.2 Validation

The proposed model for brittle fracture was implemented in C++ using an appropriately modified version of the standard particle discretization strategy described in Section 3.1, and parallelized with C++/MPI using a ghost particle strategy [80]. The resulting approach is then applied to two test problems in order to validate the ability of the model to capture experimentally observed fracture patterns, and to confirm that the dissipated fracture energy and observed crack patterns are insensitive to the discretization size.

6.2.1 Edge-on impact test of PMMA plates

As an initial test to validate the brittle peridynamic material model proposed in Section 6.1.3, we simulate an edge-on impact test designed to initiate the propagation of a Mode-I crack. Schardin [101, 102] conducted the first edge-on impact tests in the 1930s to investigate fracture patterns in glass. More recently, Rosakis and co-workers have used edge-on impact tests to study crack growth in bi-materials [59, 105]. The numerical simulations presented in this section are inspired by tests of Umberger and Love [115] who conducted edge-on impact test using a gas gun to accelerate an aluminum cylinder to impact a pre-notched PMMA target in a one-point bend

configuration (see Figure 6-2). Coherent Gradient Sensing (CGS) techniques [112] were used to obtain information about the crack propagation including the evolution of the near-tip displacement gradients and the crack tip speed. An experimental observation was that at low impact velocities a single Mode-I crack is propagated in the x direction from the notch tip. Crack branching occurs for higher initial impact velocities and the number of cracks generally increases as the velocity is increased. A few examples images from the experimental results in [115] are reproduced in Figure 6-3.

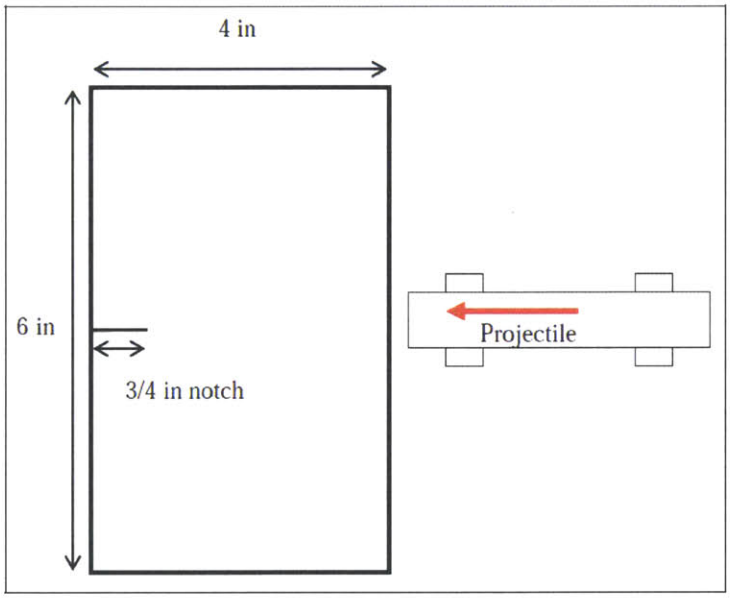

Figure 6-2: A schematic of the specimen and impactor geometry for the Mode-I edge-on impact tests of Umberger and Love on pre-notched PMMA plates. Figure reproduced from [115].

To model this experiment, we use material properties for the target corresponding to that of PMMA, with density $\rho = 1180$ kg/m^3, elastic modulus $E = 3.5$ GPa, and Poisson's ratio $\nu = 0.35$. For plane stress in 2D, these elastic constants correspond to peridynamic Lamé constants of $\bar{\mu} = 2.6$ GPa and $\bar{\lambda} = 0.1$ GPa. The fracture energy for the PMMA was taken to be $G_c = 400$ J/m^2. The target geometry is as depicted in Figure 6-2. The projectile geometry was simplified for these 2D simulations to have a square shape with a length of 0.02 m for each edge. The elastic constants for the

projectile correspond to those of aluminum, with $E = 70$ GPa, $\nu = 0.33$ and $\rho = 2700$ kg/m^3. Fracture is suppressed in the aluminum projectile. In most simulations, a relatively large peridynamic horizon of $\delta = 0.0055$ m is used.

Simulation results for a fixed particle density and peridynamic horizon size are shown in Figure 6-4 for varying initial impact velocities. In this figure and throughout this chapter, the plotted material damage corresponds to a discrete version of the nonlocal damage, Equation (6.12). Recall that this definition of material damage 'counts' the number of neighbors a given particle it is still interacting with, and can be interpreted as a measure of the amount of nearby free surface. As a results, particles which are close to newly created fracture surfaces will show higher values of nonlocal damage D, as will particles which are near the external boundary of the discretized domain.

The results in Figure 6-4 demonstrate that the proposed brittle damage model is capable of qualitatively capturing the experimentally observed trend of increasing number of cracks with increasing initial impact velocity.[4] At sufficiently low velocities, the numerical results also exhibit the clear propagation of a single Mode-I crack. At sufficiently high velocities, fracture directly under the impactor is observed, again consistent with the experiments.

[4]These comparison are only qualitative, as we are making several simplifying assumptions, e.g., the projectile geometry.

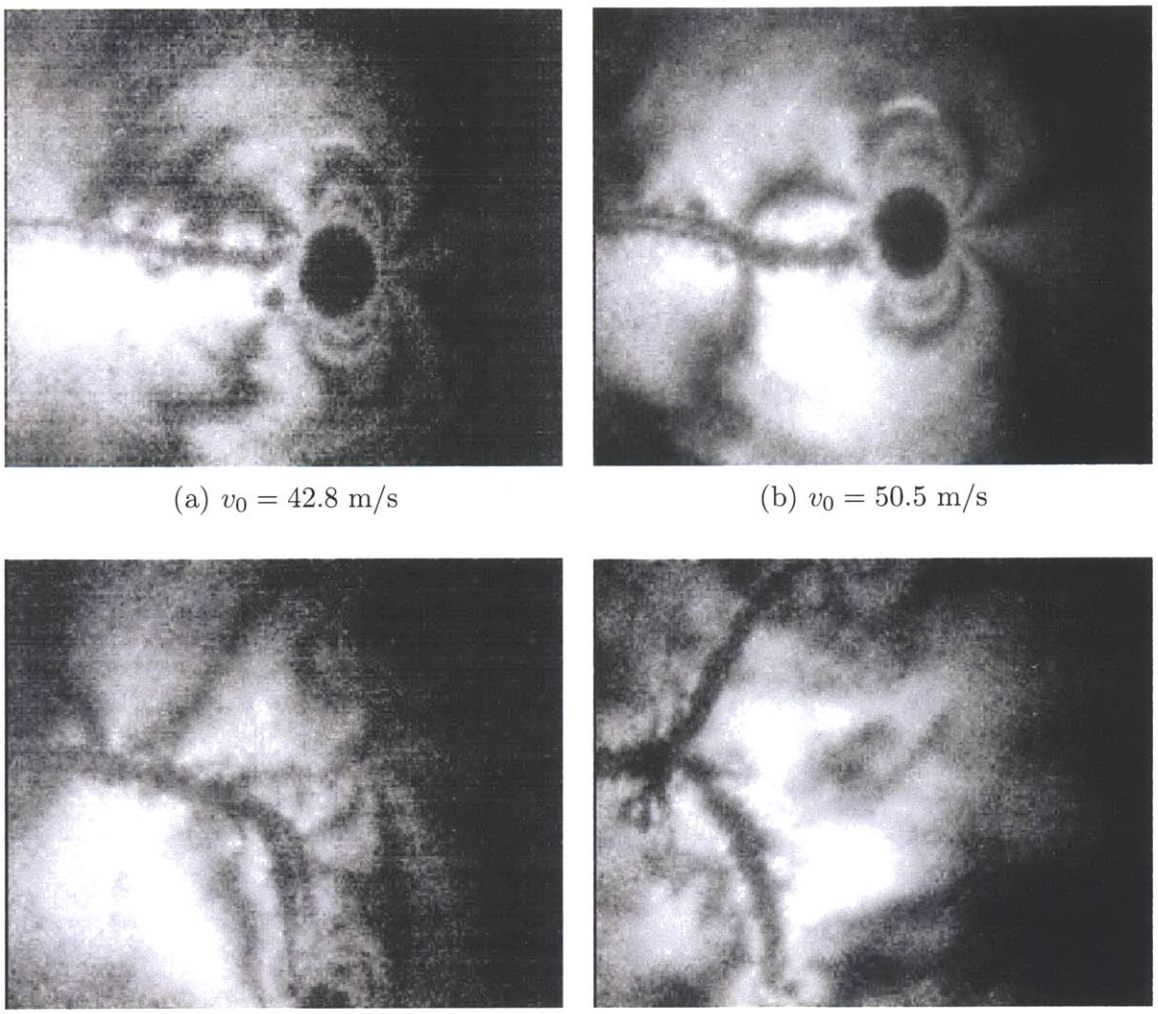

(a) $v_0 = 42.8$ m/s

(b) $v_0 = 50.5$ m/s

(c) $v_0 = 58.3$ m/s

(d) $v_0 = 65.9$ m/s

Figure 6-3: Experimental results (reproduced from [115]) with different initial impact velocities for edge-on impact of PMMA. Results show a transition from Mode-I fracture to crack branching at higher velocities. Black and white contours depict deformation gradients from Coherent Gradient Sensing.

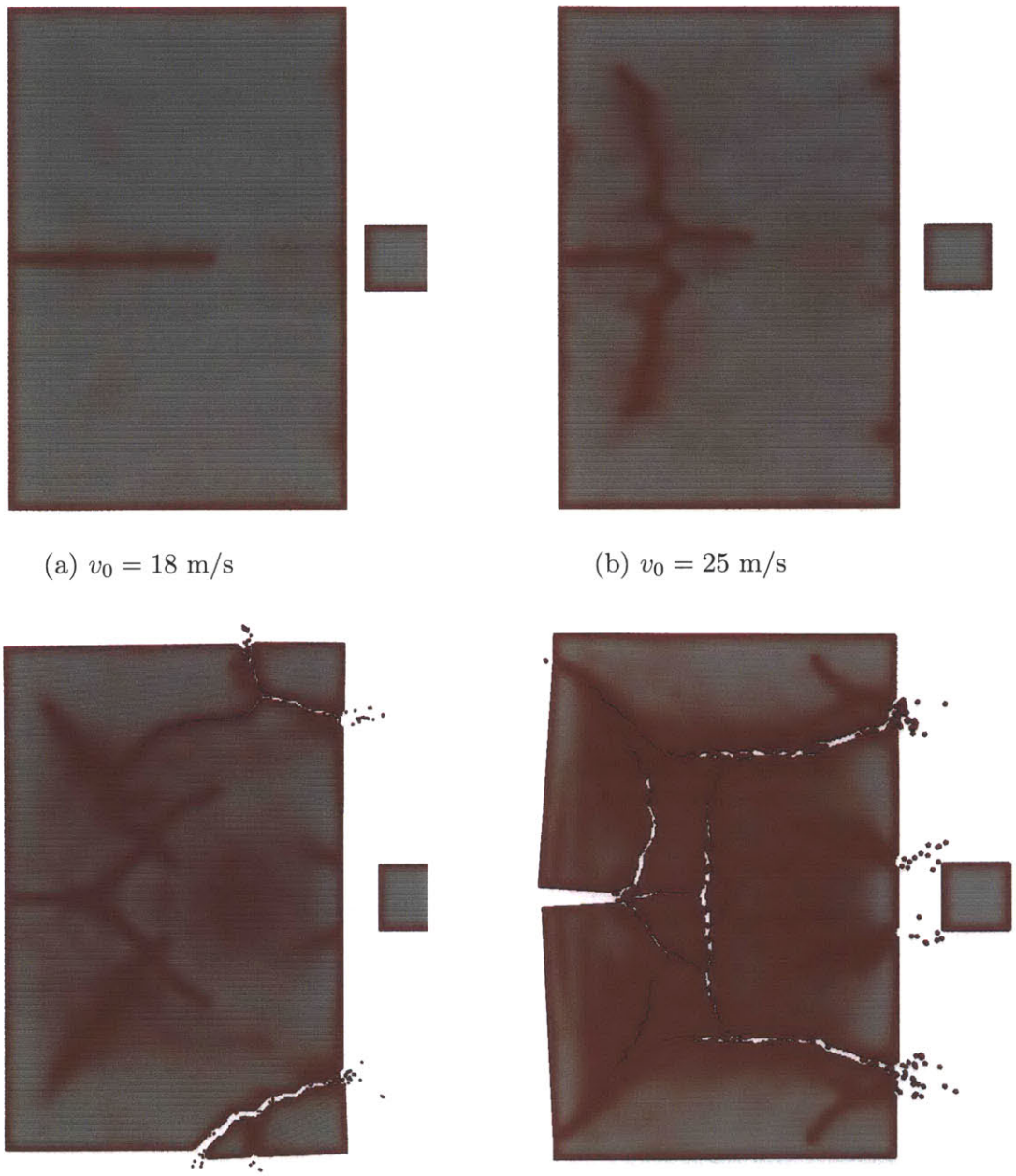

(a) $v_0 = 18$ m/s

(b) $v_0 = 25$ m/s

(c) $v_0 = 35$ m/s

(d) $v_0 = 50$ m/s

Figure 6-4: Nonlocal material damage at $t = 0.001$ s for a discretization with 61,600 particles and a horizon of $\delta = 0.0055$ m, with varying initial impact velocities.

In the simulations, we are able to carefully track energy histories. In Figure 6-11, the elastic energy, kinetic energy and dissipated fracture energy is plotted over time for the case $\delta = 0.0055$ m, $v_0 = 15$ m/s, and a relatively fine particle density with 61,600 particles. The elastic energy and kinetic energy are directly computed from the discretized constitutive formulation. The dissipated fracture energy is computed as a sum over time of the energy dissipated by severing bonds, which is estimated to be the instantaneous bond energy, defined in Section 6.1.2. An important observation is that the sum of all the energies (total energy) remains constant throughout the course of the simulation. That this should occur may seem obvious, but this conservation property is not explicitly encoded in the simulations. The fact that the total energy is conserved in simulations confirms that it is the instantaneous bond energy that is dissipated when bond are broken. This validates the assumptions of the approach for modeling brittle fracture described in Section 6.1.3.

To investigate the convergence behavior of the proposed approach, we restrict attention to the case $\delta = 0.0055$ and $v_0 = 15$ m/s. The nonlocal material damage is shown at various time-steps using different particle densities in Figures 6-5–6-9. Results using an unstructured particle distribution are shown in Figure 6-10. It can be observed that the simulations are relatively insensitive to the particle density, a remarkable feature for brittle impact simulations. Figure 6-12 provides a more direct comparison between the results for the various discretization levels by plotting the dissipated fracture energy over time. This comparison indicates that after a sufficient level of resolution is achieved (more than 39,4242 particles in this case), the dissipated energy is relatively insensitive to the particle density for both structured and unstructured particle distributions (at least over short periods of time).

It remains to confirm that the energy dissipated in simulations is consistent with the fracture energy, G_c, which is entered as an input parameter. An approximate value for the simulated fracture energy can be obtained by dividing the total dissipated

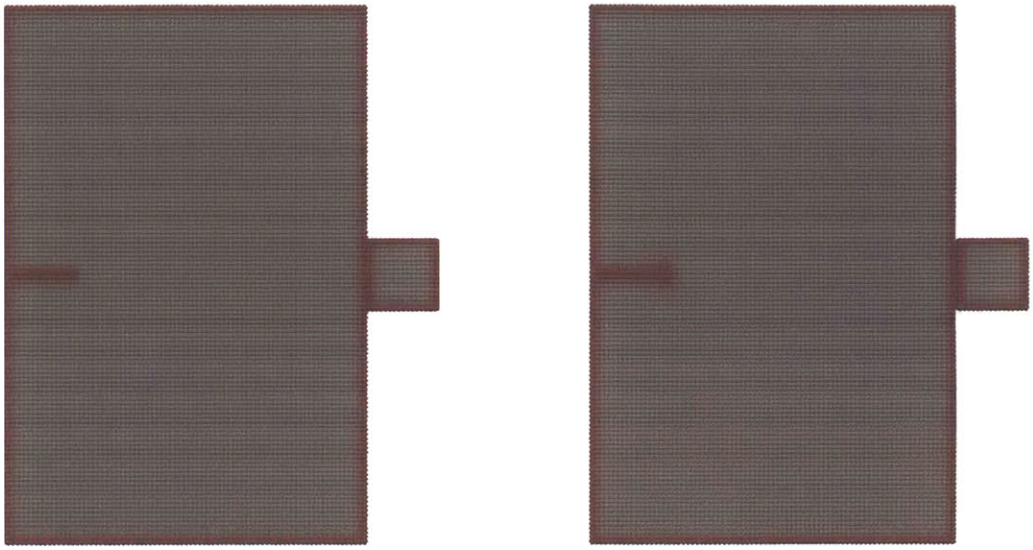

(a) $t = 0$ s (b) $t = 0.0002$ s

Figure 6-5: Nonlocal material damage at $t = 0$ s and $t = 0.0002$ s for 9,856 particle discretization with initial impact velocity of $v_0 = 15$ m/s.

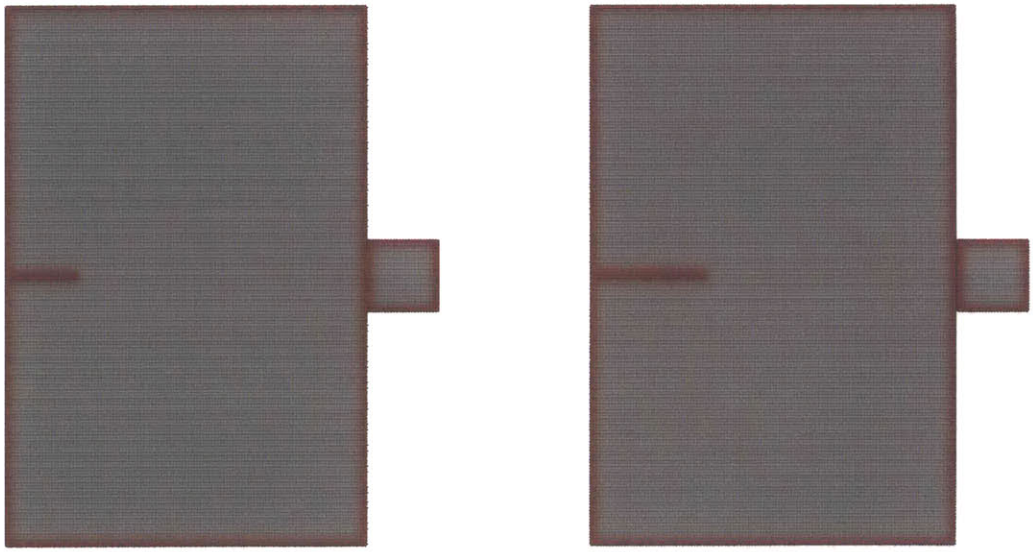

(a) $t = 0$ s (b) $t = 0.0002$ s

Figure 6-6: Nonlocal material damage at $t = 0$ s and $t = 0.0002$ s for 22,176 particle discretization with initial impact velocity of $v_0 = 15$ m/s.

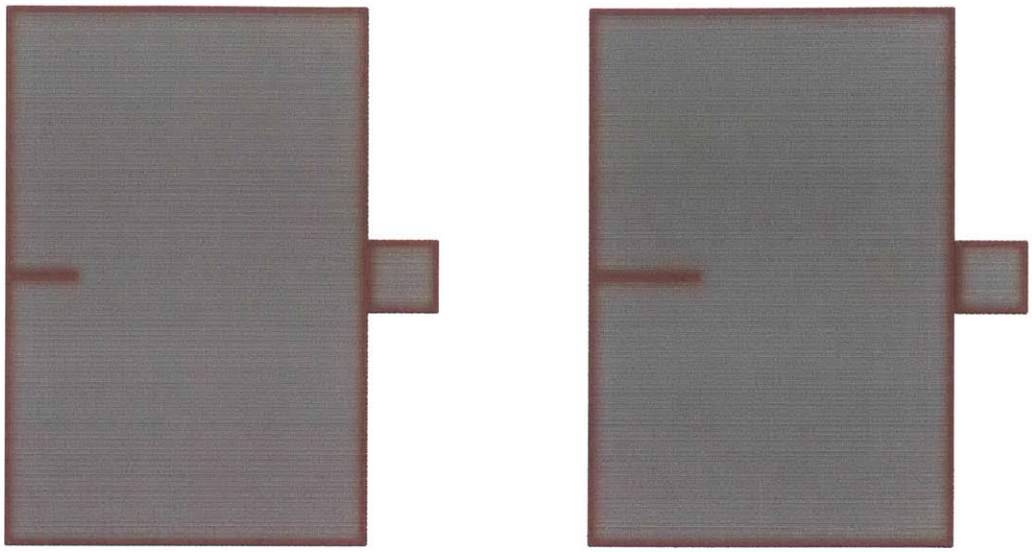

(a) $t = 0$ s (b) $t = 0.0002$ s

Figure 6-7: Nonlocal material damage at $t = 0$ s and $t = 0.0002$ s for 39,424 particle discretization with initial impact velocity of $v_0 = 15$ m/s.

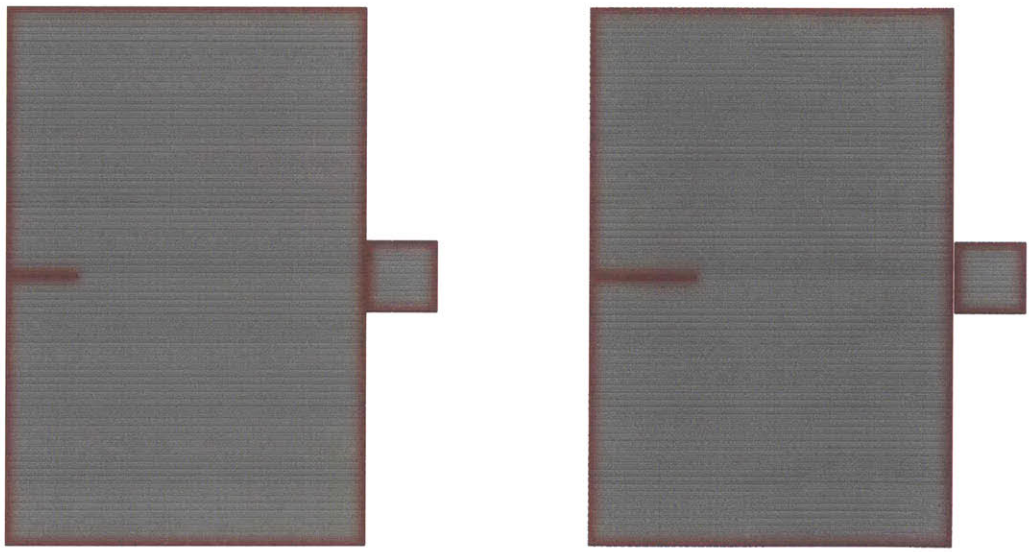

(a) $t = 0$ s (b) $t = 0.0002$ s

Figure 6-8: Nonlocal material damage at $t = 0$ s and $t = 0.0002$ s for 61,600 particle discretization with initial impact velocity of $v_0 = 15$ m/s.

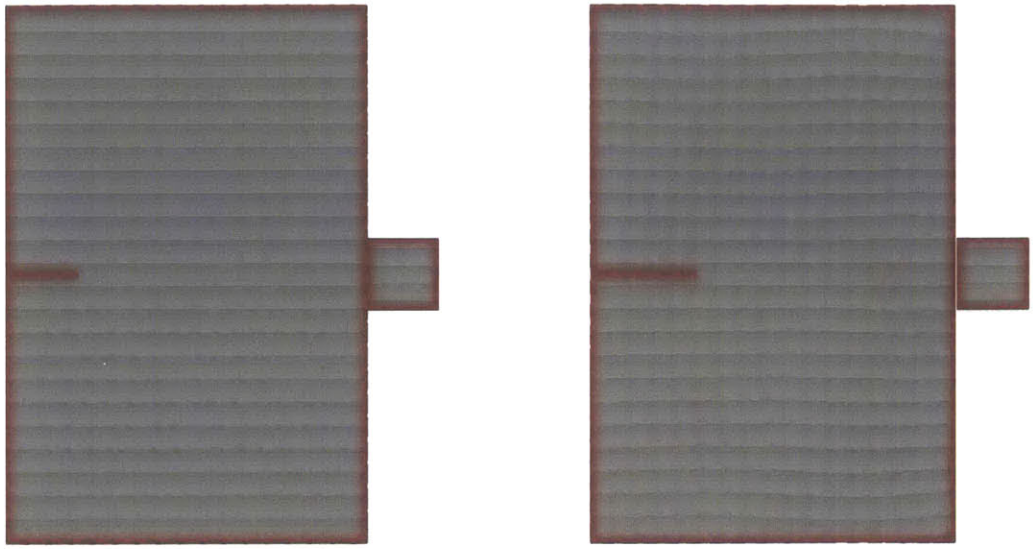

(a) $t = 0$ s (b) $t = 0.0002$ s

Figure 6-9: Nonlocal material damage at $t = 0$ s and $t = 0.0002$ s for 109,104 particle discretization with initial impact velocity of $v_0 = 15$ m/s.

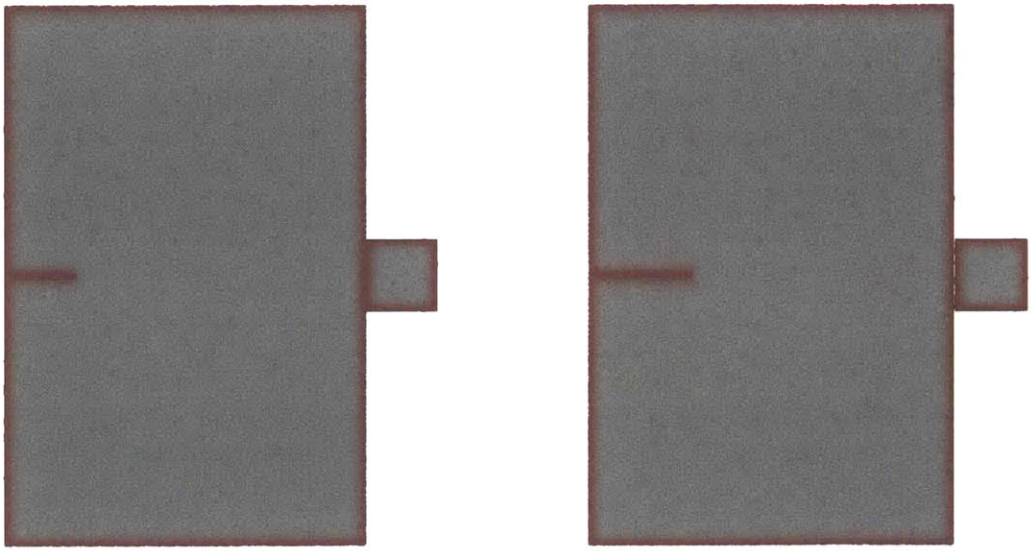

(a) $t = 0$ s (b) $t = 0.0002$ s

Figure 6-10: Nonlocal material damage at $t = 0$ s and $t = 0.0002s$ for unstructured particle distribution (109,867 particles) with initial impact velocity of $v_0 = 15$ m/s.

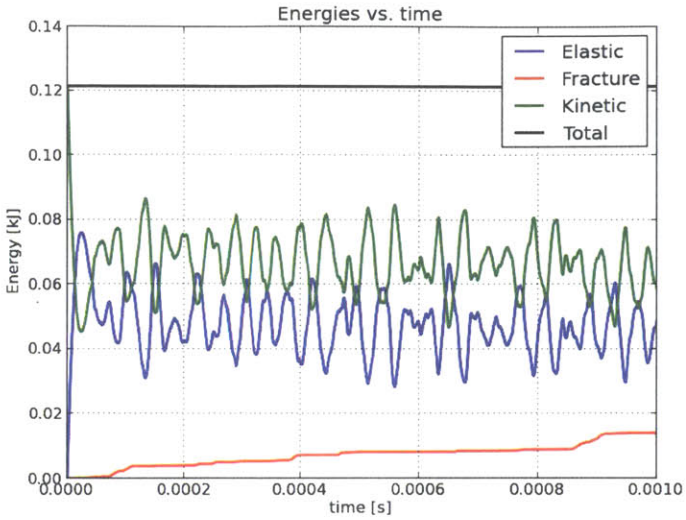

Figure 6-11: Discretized energies plotted over time for the case $v_0 = 15$ m/s, $\delta = 0.0055$ m, using an unstructured particle distribution using 109,867 particles.

fracture energy by the measured length of crack propagation at some time, t.[5] In Table 6.1, we show the results of this analysis for several different discretization sizes, an unstructured particle distribution and even using a different peridynamic horizon size, δ. The results indicate that after a sufficient level of resolution is achieved, the computed fracture energy is fairly constant and is remarkably close to the input value of $G_c = 400$ J/m^2. It is worth emphasizing that there is no prior guarantee that the simulated fracture energy be similar to the input parameter, as such a correspondence would require a highly localized fracture plane to develop.

[5]Crack propagation lengths were approximated from Figures 6-5–6-10 by counting pixels.

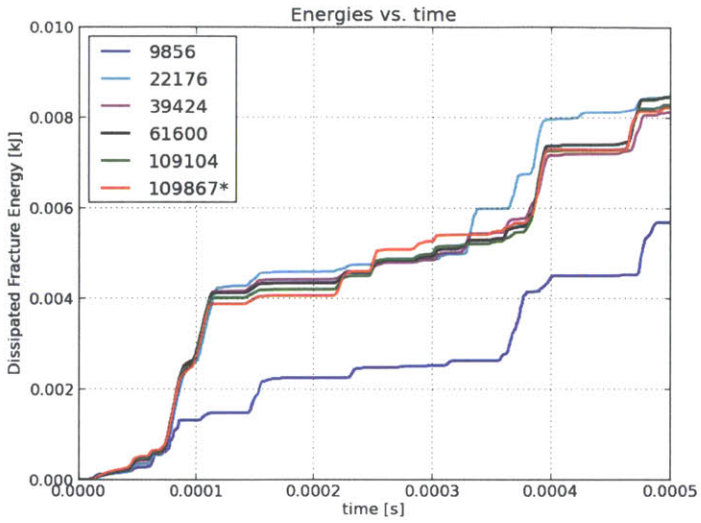

Figure 6-12: Dissipated energy over time for varying particle densities, with $v_0 = 15$ m/s. The red curve uses an unstructured particle distribution.

number of discrete particles	crack length	dissipated energy	cohesive energy
9,856	4 mm	2.5 J	620 J/m^2
22,176	12 mm	4.6 J	400 J/m^2
39,424	11 mm	4.4 J	420 J/m^2
61,600	11 mm	4.4 J	410 J/m^2
109,104	10 mm	4.2 J	420 J/m^2
109,867 (unstructured)	10 mm	4.1 J	410 J/m^2

Table 6.1: Comparison of crack propagation length, dissipated energy and the estimated cohesive energy for different particle densities after $t = 0.0002$ s, using $\delta = 0.0055$ m.

Results for a few different time-steps using a higher initial impact velocity of $v_0 = 35$ m/s with a 61,600 particle discretization are shown in Figure 6-13. This result shows the initial (albeit brief) propagation of a Mode-I crack, followed by crack branching, similar to what is observed in the experimental results of Figure 6-3 for higher initial velocities.

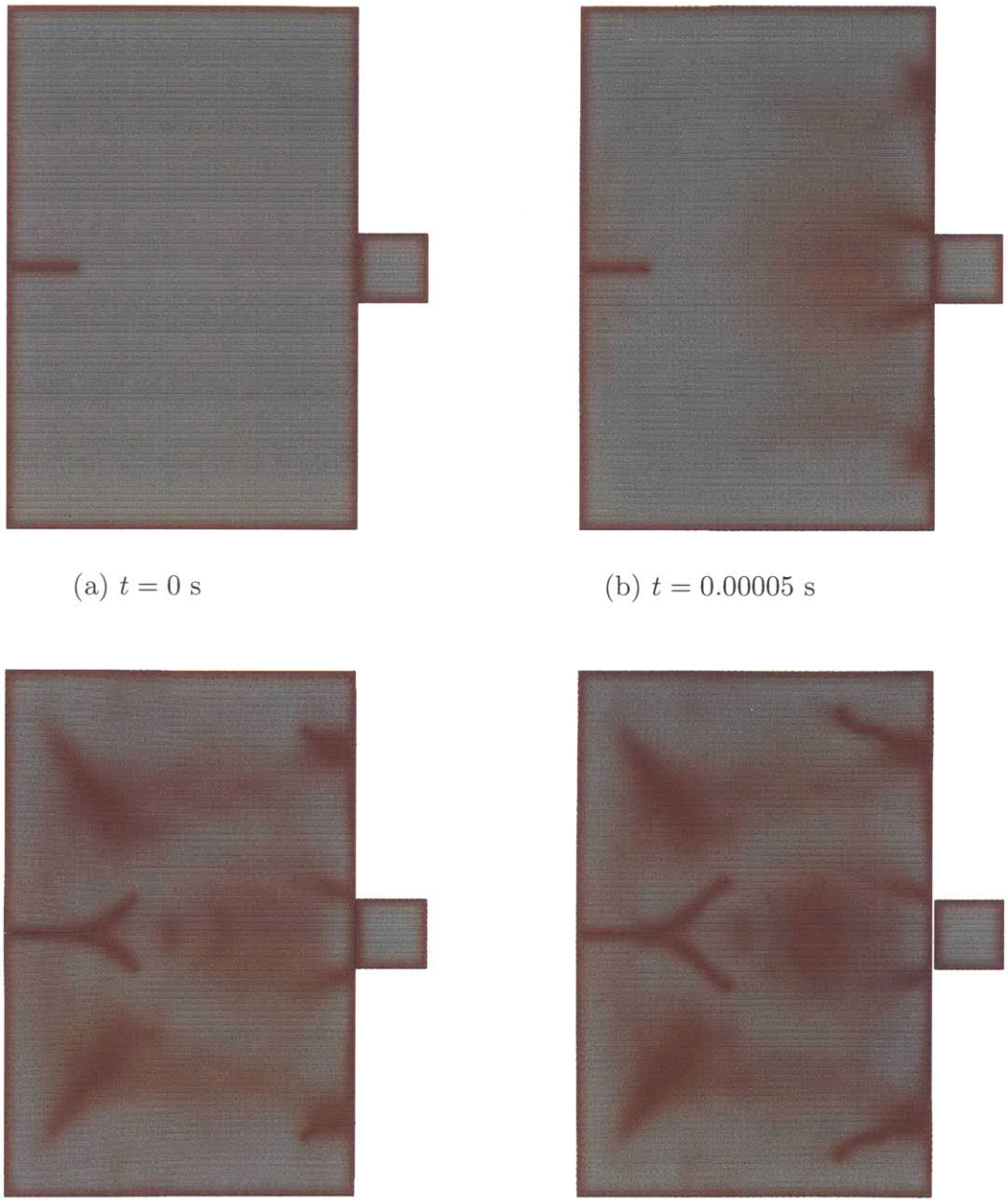

(a) $t = 0$ s

(b) $t = 0.00005$ s

(c) $t = 0.0001$ s

(d) $t = 0.00015$ s

Figure 6-13: Nonlocal material damage at various time-steps for simulation with $\delta = 0.0055$, $v_0 = 35$ m/s, and 61,600 particles.

Up to this point, we have simplified matters slightly by considering only a fixed horizon size, δ, as the effect of the peridynamic horizon is not a primary focus of this thesis. A more detailed discussions of this important consideration in peridynamic material modeling can be found in [121, 29]. As a representative case showing the effect of changing the horizon size for the problem considered here, in Figure 6-14 we show several time-steps using a smaller horizon size of $\delta = 0.0015$ m, with a significantly higher particle density and an initial impact velocity of $v_0 = 35$ m/s. Similar to the case using $\delta = 0.0055$ m, this result shows the initial propagation of a Mode-I crack, followed by crack branching. In this case, the estimated cohesive energy in the simulation was found to be 380 J/m^2, once again close to the input parameter value of 400 J/m^2.

In Figure 6-15, we show the damage profile at $t = 0.001$ using different initial impact velocities and a horizon size of $\delta = 0.0015$ m. The experimentally observed trend that the number of branches increases for increasing initial velocity is again observed, as was the case for the larger horizon size. Another feature of the peridynamic approach is that crack coalescence, and therefore fragmentation, is handled naturally, as can be seen in Figure 6-15d.

In order to test the ability of the computational framework to simulate three dimensional problems, a 3D discretization with 573,346 particles was created, where the in-plane target and impactor geometries are the same as in the 2D case, and the thicknesses are 0.02 m. Two example solutions using a peridynamic horizon of $\delta = 0.004$ m are shown in Figure 6-16, where the expected trend of crack branching occurring at higher initial impact velocities is again observed.[6] These results further highlight the remarkable robustness of the computational framework developed in this thesis.

[6]We do not expect to get results which are quantitatively similar to the experimental results in Figure 6-3, as we are not fully modeling the projectile.

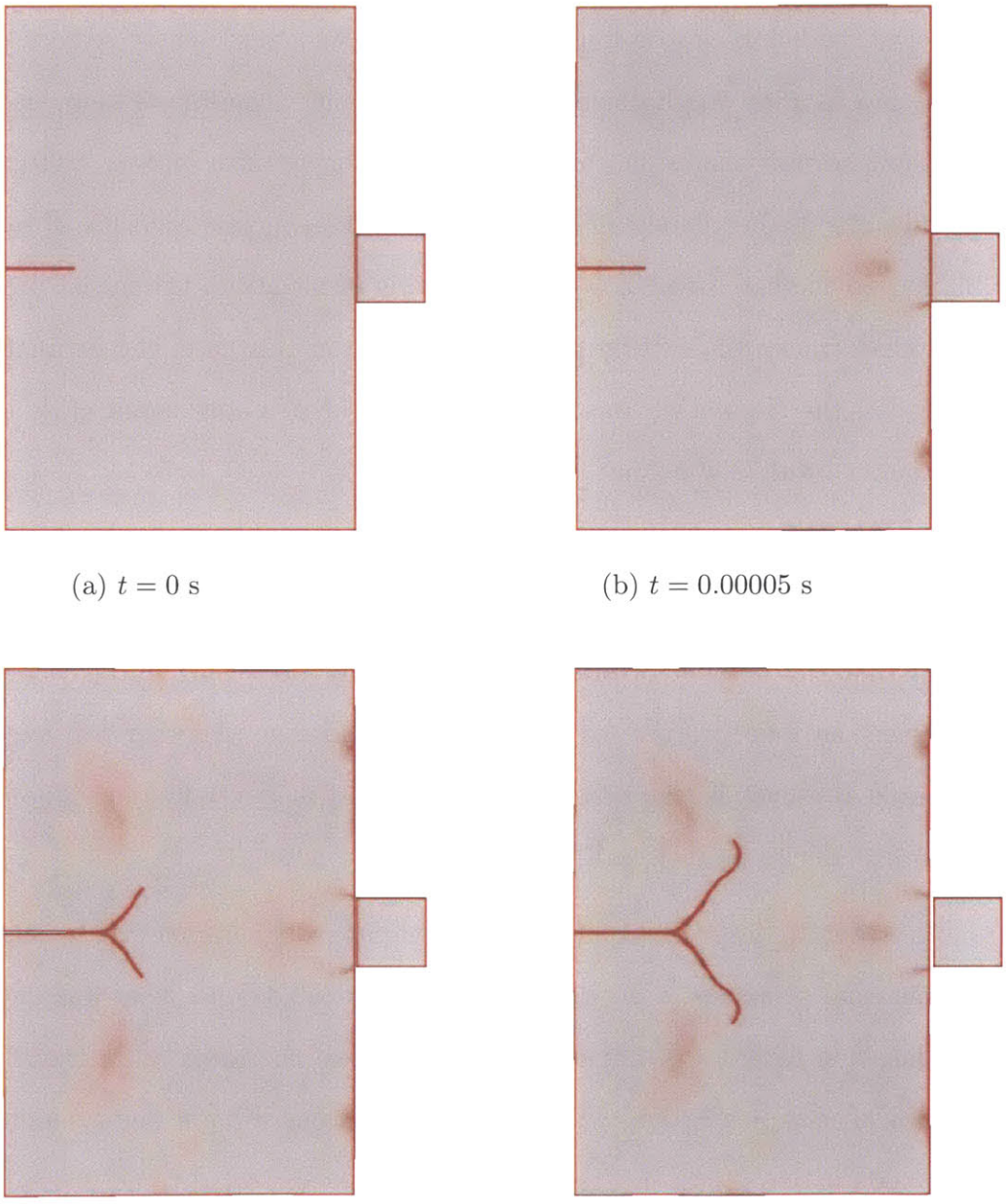

(a) $t = 0$ s

(b) $t = 0.00005$ s

(c) $t = 0.0001$ s

(d) $t = 0.00015$ s

Figure 6-14: Nonlocal material damage at various time-steps for simulation with $\delta = 0.0015$, $v_0 = 35$ m/s, and 431,636 particles.

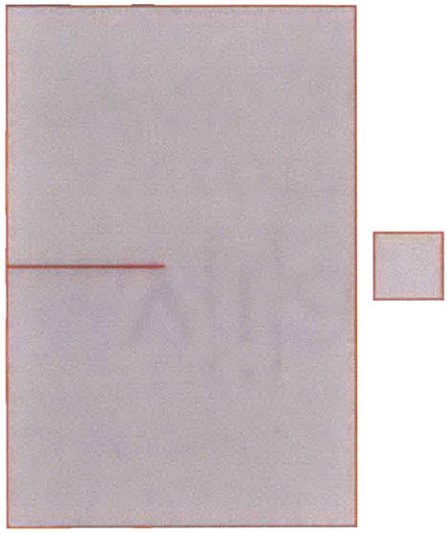

(a) $v_0 = 15$ m/s

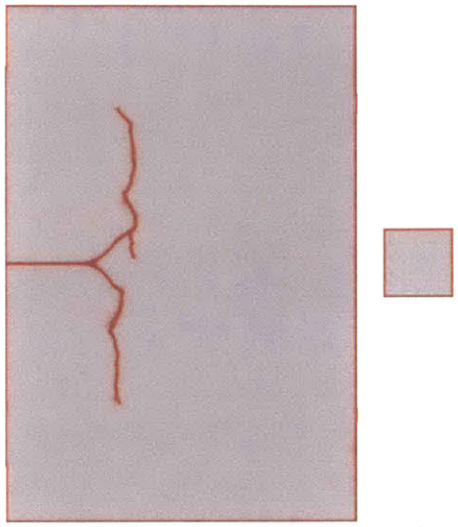

(b) $v_0 = 25$ m/s

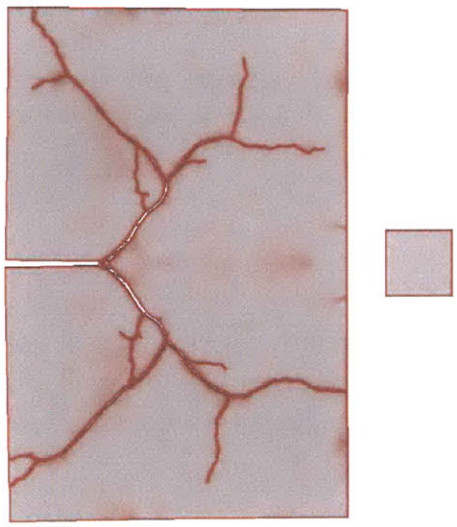

(c) $v_0 = 35$ m/s

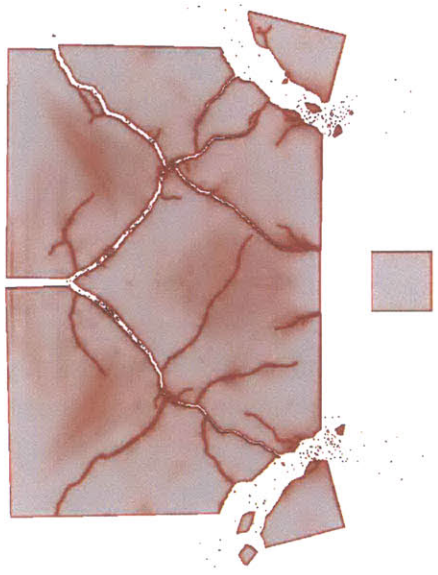

(d) $v_0 = 50$ m/s

Figure 6-15: Nonlocal material damage at $t = 0.005$ s with different initial impact velocities, and 431,636 particles.

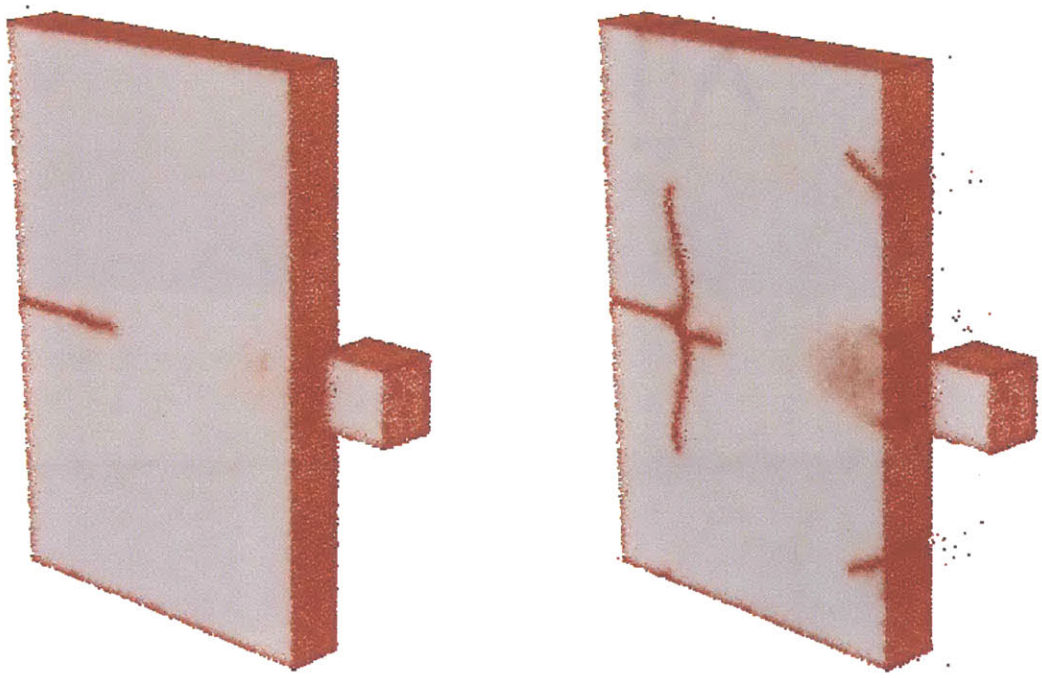

(a) $v_0 = 30$ m/s (b) $v_0 = 50$ m/s

Figure 6-16: Nonlocal material damage at $t = 0.001$ s with different initial impact velocities for edge-on impact simulations in 3D. A discretization with 573,346 particles, using a horizon size of $\delta = 0.004$ m is shown sliced through the thickness of the plate.

6.2.2 Kalthoff test

The Kalthoff test, which is based on experimental results by Kalthoff and coworkers [11, 55, 56], has emerged as a benchmark problem for numerical approaches to brittle and ductile failure modeling [125, 62]. The test consists of a plate with two edge notches, as depicted in Figure 6-17, impacted by a projectile with initial velocity v_0. The two initial notches are equidistant from the center-line of the target and are separated by distance equal to the diameter of the projectile. Peridynamic simulations of the Kalthoff test have previously been demonstrated using the simpler bond-based version of the theory [41].

For the simulations in this thesis, the notches are separated by a distance of 0.05 m, while the height of the target is 0.2 m and its width is 0.1 m. The material parameters used are a density $\rho = 8000$ kg/m^3, Young's modulus $E = 190$ GPa, Poisson's ratio $\nu = 0.3$ and fracture energy $G_c = 22,000$ J/m^2. We use an initial impact velocity of $v_0 = 16$ m/s, which in experiments resulted in brittle fracture behavior. Results using different particle densities are shown in Figure 6-18, where a fairly consistent angle of crack propagation is observed of around 66°, similar to both experimentally observed results [11, 55] which find a propagation angle of around 70° and other computational approaches [125] which also typically under-predict the crack angle slightly.[7] The difference in appearance for Figure 6-18d compared to the rest of the images is due to a change in visualization which was required for the larger number of particles. Table 6.2 summarizes the computed propagation angle for the different particle densities. For a smaller peridynamic horizon size, the crack propagation angle increases slightly towards the experimentally observed value.

[7] To handle the interface sliding which occurs in the Kalthoff test, the damage model was modified slightly by permanently turning off the interaction forces for damaged bonds, even under compressive strains.

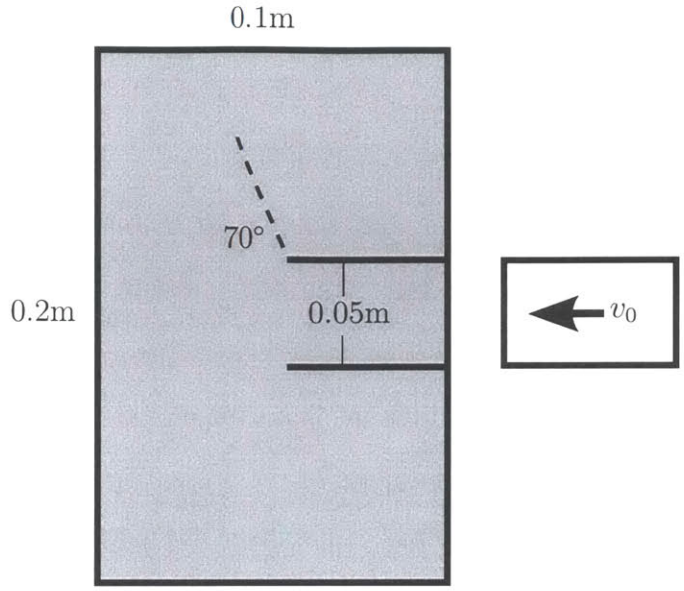

Figure 6-17: Schematic of the Kalthoff experiment[56].

number of particles	angle (degrees)
62,875	66°
92,060	65°
138,037	67°
456,652 ($\delta = 0.00185$)	68°

Table 6.2: Comparison of Kalthoff test crack propagation angle for different particle densities using $\delta = 0.005$ m (unless otherwise specified).

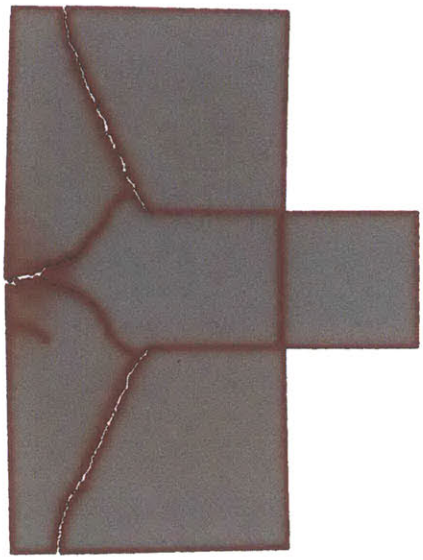

(a) Number of particles: 62,875, $\delta = 0.005$

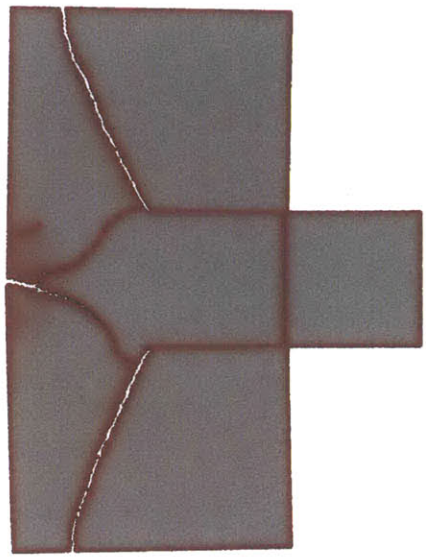

(b) Number of particles: 92,060, $\delta = 0.005$

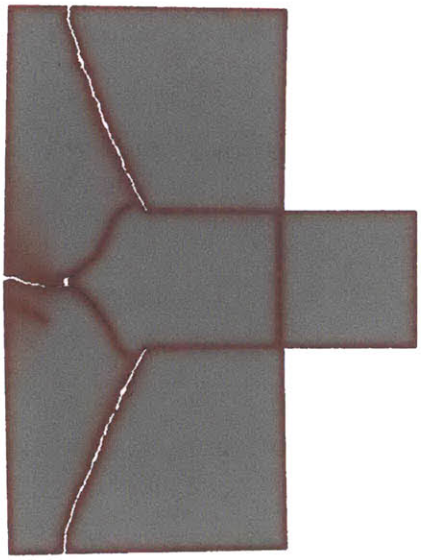

(c) Number of particles: 138,037, $\delta = 0.005$

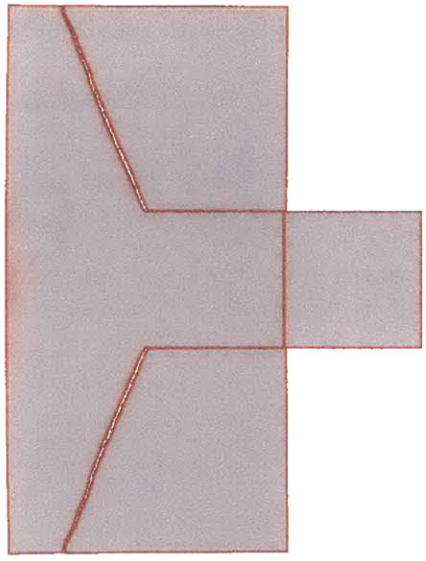

(d) Number of particles: 456,652, $\delta = 0.0019$

Figure 6-18: Nonlocal material damage with different particle densities and horizon sizes for the Kalthoff test.

6.2.3 Scalability test

As a final test of the computational framework, we provide a demonstration of the scalability of our C++/MPI implementation. A standard ghost particle approach (see, e.g., [80]) is used and shown to exhibit good scalability. Several existing peridynamics codes have also demonstrated good scalability. These include an implementation of peridynamics in the molecular dynamics code LAMMPS [67], which is known to be highly scalable up to tens of thousands of processors. In addition, there is Peridigm [66] which is a massively parallel, open-source computational peridynamics code based on Sandia National Laboratories' agile software components efforts.

Strong scalability results for the code developed in this thesis using two different particle discretizations, each with two different horizon sizes, are shown in Figure 6-19. We see that even for relatively small problem sizes the scalability is maintained up to hundreds of processors, which is the limit of the machine we had access to. Given that the parallelization strategy we use is similar to what is used in existing codes, we anticipate that this scalability will continue for sufficiently large particle discretizations. It can be observed in Figure 6-19 that the scalability is slightly worse for larger peridynamic horizon sizes. This is expected as larger horizons require more particle communications per sub-domain.

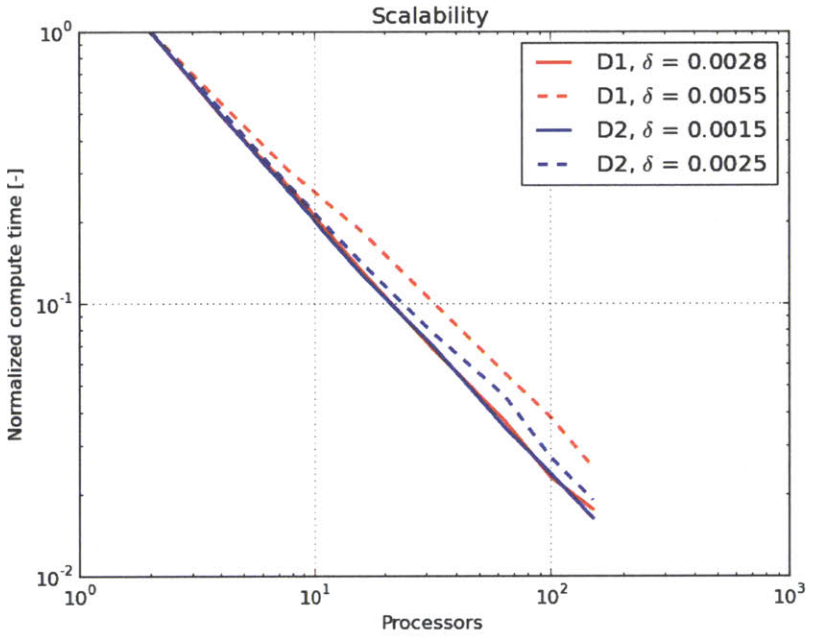

Figure 6-19: Scalability plot for two different particle discretizations: D1 has 109,104 particles, D2 has 431,636 particles, each using two different peridynamic horizons. The plot shows the normalized compute time (compute time divided by the compute time using only 2 processors) vs the number of processors. Near perfect scalability is observed for the smaller horizon sizes.

Chapter 7

Incorporating classical damage models in peridynamics

In this chapter, we describe an approach for incorporating classical continuum damage models in the state-based theory of peridynamics. The discussion below is adopted from [69], and uses examples which have also previously been reported (in less detail) in [68].

A key remaining challenge in peridynamics and its associated discretization methods is how to describe material failure in ways which are consistent with established models of fracture and damage. In the original formulation of peridynamics, usually referred to as the bond-based theory, fracture is commonly incorporated by means of a critical relative displacement criterion, i.e., when the change in distance between two particles reaches a critical value u_c, their bond is irreversibly broken [95, 94]. A particle-based discretization of peridynamic was proposed in [94], where it was demonstrated that the critical bond elongation u_c can be related to the fracture energy G_0 for brittle materials. This approach has been used for modeling fracture and failure of composites, nanofiber networks and polycrystals [22], to simulate ballistic impact on brittle plates [67], to study crack nucleation in peridynamic solids [100], and to

study dynamic crack propagation and crack branching [121]. The main limitation of the bond-based peridynamic theory is that it only considers pairwise interactions between particles. As is well known, a direct consequence of this assumption is that the effective Poisson's ratio for isotropic linear materials is fixed at the value of $\nu = 0.25$ [93]. An immediate repercussion of this limitation is the inadequacy of the bond-based peridynamics formulation in situations involving incompressible deformations, e.g. plasticity.

To address these issues, Silling *et al.* developed the so called state-based peridynamics formulation [98] (summarized in Chapter 2), which makes it possible to incorporate general constitutive models. In particular, the new formulation introduces a constitutive correspondence framework which enables the use of traditional constitutive models formulated in terms of a continuum local measure of deformation (i.e., the deformation gradient tensor, $\mathbf{F}$, see Section 2.2.1). Recently, this approach was used to model viscoplastic deformations in metals [51, 52]. The ability to incorporate classical constitutive models also opens the path for using classical continuum damage models within the peridynamics framework.

Existing state-based peridynamic damage modeling approaches in the literature are based on permanently modifying the peridynamic influence function by instantly setting it equal to zero and severing the bond when a failure criterion is achieved [51, 78]. Within the context of ordinary state-based peridynamics, the role of the influence function has been explored in [79], and a critical bond elongation criterion has been proposed in [78] which is similar to the damage modeling approach commonly used in bond-based peridynamics [95, 94, 22, 67, 100, 121]. A severing criterion based on a maximum elastic bond energy was proposed in [51] for the constitutive correspondence formulation and calibrated to dissipate a pre-specified fracture energy when a new surface is created. These approaches appear to be successful for modeling brittle fracture. However, there are situations (e.g. in ductile fracture), in which

damage evolution and failure are known to depend on quantities such as the stress triaxiality, Lode angle, and possibly other parameters characterizing the local stress state [7, 54, 6]. It would therefore be desirable to be able to incoporate classical damage models whose primary objective is the description of damage mechanisms and their evolution in a physics-based or phenomenological manner.

A more general framework for modeling damage within peridynamics has recently been proposed [97]. The theory constitutes a thermodynamically consistent extension of state-based peridynamics where accumulated damage is represented by a *damage-state*. However, the requirement to introduce a peridynamic damage-state makes it impossible to use existing damage models directly, and the necessary reformulation within this framework has yet to be done for general damage models. Specifically, it is not clear how the Johnson-Cook damage model adopted in the examples in this chapter should be modified to fit this general framework.

The main objective of this chapter is to develop a state-based peridynamics formulation where classical (local) continuum damage models can be incorporated without modification. It is found that a direct implementation of damage models within the constitutive correspondence framework leads to instabilities associated with unphysical diffusion of the damage zone. To address this issue, we employ a peridynamic bond degradation criterion based on the accumulated material damage. As damage evolves at a material point, the peridynamic influence function for bonds in the neighborhood is decreased so that in the limit of full damage its interaction with other material points vanishes. This can be viewed as an extension of previous bond-severing criteria in state-based peridynamics to more general cases where the influence function is allowed to degrade gradually and to have a general dependence on other state variables such as plastic strain, void volume fraction, temperature, etc., thereby enabling the description of the damage evolution process. To assess the method, we consider the specific case of the Johnson-Cook plasticity and damage model [32].

7.1 Constitutive correspondence with damage

The ability to incorporate existing classical constitutive models provided by the correspondence formulation opens up the possibility of using classical continuum descriptions of damage within the peridynamic framework. However, it can be easily seen that an inattentive use of such models results in unphysical instabilities in numerical computations. Specifically, when a material particle in the peridynamic body is fully damaged, the material is able to flow unconstrained. Due to the nonlocal character of the peridynamic deformation gradient $\bar{\mathbf{F}}$, material points within the horizon of fully damaged regions will then compute unphysically-large strains which, in turn, will lead to unphysical damage. As a result, there is a tendency for damage to diffuse in an unrealistic manner in situations where damage should in fact localize into regions whose width should be of the order of the horizon size. It is therefore necessary to augment the peridynamic formulation to preserve the ability for damage to localize.

Instabilities in peridynamic simulations have been previously observed in the form of zero energy modes [21], which are common to many particle based continuum discretizations [90, 9]. These zero-energy modes can manifest themselves even in purely elastic simulations. However, the instability we focus on here appears to be primarily due to unphysical propagation of damage.

In order to address this issue, we adopt a generalized definition of the influence function ω, Equation (2.6), and make it dependent not only on the length of the bond $|\boldsymbol{\xi}|$, but also on the internal state-variables $(\mathbf{q}, \mathbf{q}')$:

$$\omega = \hat{\omega}(|\boldsymbol{\xi}|, \mathbf{q}, \mathbf{q}')$$

where $\mathbf{q}$ and $\mathbf{q}'$ are vectors of internal or state variables at the material points $\mathbf{x}$ and $\mathbf{x}'$ respectively. This strategy can be viewed as an extension of previous approaches to state-based peridynamic damage modeling in which the influence function is set to

zero when a bond failure criterion is satisfied [51, 78, 79] with two major differences: 1) the proposed formulation contemplates the possibility that the influence function may depend smoothly on the internal fields, resulting in a gradual degradation of material point interactions. In addition, 2) both the evolution of the damage process and the ultimate material failure criterion are governed by the classical continuum damage model which in general may depend on any of the internal state fields (e.g. plastic strain, void volume fraction, temperature, stress triaxiality, Lode angle, as well as material properties). These two considerations are probably critical to fully capture the damage mechanisms that are phenomenologically implied by the original continuum damage model.

In the following we will assume for simplicity that the state of material damage in the constitutive model is described by a single parameter D, which is commonly the case in some of the most popular damage models used in practice. We consider influence functions of the form

$$\hat{\omega}(|\boldsymbol{\xi}|, \mathbf{q}, \mathbf{q}') = \omega_\xi(|\boldsymbol{\xi}|)\, \omega_D(D, D') \tag{7.1}$$

where D and $D' \in [0, 1]$ are the values of the damage parameter at $\mathbf{x}$ and $\mathbf{x}'$, respectively, and $\omega_\xi(|\boldsymbol{\xi}|)$ is the conventional (radial) influence function which quantifies the relative degree of interaction between neighboring material points in an undamaged material. We require ω_D to be a non-increasing function of each of its arguments and to be zero if either argument is 1, i.e., $\omega_D(a, b) = 0$ if $a = 1$ or $b = 1$. In this way, the contribution of a damaged material point to the peridynamic force-state of neighboring points decreases as damage accumulates, and vanishes altogether when the material point is fully damaged. Any subsequent compressive response resulting from contact interactions are handled by a particle contact algorithm.

The specific forms we choose for the influence functions are

$$\omega_\xi(|\boldsymbol{\xi}|) = e^{-\frac{|\boldsymbol{\xi}|^2}{\sigma^2}},$$

$$\omega_D(D, D') = \begin{cases} 0 & \text{if } D > D_c, \text{ or } D' > D_c \\ 1 & \text{otherwise,} \end{cases} \tag{7.2}$$

where σ defines the physical length scale, and D_c is the critical bond damage. A Gaussian influence function such as ω_ξ has previously been used in the context of bond-based peridynamics [3]. The influence function, Equation (7.1), leads to equations of motion which conserve angular momentum, as can be shown by arguments identical to those presented in [98]. The only difference is the added explicit dependence on additional internal state-variables, $\mathbf{q}$ and $\mathbf{q}'$, which does not affect momentum conservation.

7.2 Constitutive model for metal

The damage correspondence formulation of Section 7.1 is general and can in principle be applied to a wide array of continuum damage models. For definiteness, we specialize it to a modified Johnson-Cook constitutive model of viscoplasticity and failure of metals [31, 32]. In this model, the flow stress Y is defined as

$$Y = \sigma_0 \left[1 + \frac{\epsilon^p}{\epsilon_0^p}\right]^n \left[1 + C \log\left(\frac{\dot{\epsilon}^p}{2\dot{\epsilon}_0^p} + \sqrt{1 + \left(\frac{\dot{\epsilon}^p}{2\dot{\epsilon}_0^p}\right)^2}\right)\right],$$

where ϵ^p is the equivalent plastic strain, $\dot{\epsilon}^p$ is the equivalent plastic strain rate,

$$\epsilon_0^p = \left(\frac{\sigma_0}{B}\right)^{\frac{1}{n}}$$

is a reference plastic strain, and $\dot{\epsilon}_0^p$ is a reference plastic strain rate. Compared to the classical Johnson-Cook flow stress, this modified expression avoids singularities in the hardening as $\dot{\epsilon}^p \to 0$ and in the hardening modulus as $\epsilon^p \to 0$. [31, 83, 76, 120]. The elastic part of the constitutive response is described using a hyperelastic formulation based on logarithmic strains and standard isotropic elastic constants.

As in the standard Johnson-Cook damage model [32], the evolution of damage is controled by the damage parameter given by

$$D = \int_0^t \dot{D}\, d\tau,$$

$$\dot{D} = \begin{cases} \frac{\dot{\epsilon}^p}{\epsilon_f} & \text{if } D < 1 \\ 0 & \text{otherwise} \end{cases}$$

with ϵ_f defined as

$$\epsilon_f = \left[d_1 + d_2 \exp\left(-d_3 \frac{\sigma_m}{\sigma_e}\right)\right]\left[1 + d_4 \ln\left(\frac{\dot{\epsilon}^p}{\dot{\epsilon}_0}\right)\right],$$

where d_1, d_2, d_3, d_4, and $\dot{\epsilon}_0$ are material parameters, σ_m is the hydrostatic stress, and σ_e is the Von Mises equivalent stress.

7.3 Ballistic impact simulations

To assess the functionality of the proposed state-based constitutive correspondence damage formulation, the discretized equations were implemented from scratch in a C++ computer code for three dimensional simulations. The discretization used for the example presented here is based on the particle method introduced in [52] and described in Section 3.1.

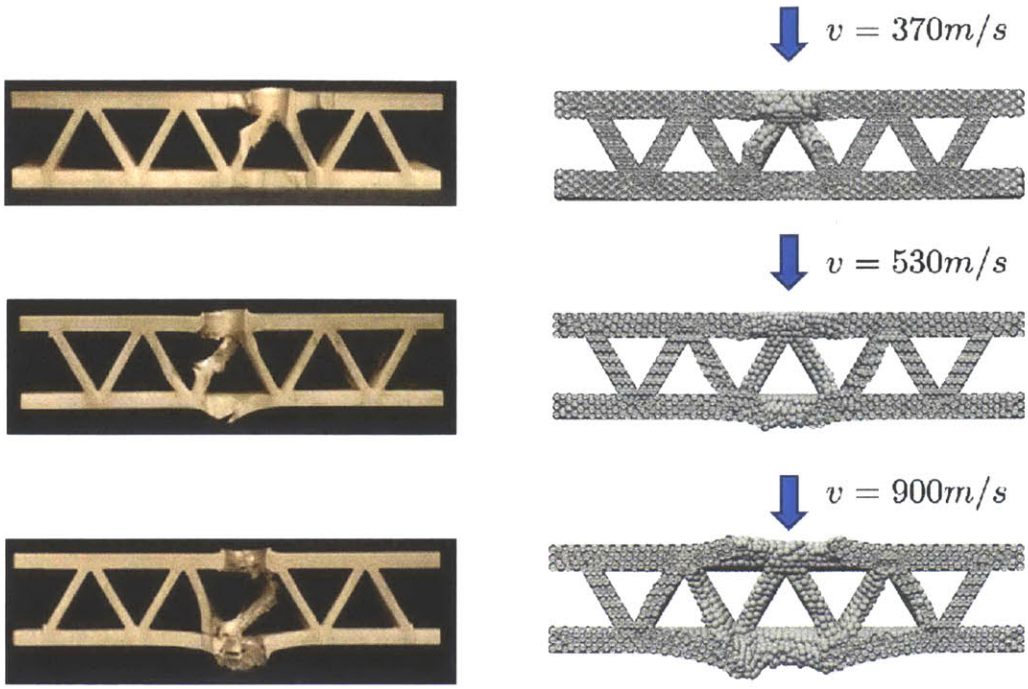

Figure 7-1: Comparison between numerical simulations and experimental results of a steel sphere projectile impacting an aluminum sandwich structure (experimental results courtesy of Hayden Wadley, UVA.)

We consider the simulation of recent experiments of hard-steel spherical projectiles of diameter 0.55 inches impacting extruded 6061-T6 aluminum sandwich panels [46]. The design of such sandwich structures for improved protection performance against impulsive loadings has recently received significant attention [61, 36, 110]. This case provides a stringent test on the ability of the numerical method to model damage, as material damage has a critical influence on the ballistic limit of the structure (the lowest projectile impact velocity for which the target is fully penetrated), and on the residual projectile velocities at higher impact speeds. The left column of Figure 7-1 shows the post-mortem configurations of the tested panels for different impact velocities.

In simulations, the panel's constitutive response was described by the modified Johnson Cook model, Section 7.2. The Young's modulus E and the strain hardening parameters n, B, and σ_0 were calibrated to quasi-static tensile tests, conducted on

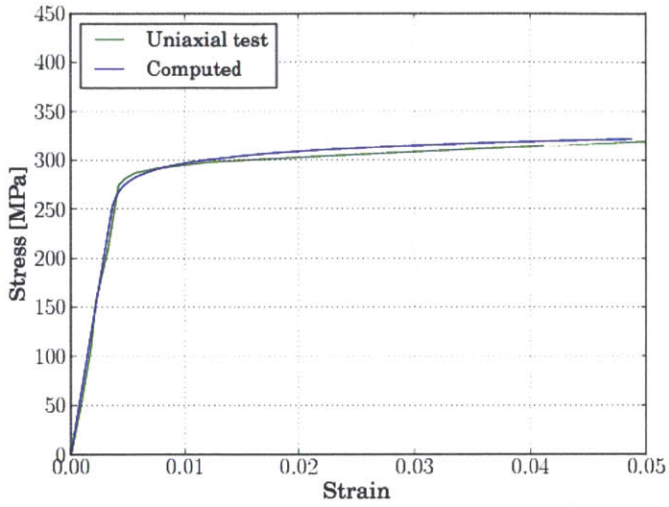

Figure 7-2: Modified Johnson-Cook material model fit against uniaxial test data [45].

coupons cut from the faces of the finished panels and measured in the direction of extrusion [45]. Figure 7-2 shows the quasi-static tensile test stress-strain curve obtained in experiments and the results from the calibrated constitutive model. The parameter C controlling rate-sensitivity in the flow stress was adopted from [18], where it was calibrated to dynamic test data for this material at a reference strain rate $\dot{\epsilon}^p = 1\,\mathrm{s}^{-1}$. The full set of calibrated constitutive parameter values for the viscoplastic response of the aluminum panels is shown in Table 7.1. A systematic approach to calibrate damage models for ductile fracture of metals typically involves conducting specific experiments of strain-to-failure for different triaxialities and possibly other parameters characterizing the local stress state [7, 54, 6]. However, it is well known that the damage parameters of the model must be recalibrated in simulations depending on the type and size of the discretization [17]. Considering these difficulties and that the emphasis of this chapter is in demonstrating the peridynamics description of damage, we calibrated the damage model using a simplified approach where the parameters were adjusted to match a specific measurable metric of a single experiment.

In simulations we represent failure between particles by breaking their bonds when

E	ν	σ_0	B	n	C	$\dot{\epsilon}_0^p$	ρ
72 GPa	0.343	250 MPa	365 MPa	0.04	0.002	1	2700 kg/m^3

Table 7.1: Material parameters used in ballistic impact simulations.

the damage parameter D_c in Equation (7.2) exceeds the value 0.99. The choice of a critical damage of 0.99 was chosen arbitrarily and its calibration may have a non-negligible impact on simulation results. Contact between particles is enforced using a simple penalty algorithm which prevents interpenetration of both undamaged and damaged particles. This form of contact is similar to what has been used in the peridynamic literature for particle-on-particle contact [67].

Since the spherical projectiles showed no perceivable plastic deformation in experiments, for simplicity we decided to model them as elastic with density 7800 kg/m^3, Young's modulus 200 GPa, and Poisson's ratio 0.25 using a finite element discretization. The boundary conditions for the plate were chosen so as to replicate the experimental conditions by fully constraining the particles along the two long sides of the sandwich specimen. Contact between the finite element mesh (projectile) and the peridynamic domain (sandwich structure) is enforced via penalty contact forces between the nodes of the finite element mesh and the particles in the peridynamic discretization. The peridynamic horizon radius was taken to be approximately three times the largest distance between neighboring particles, which proved to be sufficiently large to ensure reasonably stability of the method.

Simulations were conducted for all of the projectile impact velocities used in experiments. The simulations were run until the projectile: bounced, partially penetrated and was arrested by the panel, or fully penetrated and exited the back face with a final residual velocity. The Johnson-Cook damage parameters were calibrated using the test-case where the initial projectile velocity was 740 m/s. The parameters, shown in Table 7.2, were calibrated to exactly reproduce the experimentally observed residual

d_1	d_2	d_3	d_4
0.875	0.13	-1.5	0.0

Table 7.2: Damage parameters used in ballistic impact simulations.

velocity for this test-case. All other simulations were performed using those same parameters.

Figure 7-1 shows both the experimentally obtained [46] and simulated post-mortem deformed configuration of the impacted sandwich structures. The results show that the simulated results accurately predict that an initial projectile velocity of $v = 370$ m/s is well below the ballistic limit. For an initial velocity of $v = 530$ m/s, which is near the experimentally predicted ballistic limit, the simulated results accurately predict that the projectile penetrates the top face of the sandwich structure, but is barely stopped by the second layer. At $v = 900$ m/s, the prediction that the projectile penetrates both layers is again consistent with the experiments. The numerically computed projectile residual velocity as a function of the initial impact velocity is shown in Figure 7-3 and is compared with the corresponding experimental results by Wetzel [46]. As it can be observed in this figure, there is a very reasonable agreement between simulations and experiments.

7.4 Chapter summary

In this chapter, an extension of the peridynamic state-based constitutive correspondence framework to incorporate material damage has been proposed. The main motivation is the desire to incorporate in the modeling framework continuum damage models commonly used in other numerical approaches which have difficulty in simulating problems involving extreme deformations, e.g. the finite element method.

It is found that a direct use of damage models within the constitutive correspondence framework leads to instabilities associated with unphysical diffusion of the

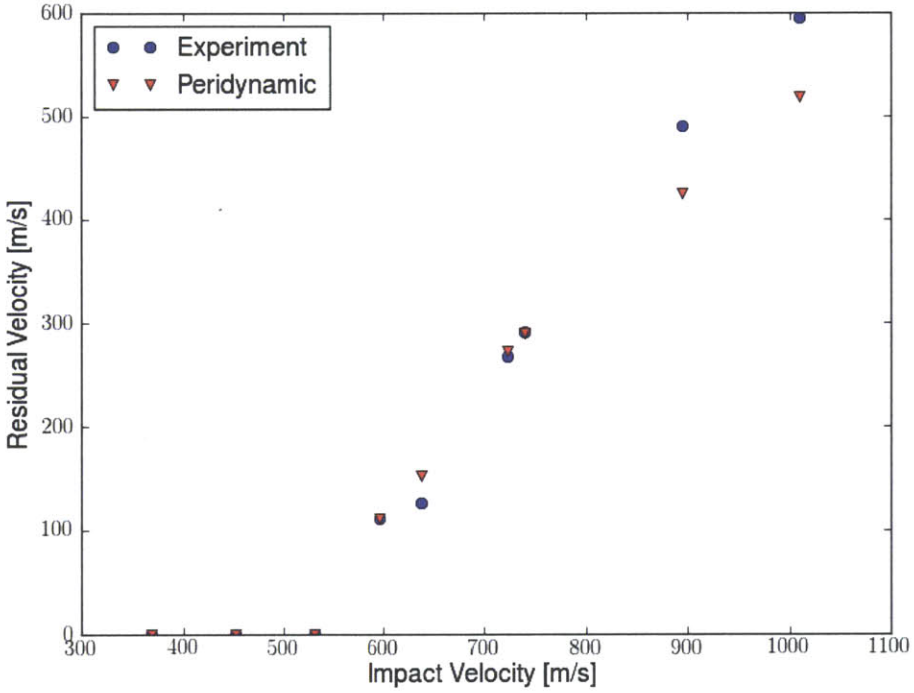

Figure 7-3: Simulated peridynamic residual velocity vs. initial impact velocity for sandwich panel impact compared to experimental results [46].

damage zone. In order to address this issue, we proposed to progressively degrade the peridynamic influence function appearing in the nonlocal integral measure of deformation as continuum damage accumulates. This approach effectively generalizes previous approaches which set the influence function to zero when a bond extension [78] or a bond elastic energy [51] criterion is satisfied. As a result, fully-damaged material points cease their interaction with their neighbors and damage diffusion issues are avoided.

The method was tested for the case of ballistic impact of steel spheres on corrugated aluminum sandwich structures at varying initial velocities. After calibrating the damage evolution law to a single experimental result, both the ballistic limit and the dependence of residual velocity on impact velocity were found to be in close agreement with experimental results. In conclusion, the proposed method furnishes a robust and simple way to incorporate damage models in the peridynamics framework method which is critical for problems involving severe deformations and failure.

Chapter 8

Summary and suggestions for future research

In this thesis, several extensions to the peridynamic theory of continua have been proposed. These developments emerged from limitations which were observed in particle simulations based on state-based peridynamics. The theoretical extensions generally fall into two categories: 1) reformulating the various peridynamic constitutive theories in terms of nonlinear (Seth-Hill) strain measures in order to prevent issues related to matter interpenetration, and 2) extending existing damage modeling approaches in peridynamics. A computational framework incorporating these extensions was developed and shown to overcome many of the previously observed limitations when simulating problems involving ballistic impact. A more detailed summary and suggestions for future work are presented below.

In the early part of the thesis process, numerical instabilities were observed when simulating ballistic impact events based on particle discretizations of the state-based theory of peridynamics. The identification of these instabilities and their ultimate solution (via modified peridynamic constitutive theories) provided motivation for a significant portion of the developments in this thesis. It was ultimately demonstrated

that these instabilities result from issues with the theory and are not artifacts of the discretization approach. To show this, a novel finite element discretization of state-based peridynamics was introduced in order to resolve the stability issues, which are typical for particle and meshless discretization of classical continuum mechanics. However, even after carefully addressing the numerical issues, the instabilities still persisted. This helped to confirm that the observed instabilities are due to theoretical issues within the original constitutive correspondence formulation.

Analytical investigation into the constitutive correspondence formulation of state-based peridynamics found that the theory permits the existence of unphysical deformation modes (i.e. matter interpenetration and zero-energy modes). In order to address this theoretical issue, an extension of the constitutive correspondence framework of peridynamics was proposed. The approach introduces generalized nonlocal peridynamic strain tensors which are in turn based on corresponding bond-level Seth-Hill strain measures. These bond-strain measures inherently avoid violations of the matter interpenetration constraint on a bond-by-bond basis. Analytical examples were used to show that the modified theory avoids issues of matter interpenetration in cases where the original theory fails. The introduced nonlinear bond-strain measures also enable a finite deformation extension of the linear version of the so-call ordinary elastic solids formulation. Once again, analytical and computational results are provided which highlight cases in which the nonlinear theory behaves reasonably while the linear theory fails to prevent matter interpenetration. Possible future work includes demonstrating how inelastic and anisotropic material behavior may be incorporated using the modified constitutive correspondence theory. Alternatively, inelasticity may be incorporated using the concept of the plastic part of the deviatoric extension-state (or in our case the plastic strain-state), as in [40]. Additional work is also needed to estimate the stable time-step for discretizations of nonlinear peridynamics formulations, as this currently constitutes a significant bottleneck in

numerical simulations.

In addition to resolving fundamental issues with the peridynamic theory and its discretization, two distinct approaches for modeling material damage were explored. The first approach is an extension of the *bond-severing* criteria used in bond-based peridynamic theories. It is formulated in terms of a critical energy per bond, corresponding to the energy dissipated when that bond is cut while all other bonds are held fixed. This is in contrast to existing critical bond-energy criterion which may not properly quantify the true energy dissipated by severing a bond. In addition, a generalized bond failure function is introduced which weighs the relative strength of bonds based on their initial separation distance. The resulting damage model has the property that the fracture energy G_c is treated as an input variable (similar to cohesive models of fracture). The viability of this approach in capturing experimentally observed fracture patterns was demonstrated using two standard test problems for brittle fracture: 1) edge on impact of PMMA and 2) the so-called Kalthoff test. For Mode-I fracture simulations based on the edge on impact tests, a fairly constant level of dissipated fracture energy was observed for different discretizations sizes, a rare feature for brittle fracture discretizations. In addition, it was shown that the input fracture energy G_c per unit crack length (in 2D) is dissipated in simulations to within a few percent error. A possible extension to this brittle fracture modeling approach is to combine such a bond-severing criterion with elasto-plastic bulk behavior, which would result in a ductile fracture law with a pre-specified cohesive energy. In addition, one could envision modifying the cohesive energy to make it depend on quantities such as stress triaxiality, Lode angle or crack-tip velocity. The proposed bond-severing approach can also be readily extended to constitutive correspondence theories of peridynamics.

In addition, an approach for incorporating classical continuum damage models in the state-based theory of peridynamics was proposed, which has the advantage of

enabling the description of the damage evolution process in peridynamics according to well-established models. The approach was applied to the simulation of ballistic impact of extruded corrugated aluminum panels and compared with experiments. This advancement has the advantage that practitioners desiring to use a peridynamics based discretization approach can readily use existing, well established models of material failure. An important next step for this line of research is apply the approach to more general damage models.

In summary, the extensions in this thesis have enabled the development of a powerful computational framework for simulating material response under extreme impact loading.

Appendix A

Appendix

A.1 Virtual power derivation of the peridynamic equations of motion

To derive the equations of motion for peridynamics, we deviate slightly from previous approaches which assume from the outset a momentum balance [98, 97], and instead we apply the principal of virtual power [65]. In this derivation, the key assumption of peridynamics is that internal work is performed by changes in the deformation vector-state at $\mathbf{x}$. In particular, the specific internal power is assumed to be given by the functional of the velocity field $\mathcal{P}_{\text{int}}(\cdot\,;\mathbf{x}) : \mathcal{B}_0 \to \mathbb{R}$,

$$\mathcal{P}_{\text{int}}(\mathbf{v}\,;\mathbf{x}) := \underline{\mathbf{T}} \bullet \underline{\dot{\mathbf{Y}}} = \int_{\mathcal{H}(\mathbf{x})} \underline{\mathbf{T}}\,\langle \boldsymbol{\xi} \rangle \cdot (\mathbf{v}(\mathbf{x}+\boldsymbol{\xi}) - \mathbf{v}(\mathbf{x}))\; d\boldsymbol{\xi},$$

where the force vector-state $\underline{\mathbf{T}}$ is defined to be the vector-state which is power conjugate to the deformation vector-state, $\mathbf{v}(\mathbf{x}) := \dot{\boldsymbol{\varphi}}(\mathbf{x})$ is the velocity field, and $\mathbf{x}$ parametrizes the location where the specific power is evaluated. This form for the internal power is analougous to the stress power $\mathcal{P}_{\text{s}} = \mathbf{P} : \dot{\mathbf{F}}$ in classical continuum theories, where $\mathbf{F}$ is the deformation gradient tensor and $\mathbf{P}$ is the first Piola-Kirchhoff

stress tensor.

The total internal power $\mathcal{I}$ over $\mathcal{B}_0$ is

$$\mathcal{I} = \int_{\mathcal{B}_0} \mathcal{P}_{\text{int}}(\mathbf{v}\,;\mathbf{x})\; d\mathbf{x},$$

and the externally applied power $\mathcal{W}$ is assumed to be of the form

$$\mathcal{W} = \int_{\mathcal{B}_0} \mathbf{b}(\mathbf{x}) \cdot \mathbf{v}(\mathbf{x})\; d\mathbf{x},$$

where $\mathbf{b}$ is the externally applied body force which is power conjugate to $\mathbf{v}$. We make the standard assumption that the kinetic energy $\mathcal{K}$ of the body is given by

$$\mathcal{K} = \int_{\mathcal{B}_0} \frac{1}{2}\rho(x)|\mathbf{v}(\mathbf{x})|^2\; d\mathbf{x},$$

and the rate of change of the total kinetic energy is

$$\dot{\mathcal{K}} = \int_{\mathcal{B}_0} \rho(\mathbf{x})\, \dot{\mathbf{v}}(\mathbf{x}) \cdot \mathbf{v}(\mathbf{x})\; d\mathbf{x},$$

where $\rho(x)$ is the spatially varying reference density, which is constant in time. Conservation of energy implies the power balance:

$$\mathcal{W} = \mathcal{I} + \dot{\mathcal{K}}, \tag{A.1}$$

which must hold over the body $\mathcal{B}_0$.

The principal of virtual power [65] requires that equation (A.1) must hold for all admissible "virtual velocities" $\bar{\mathbf{v}}$, which are disassociated from the actual evolution of

the body:

$$\int_{\mathcal{B}_0} \mathbf{b}(\mathbf{x}) \cdot \bar{\mathbf{v}}(\mathbf{x})\, d\mathbf{x} = \int_{\mathcal{B}_0} \mathcal{P}_{\text{int}}(\bar{\mathbf{v}}\,;\mathbf{x})\, d\mathbf{x} + \int_{\mathcal{B}_0} \rho(\mathbf{x})\, \dot{\mathbf{v}}(\mathbf{x}) \cdot \bar{\mathbf{v}}(\mathbf{x})\, d\mathbf{x}, \quad \forall \bar{\mathbf{v}} \in \mathcal{B}_0 \times \mathbb{R}^3. \tag{A.2}$$

By changing variables and the order of integration:

$$\begin{aligned}
\int_{\mathcal{B}_0} \mathcal{P}_{\text{int}}(\bar{\mathbf{v}}\,;\mathbf{x})\, d\mathbf{x} &= \int_{\mathcal{B}_0} \int_{\mathcal{H}(\mathbf{x})} \underline{\mathbf{T}}\,[\mathbf{x}]\, \langle \boldsymbol{\xi} \rangle \cdot [\bar{\mathbf{v}}(\mathbf{x}+\boldsymbol{\xi}) - \bar{\mathbf{v}}(\mathbf{x})]\, d\boldsymbol{\xi}\, d\mathbf{x} \\
&= \int_{\mathcal{B}_0} \int_{\mathcal{B}_0} \underline{\mathbf{T}}\,[\mathbf{x}]\, \langle \mathbf{x}' - \mathbf{x} \rangle \cdot [\bar{\mathbf{v}}(\mathbf{x}') - \bar{\mathbf{v}}(\mathbf{x})]\, d\mathbf{x}'\, d\mathbf{x} \\
&= \int_{\mathcal{B}_0} \int_{\mathcal{B}_0} \underline{\mathbf{T}}\,[\mathbf{x}']\, \langle \mathbf{x} - \mathbf{x}' \rangle \cdot \bar{\mathbf{v}}(\mathbf{x})\, d\mathbf{x}\, d\mathbf{x}' \\
&\quad - \int_{\mathcal{B}_0} \int_{\mathcal{B}_0} \underline{\mathbf{T}}\,[\mathbf{x}]\, \langle \mathbf{x}' - \mathbf{x} \rangle \cdot \bar{\mathbf{v}}(\mathbf{x})\, d\mathbf{x}'\, d\mathbf{x} \\
&= \int_{\mathcal{B}_0} \left(\int_{\mathcal{B}_0} \underline{\mathbf{T}}\,[\mathbf{x}']\, \langle \mathbf{x} - \mathbf{x}' \rangle - \underline{\mathbf{T}}\,[\mathbf{x}]\, \langle \mathbf{x}' - \mathbf{x} \rangle\, d\mathbf{x}' \right) \cdot \bar{\mathbf{v}}(\mathbf{x})\, d\mathbf{x},
\end{aligned}$$

and the balance (A.2) becomes

$$\int_{\mathcal{B}_0} \left(\mathbf{b} - \int_{\mathcal{H}(\mathbf{x})} \underline{\mathbf{T}}'\langle -\boldsymbol{\xi} \rangle - \underline{\mathbf{T}}\,\langle \boldsymbol{\xi} \rangle\, d\boldsymbol{\xi} - \rho \dot{\mathbf{v}} \right) \cdot \bar{\mathbf{v}}(\mathbf{x})\, d\mathbf{x} = 0, \quad \forall \bar{\mathbf{v}},$$

where $\underline{\mathbf{T}} = \underline{\mathbf{T}}\,[\mathbf{x}]$, and $\underline{\mathbf{T}}' = \underline{\mathbf{T}}\,[\mathbf{x}']$. Invoking the fundamental lemma of the calculus of variation, the local force balance

$$\rho \ddot{\boldsymbol{\varphi}} = \int_{\mathcal{H}(\mathbf{x})} \underline{\mathbf{T}}\,\langle \boldsymbol{\xi} \rangle - \underline{\mathbf{T}}'\langle -\boldsymbol{\xi} \rangle\, d\boldsymbol{\xi} + \mathbf{b} \tag{A.3}$$

must be satisfied. Equation (A.3) is the standard peridynamic equation of motion [98, 97].

In addition, the requirement of frame invariance of the specific internal power

provides restrictions on the force state $\underline{\mathbf{T}}$. Consider a change of frame

$$\mathbf{y}^* = \mathbf{u} + \mathbf{Q}\,\mathbf{y}, \quad \dot{\mathbf{y}}^* = \dot{\mathbf{u}} + \dot{\mathbf{Q}}\,\mathbf{y} + \mathbf{Q}\,\dot{\mathbf{y}}.$$

$\mathbf{u} \in \mathbb{R}^3$, and where $\mathbf{Q} \in \mathbb{R}^3 \times \mathbb{R}^3$ is a rotation vector, $\mathbf{Q}\mathbf{Q}^T = \mathbf{Q}^T\mathbf{Q} = \mathbf{1}$, where without loss of generalization we assume that the rotation is about the origin $\mathbf{0}$. The specific internal power in the new frame must equal the internal power in the original frame:

$$\mathcal{P}_{\text{int}} = \underline{\mathbf{T}} \bullet \underline{\dot{\mathbf{Y}}} = \underline{\mathbf{T}}^* \bullet \underline{\dot{\mathbf{Y}}}^*.$$

Evaluating the right hand side:

$$\begin{aligned}
\underline{\mathbf{T}}^* \bullet \underline{\dot{\mathbf{Y}}}^* &= \int_{\mathcal{H}(\mathbf{x})} \mathbf{Q}\,\underline{\mathbf{T}}\langle\boldsymbol{\xi}\rangle \cdot \left[\dot{\mathbf{Q}}\,(\mathbf{y}(\mathbf{x}+\boldsymbol{\xi}) - \mathbf{y}(\mathbf{x})) + \mathbf{Q}\,(\dot{\mathbf{y}}(\mathbf{x}+\boldsymbol{\xi}) - \dot{\mathbf{y}}(\mathbf{x}))\right] d\boldsymbol{\xi} \\
&= \int_{\mathcal{H}(\mathbf{x})} \underline{\mathbf{T}}\langle\boldsymbol{\xi}\rangle \cdot \mathbf{Q}^T \left[\dot{\mathbf{Q}}\,(\mathbf{y}(\mathbf{x}+\boldsymbol{\xi}) - \mathbf{y}(\mathbf{x})) + \mathbf{Q}\,(\dot{\mathbf{y}}(\mathbf{x}+\boldsymbol{\xi}) - \dot{\mathbf{y}}(\mathbf{x}))\right] d\boldsymbol{\xi} \\
&= \int_{\mathcal{H}(\mathbf{x})} \underline{\mathbf{T}}\langle\boldsymbol{\xi}\rangle \cdot (\dot{\mathbf{y}}(\mathbf{x}+\boldsymbol{\xi}) - \dot{\mathbf{y}}(\mathbf{x}))\, d\boldsymbol{\xi} + \int_{\mathcal{H}(\mathbf{x})} \underline{\mathbf{T}}\langle\boldsymbol{\xi}\rangle \cdot \mathbf{Q}^T\dot{\mathbf{Q}}\,(\mathbf{y}(\mathbf{x}+\boldsymbol{\xi}) - \mathbf{y}(\mathbf{x}))\, d\boldsymbol{\xi} \\
&= \underline{\mathbf{T}} \bullet \underline{\dot{\mathbf{Y}}} + \int_{\mathcal{H}(\mathbf{x})} \underline{\mathbf{T}}\langle\boldsymbol{\xi}\rangle \cdot [\boldsymbol{\omega} \times (\mathbf{y}(\mathbf{x}+\boldsymbol{\xi}) - \mathbf{y}(\mathbf{x}))]\, d\boldsymbol{\xi} \\
&= \underline{\mathbf{T}} \bullet \underline{\dot{\mathbf{Y}}} + \left(\int_{\mathcal{H}(\mathbf{x})} \underline{\mathbf{T}}\langle\boldsymbol{\xi}\rangle \times (\mathbf{y}(\mathbf{x}+\boldsymbol{\xi}) - \mathbf{y}(\mathbf{x}))\, d\boldsymbol{\xi}\right) \cdot \boldsymbol{\omega},
\end{aligned}$$

where $\boldsymbol{\omega}$ is the angular velocity vector of the rotating frame associated with the skew tensor $\mathbf{Q}^T\dot{\mathbf{Q}}$. Enforcing that the expended power is invariant to arbitrary frame rotations requires[1]

$$\left(\int_{\mathcal{H}(\mathbf{x})} \underline{\mathbf{T}}\langle\boldsymbol{\xi}\rangle \times (\mathbf{y}(\mathbf{x}+\boldsymbol{\xi}) - \mathbf{y}(\mathbf{x}))\, d\boldsymbol{\xi}\right) \cdot \boldsymbol{\omega} = 0, \quad \forall \boldsymbol{\omega} \in \mathbb{R}^3$$

[1]Note that translation invariance is automatically satisfied because only relative deformations are accounted for in the deformation vector-state.

and therefore

$$\int_{\mathcal{H}(\mathbf{x})} \underline{\mathbf{T}}\langle\boldsymbol{\xi}\rangle \times \underline{\mathbf{Y}}\langle\boldsymbol{\xi}\rangle \, d\boldsymbol{\xi} = \mathbf{0}, \quad \forall \mathbf{x} \in \mathcal{B}_0. \tag{A.4}$$

It known that the peridynamic equation of motion (A.3), together with equation (A.4) ensures conservation of linear and angular momentum over the peridynamic body $\mathcal{B}_0$ [98, 97]. In the peridynamic literature, materials which satisfy (A.4) are called nonpolar, and it appears to be a new result that this condition (the nonpolar constraint) can be derived directly from frame invariance principals. For a more general discussion of non-local conservation laws on subregions $\mathcal{P} \subset \mathcal{B}_0$, see [97].

Having investigated the consequences of the first law of thermodynamics together with frame invariance of power expenditures, in the next section we investigate constitutive restrictions required to satisfy the second law of thermodynamics. This derivation is similar to that in [97], and is included for completeness.

A.2 Thermodynamic restrictions on the constitutive behavior

We postulate the existence of a Helmholtz free energy ψ, which depends on the deformation vector-state, internal vector-states, and other internal variables and is allowed to vary in space:

$$\psi = \hat{\psi}(\underline{\mathbf{Y}}, \underline{\mathbf{q}}, \mathbf{q}, \theta; \mathbf{x}), \tag{A.5}$$

where $\underline{\mathbf{q}}$ are internal vector-state field variables (e.g. a damage-state [97]), $\mathbf{q}$ are internal field variables, and θ is temperature. The second law of thermodynamics can

be expressed via a dissipation version of the Clausius-Duhem inequality [97, 65]:

$$\underline{\mathbf{T}} \bullet \underline{\dot{\mathbf{Y}}} - \dot{\theta}\,\eta - \dot{\psi} \geq 0, \tag{A.6}$$

where η is the entropy,

$$\dot{\psi} = \psi_{,\underline{\mathbf{Y}}} \bullet \underline{\dot{\mathbf{Y}}} + \psi_{,\underline{\mathbf{q}}} \bullet \underline{\dot{\mathbf{q}}} + \nabla_{\mathbf{q}}\psi \cdot \dot{\mathbf{q}} + \frac{\partial \psi}{\partial \theta}\,\dot{\theta},$$

and recalling that $\underline{\mathbf{T}} \bullet \underline{\dot{\mathbf{Y}}}$ is the specific internal power. We can decompose the force-state as

$$\underline{\mathbf{T}} = \underline{\hat{\mathbf{T}}}\left(\underline{\mathbf{Y}}, \underline{\dot{\mathbf{Y}}}, \underline{\mathbf{q}}, \mathbf{q}, \theta\right) = \underline{\hat{\mathbf{T}}}_e\left(\underline{\mathbf{Y}}, \underline{\mathbf{q}}, \mathbf{q}, \theta\right) + \underline{\hat{\mathbf{T}}}_d\left(\underline{\mathbf{Y}}, \underline{\dot{\mathbf{Y}}}, \underline{\mathbf{q}}, \mathbf{q}, \theta\right),$$

where the subscripts e and d mean equilibrium and dissipative respectively, using (A.6)

$$\left[\underline{\hat{\mathbf{T}}}_e - \psi_{,\underline{\mathbf{Y}}}\right] \bullet \underline{\dot{\mathbf{Y}}} + \underline{\hat{\mathbf{T}}}_d \bullet \underline{\dot{\mathbf{Y}}} - \psi_{,\underline{\mathbf{q}}} \bullet \underline{\dot{\mathbf{q}}} - \nabla_{\mathbf{q}}\psi \cdot \dot{\mathbf{q}} - \left[\eta + \frac{\partial \psi}{\partial \theta}\right] \dot{\theta} \geq 0.$$

Allowing $\underline{\dot{\mathbf{Y}}}$, and $\dot{\theta}$ to vary arbitrarily:

$$\underline{\hat{\mathbf{T}}}_e = \psi_{,\underline{\mathbf{Y}}} \text{ and } \eta = -\frac{\partial \psi}{\partial \theta}.$$

Furthermore, we require each inequality term to hold independently:

$$\underline{\hat{\mathbf{T}}}_d \bullet \underline{\dot{\mathbf{Y}}} \geq 0,$$

$$-\psi_{,\underline{\mathbf{q}}} \bullet \underline{\dot{\mathbf{q}}} \geq 0,$$

$$-\nabla_{\mathbf{q}}\psi \cdot \dot{\mathbf{q}} \geq 0.$$

Elastic peridynamic materials are defined by the restricted dependence

$$\psi = \hat{\psi}(\underline{\mathbf{Y}}, \theta),$$

$$\underline{\mathbf{T}}_d \langle \boldsymbol{\xi} \rangle = \mathbf{0}, \quad \forall \boldsymbol{\xi} \in \mathcal{H}(\mathbf{x}).$$

Bibliography

[1] A. Kamoulakos. A simple benchmark for impact. *Benchmark*, pages 31–35, 1990.

[2] A.C. Eringen. Linear theory of nonlocal elasticity and dispersion of plane waves. *International Journal of Engineering Science*, 10:425–435, 1972.

[3] B. Kilic and E. Madenci. Prediction of crack paths in a quenched glass plate using peridynamic theory. *International Journal of Fracture*, 156:165–177, 2009.

[4] B. Li, F. Habbal, and M. Ortiz. Optimal transportation meshfree approximation schemes for fluid and plastic flows. *International Journal for Numerical Methods in Engineering*, 83:1541–1579, 2010.

[5] B. Nayroles, G. Touzot, and P. Villon. Generalizing the finite element method: diffuse approximation and diffuse elements. *Computational Mechanics.*, 10:307–318, 1992.

[6] Y. Bai and T. Wierzbicki. Application of extended Mohr–Coulomb criterion to ductile fracture. *International Journal of Fracture*, 161:1–20, 2010.

[7] Y. Bao and T. Wierzbicki. A comparative study on various ductile crack formation criteria. *Journal of Engineering Materials and Technology*, 126:314–324, 2004.

[8] S.R. Beissel, C.A. Gerlach, T.J. Holmquist, and J.D. Walker. Comparison of numerical methods in the simulation of hypervelocity pact. *Proceedings of 11th Hypervelocity Impact Symposium, Freiburg, Germany*, 2010.

[9] T. Belytschko, Y. Guox, W.K. Liu, and S.P. Xia. A unifed stability analysis of meshless particle methods. *International Journal for Numerical Methods in Engineering*, 48:1359–1400, 2000.

[10] G.C. Bessette, E.B. Becker, L.M. Taylor, and D.L. Littlefield. Modeling of impact problems using an h-adaptive, explicit lagrangian finite element method in three dimensions. *Computer Methods in Applied Mechanics and Engineering*, 192:1649–1679, 2003.

[11] W. Bohme and J. Kalthoff. The behavior of notched bend specimens in impact testing. *International Journal of Fracture*, 20:139–143, 1982.

[12] T. Borvik, O.S. Hopperstad, and K.O. Pedersen. Quasi-brittle fracture during structural impact of aa7075-t651 aluminium plates. *International Journal of Impact Engineering*, 37:537–551, 2010.

[13] B.R. Seth. Generalized strain measures with applications to physical problems. In M. Rener and D. Abir, editors, *Second-order effects in elasticity, plasticity and fluid dynamics.* Oxford, 1964.

[14] C.A.M. Duarte and J.T. Oden. H-p clouds an h-p meshless method. *Numerical Methods for Partial Differential Equations*, 12:673–705, 1996.

[15] G.T. Camacho and M. Ortiz. Computational modeling of impact damage in brittle materials. *International Journal of Solids and Structures*, 33(20–22):2899–2983, 1996.

[16] C.E. Zhou, G.R. Liu, and X. Han. Classic taylor-bar impact test revisited using 3D SPH. *G.R. Liu et al. (eds.), Computational Methods*, pages 1405–1409, 2010.

[17] Committee on Opportunities in Protection Materials Science and Technology for Future Army Applications; National Research Council. *Opportunities in Protection Materials Science and Technology for Future Army Applications.* National Academies Press, 2011. pdf, online link.

[18] K.A. Dannemann, C.E. Anderson, and G.R. Johnson. Modeling the ballistic impact performance of two aluminum alloys. In D.R. Lesuer and T.S. Srivatsan, editors, *Proceedings of the symposium modeling the performance of engineering structural materials II*, pages 63–74, Indianapolis, Indiana, USA, Nov 4-8 2001. The Minerals, Metals and Materials Society (TMS). pdf.

[19] V.S. Deshpande and A.G. Evans. Inelastic deformation and energy dissipation in ceramics: a mechanism-based constitutive model. *Journal of the Mechanics and Physics of Solids*, 56:3077–3100, 2008.

[20] D.J. Benson. Computational methods in lagrangian and eulerian hydrocodes. *Computer Methods in Applied Mechanics and Engineering*, 99:235–394, 1992.

[21] D.L. Littlewood. Simulation of dynamic fracture using peridynamics, finite element modeling, and contact. *Proceedings of the ASME 2010 International Mechanical Engineering Congress & Exposition*, November 12-18, 2010.

[22] E. Askari, F. Bobaru, R.B. Lehoucq, M.L. Parks, S.A. Silling, and O. Weckner. Peridynamics for multiscale materials modeling. *Journal of Physics: Conference Series*, 125:012078, 2008.

[23] E. Emmrich and O. Wechner. Analysis and Numerical Approximation of an Integro-differential Equation Modeling Non-local Effects in Linear Elasticity. *Mathematics and Mechanics of Solids*, 12:363–384, 2007.

[24] E. Emmrich and O. Wechner. The peridynamic equation and its spatial discretization. *Math. Model. Anal.*, 12:17–27, 2007.

[25] E. Emmrich and O. Weckner. On the well-posedness of the linear peridynamic model and its convergence towards the Navier equation of linear elasticity. *Communications in Mathematical Sciences*, 5:851–864, 2007.

[26] E.P. Fahrenthold and B.A. Horban. A hybrid particle-finite element method for hypervelocity impact simulation. *International Journal of Impact Engineering*, 23:237–248, 1999.

[27] E.P. Fahrenthold and R. Shivarama. Orbital debris impact simulation using a parallel hybrid particle-element code. *International Journal of Impact Engineering*, 26:179–188, 2001.

[28] F. Bobaru and M. Duangpanya. The peridynamic formulation for transient heat conduction. *International Journal of Heat and Mass Transfer*, published online June 4, 2010.

[29] F. Bobaru and W. Hu. The meaning, selection, and use of the peridynamic horizon and its relation to crack branching in brittle materials. *International Journal of Fracture*, 176:215–222, 2012.

[30] G.I. Taylor. The use of flat-ended projectiles for determining dynamic yield stress i. theoretical considerations. *Proceedings of the Royal Society of London. Series A. Mathematical and Physical Sciences*, 194:289–299, 1948.

[31] G.R. Johnson and W.H. Cook. A constitutive model and data for metals subjected to large strains, high strain rates and high temperatures. In *Proceedings of the 7th International Symposium on Ballistics*, pages 541–547, The Hague, Netherlands, 1983. pdf.

[32] G.R. Johnson and W.H. Cook. Fracture characteristics of three metals subjected to various strains, strain rates, temperatures and pressures. *Engineering Fracture Mechanics*, 21:31–48, 1985.

[33] G.R. Johnson, R.A. Stryk, and S.R. Beissel. SPH for high velocity impact computations. *Computer Methods in Applied Mechanics and Engineering*, 139:347–373, 1996.

[34] A.A. Griffith. The phenomena of rupture and flow in solids. In Royal society (GB)., editor, *Philosophical transactions of the Royal society of London*, volume Series A221, Mathematical and physical sciences, pages 163–198. Cambridge University Press, 1920. no pdf, no DOI.

[35] G.T. Camacho and M. Ortiz. Adaptive lagrangian modelling of ballistic penetration of metallic targets. *Computer Methods in Applied Mechanics and Engineering*, 142:269–301, 1997.

[36] H.N.G. Wadley. Multifunctional periodic cellular metals. *Philisophical Transactions of the Royal Society A*, 364:31–68, 2006.

[37] G.A. Holzapfel. *Nonlinear Solid Mechanics: A Continuum Approach for Engineering.* John Wiley & Sons Ltd., 2001.

[38] J. Bonet, S. Kulasegaram, M.X. Rodriguez-Paz, and M. Profit. Variational formulation for the smooth particle hydrodynamics (sph) simulation of fluid and solid problems. *Computer Methods in Applied Mechanics and Engineering*, 193:1245–1256, 2004.

[39] J. Foster, S.A. Silling, and W. Chen. An energy based failure criterion for use with peridynamic states. *International Journal for Multiscale Computational Engineering*, 9:675–688, 2011.

[40] J.A. Mitchell. A nonlocal, ordinary, state-based plasticity model for peridynamcis. *Sandia Report, 2011*, 2011.

[41] J.B. Aidun and S.A. Silling. Accurate prediction of dynamic fracture with peridynamics. Joint US-Russian Conference on Advances in Material Science, Prague, 2009.

[42] J.C. Simo. Algorithms for static dynamic multiplicative plasticity that preserve the classical return mapping schemes of the infinitesimal theory. *Computer Methods in Applied Mechanics and Engineering*, 99:61–112, 1992.

[43] J.J. Monaghan. An introduction to SPH. *Computer Physics Communications*, 48:89–96, 1988.

[44] J.J. Monaghan. Smoothed particle hydrodynamics. *Reports on Progress in Physics*, 68:1703–1759, 2005.

[45] J.J. Rimoli, B. Talamini, J.J. Wetzel, K.P. Dharmasena, R. Radovitzky and H.N.G. Wadley. Wet-sand impulse loading of metallic plates and corrugated core sandwich panels. *International Journal of Impact Engineering*, 38:837–848, 2011.

[46] J.J. Wetzel. The impulse response of extruded corrugated core aluminum sandwich structures. Master's thesis, University of Virginia, 2009.

[47] J.M. Ball. Convexity conditions and existence theorems in nonlinear elasticity. *Arch. Rat. Mech. Anal.*, 63:337–403, 1977.

[48] J.M. Melenk and I. Babuska. The partition of unity finite element method: basic theory and applications. *Computer Methods in Applied Mechanical Engineering*, 139:280–314, 1996.

[49] G. R. Johnson and T. J. Holmquist. Evaluation of cylinder-impact test data for constitutive models. *Journal of Applied Physics*, 64(8):3901–3910, 1988.

[50] G.R. Johnson and R.A. Stryk. Conversion of 3D distorted elements into meshless particles during dynamic deformation. *International Journal of Impact Engineering*, 28(9):947 – 966, 2003.

[51] J.T. Foster. Dynamic Crack Initiation Toughness: Experiments and Peridynamic Modeling. *Technical Report SAND2009-7217, Sandia National Laboratories, Albuquerque*, 2009.

[52] J.T. Foster, S.A. Silling, and W.W. Chen. Viscoplasticity using peridynamics. *International Journal for Numerical Methods in Engineering*, 81:1242–1258, 2010.

[53] K. Dayal and K. Bhattacharya. Kinetics of phase transformations in the peridynamic formulation of Continuum Mechanics. *Journal of the Mechanics and Physics of Solids*, 54:1811–1842, 2006.

[54] K. Nahshon and J.W. Hutchinson. Modification of the Gurson model for shear failure. *European Journal of Mechanics A/Solids*, 27:1–17, 2008.

[55] J. Kalthoff. On the measurement of dynamic fracture toughnesses - a review of recent work. *International Journal of Fracture*, 27:277–298, 1985.

[56] J.F. Kalthoff and S. Winkler. Failure mode transition at high rates of shear loading. In C.Y. Chiem, H.D. Kunze and L.W. Meyer, editor, *International Conference on Impact Loading and Dynamic Behavior of Materials*, pages 185–195, 1987.

[57] L. Xue. *Ductile Fracture Modeling - Theory, Experimental Investigation and Numerical Verification.* PhD thesis, Massachusetts Institute of Technology, 2007.

[58] S.K. Lahiri, J. Bonet, and J. Peraire. A variationally consistent mesh adaptation method for explicit lagrangian dynamics. *International Journal for Numerical Methods in Engineering*, pages 1–38, 2007.

[59] J. Lambros and A.J. Rosakis. Dynamic decohesion and bimaterials: Experimental observations and failure criteria. *International Journal of Solids and Structures*, 32:17, 1995.

[60] L.B. Lucy. A numerical approach to the testing of the fission hypothesis. *The Astronomical Journal*, 82:1013–1024, 1977.

[61] L.F. Mori, S. Lee, Z.Y. Xue, A. Vaziri, D.T. Queheillalt, K.P. Dharmasena, H.N.G. Wadley, J.W. Hutchinson and H.D. Espinosa. Deformation and fracture modes of sandwich structures subjected to underwater impulsive loads. *Journal of Mechanics of Materials and Structures*, 2:1981–2006, 2007.

[62] Z. L. Liu, T. Menouillard, and T. Belytschko. An xfem/spectral element method for dynamic crack propagation. *International Journal of Fracture*, 169:183–198, 2011.

[63] M. Arroyo and M. Ortiz. Local maximum-entropy approximation schemes: a seamless bridge between finite elements and meshfree methods. *International Journal for Numerical Methods in Engineering*, 65:2167–2202, 2006.

[64] M. Zimmermann. *A continuum theory with long-range forces for solids.* PhD thesis, Massachusetts Institute of Technology, 2005.

[65] M.E. Gurtin, E. Fried, and L. Anand. *The Mechanics and Thermodynamics of Continua.* Cambridge University Press, 2010.

[66] M.L. Parks, D.J. Littlewood, J.A. Mitchell, and S.A. Silling. Peridigm users guide v1.0.0. *Sandia Report, 2012-7800*, 2012.

[67] M.L. Parks, R.B. Lehoucq, S. Plimpton, and S. Silling. Implementing peridynamics within a molecular dynamics code. *Computer Physics Communications*, 179:777–783, 2008.

[68] M.R. Tupek. Lagrangian methods for ballistic impact simulations. Master's thesis, Massachusetts Institute of Technology, 2010.

[69] M.R. Tupek, J.J. Rimoli, R. Radovitzky. An approach for incorporating classical continuum damage models in state-based peridynamics. *Computer Methods in Applied Mechanics and Engineering*, 263:20–26, 2013.

[70] M.R. Tupek, R. Radovitzky. An extended constitutive correspondence formulation of peridynamics based on nonlinear bond-strain measures. *Submitted to JMPS*, 0:0–0, 2013.

[71] L. Noels and R. Radovitzky. A general discontinuous Galerkin method for finite hyperelasticity. Formulation and numerical applications. *International Journal for Numerical Methods in Engineering*, 68(1):64–97, 2006.

[72] L. Noels and R. Radovitzky. An explicit discontinuous Galerkin method for non-linear solid dynamics. Formulation, parallel implementation and scalability properties. *International Journal for Numerical Methods in Engineering*, 74(9):1393–1420, 2007.

[73] O. Weckner and R. Abeyaratne. The effect of long-range forces on the dynamics of a bar. *Journal of the Mechanics and Physics of Solids*, 53:705–728, 2005.

[74] O. Weckner, G. Brunk, M.A. Epton, S.A. Silling, and E. Askari. Green's functions in non-local three-dimensional linear elasticity. *Proceedings of the Royal Society A*, 465:3463–3487, 2009.

[75] R.W. Ogden. *Non-linear elastic deformations.* Dover, New York, 1997.

[76] M. Ortiz and L. Stainier. The variational formulation of viscoplastic updates. *Computer Methods in Applied Mechanics and Engineering*, 171:419–444, 1999.

[77] P. DiMarco. Navy foreign object damage and its impact on future gas turbine engine low pressure compression systems. *Propulsion and Energetics Panel Symposium: Erosion, Corrosion and Foreign Object Damage Effects in Gas Turbines*, 1994.

[78] P. Seleson. *Peridynamic multiscale models for the mechanics of materials: constitutive relations, upscaling from atomistic systems, and interface problems.* PhD thesis, Florida State University, 2010.

[79] P. Seleson and M.L. Parks. On the role of the influence function in the peridynamic theory. *Journal for Multiscale Computational Engineering*, 9(6):689–706, 2011.

[80] S.J. Plimpton. Fast parallel algorithms for short-range molecular dynamics. *Journal of Computational Physics*, 117:1–19, 1995.

[81] R. Becker and R. Lucas. An assessment of peridynamics for pre and post failure deformation. Technical Report ARL-TR-5811, U.S. Army Research Laboratory, Aberdeen Proving Ground, MD 21005, November 2011.

[82] R. Hill. On constitutive inequalities for simple materials. *I.J. Mech. Phys. Solids*, 16:229–242, 1968.

[83] R. Radovitzky and M. Ortiz. Error estimation and adaptive meshing in strongly nonlinear dynamic problems. *Computer Methods in Applied Mechanics and Engineering*, 172:203–240, 1999.

[84] R.A. Gingold and J.J. Monaghan. Smoothed particle hydrodynamics: theory and application to non-spherical stars. *Monthly Notices of the Royal Astronomical Society*, 181:375—-389, 1977.

[85] R. Radovitzky, A. Seagraves, M. Tupek, and L. Noels. A scalable 3d fracture and fragmentation algorithm based on a hybrid, discontinuous galerkin, cohesive element method. *Computer Methods in Applied Mechanics and Engineering*, 200:326–344, 2011.

[86] R.D. Mindlin. Second gradient of strain and surface-tension in linear elasticity. *International Journal of Solids and Structures*, 1:417–438, 1965.

[87] R.F. Stellingwerf and C.A. Wingate. Impact modeling with smooth particle hydrodynamics. *Società Astronomica Italiana*, 65:1117–1128, 1994.

[88] R.H.J. Peerlings. *Enhanced Damage Modelling for Fracture and Fatigue.* PhD thesis, Technical University of Eindhoven, 1999.

[89] R.W. Macek and S.A. Silling. Peridynamics via finite element analysis. *Finite Elements in Analysis and Design*, 43:1169–1178, 2007.

[90] S. Beissela and T. Belytschko. Nodal integration of the element-free galerkin method. *Computer Methods in Applied Mechanics and Engineering*, 139:49–74, 1996.

[91] S. Bochkanov. ALGLIB. Online: http://www.alglib.net, 2013.

[92] S. De and J. Bathe. The method of finite spheres. *Computational Mechanics*, 25:329–345, 2000.

[93] S.A. Silling. Reformulation of elasticity theory for discontinuities and long-range forces. *Journal of the Mechanics and Physics of Solids*, 48:175–209, 2000.

[94] S.A. Silling and E. Askari. A meshfree method based on the peridynamic model of solid mechanics. *Computers and Structures*, 83:1526–1535, 2005.

[95] S.A. Silling and F. Bobaru. Peridynamic modeling of membranes and fibers. *International Journal of Non-Linear Mechanics*, 40:395–409, 2004.

[96] S.A. Silling and R.B. Lehoucq. Convergence of peridynamics to classical elasticity theory. *Journal of Elasticity*, 93:13–37, 2008.

[97] S.A. Silling, and R.B. Lehoucq. Peridynamic theory of solid mechanics. *Advances in Applied Mechanics*, 44:73–168, 2010.

[98] S.A. Silling, M. Epton, O. Weckner, J. Xu, and E. Askari. Peridynamic states and constitutive modeling. *Journal of Elasticity*, 88:151–184, 2007.

[99] S.A. Silling, M. Zimmermann, and R. Abeyaratne. Deformation of a peridynamic bar. *Journal of Elasticity*, 73:173–190, 2003.

[100] S.A. Silling, O. Weckner, E. Askari, and F. Bobaru. Crack nucleation in a peridynamic solid. *International Journal of Fracture*, 162:219–227, 2010.

[101] H. Schardin. Physikalische vorgange bei hohen belastungen und belastungseschwindigkeiten (physical processes at high loadings and loading rates). *Scripts of the German Academy for Aeronautical Research*, 40, 1939.

[102] H. Schardin. Results of cenimatographic investigation of the fracture process in glass. *Glastechnische Berichte (Reports on Glass Technology)*, 23, 1950.

[103] A. Seagraves and R. Radovitzky. *Dynamic Failure of Materials and Structures*, chapter 12 Advances in Cohesive Zone Modeling of Dynamic Fracture, pages 349–405. Springer, 2009. DOI.

[104] Andrew Seagraves. *Next Generation Computational Tools for Extreme-Scale simulation of Dynamic Fracture and Fragmentation in Three Dimensions.* PhD thesis, Massachusetts Institute of Technology, 2013.

[105] R.P. Singh, J. Lambros, A. Shukla, and A.J. Rosakis. Investigation of the mechanics of intersonic crack propagation along a bimaterial interface using coherent gradient sensing and photoelasticity. *Proceedings of the Royal Society A*, 453(1967):2649–2667, 1997.

[106] S.N. Atluri and T. Zhu. A new Meshless Local Petrov-Galerkin (MLPG) approach in computational mechanics. *Computational Mechanics*, 22:117–127, 1998.

[107] T. Belytschko and T.J.R. Hughes. *Computational Methods for Transient Analysis.* Elsevier Science, North-Holland, 1983.

[108] T. Belytschko, Y.Y. Lu, and L. Gu. Element-free Galerkin methods. *International Journal for Numerical Methods in Engineering*, 37:229–256, 1994.

[109] T. Kenkmann, F. Horz, and A. Deutsch, editor. *Large meteorite impacts III.* The Geological Society of America, Boulder, Colorado, 2005.

[110] T. Rabczuk, E. Samaniego, and T. Belytschko. Simplified model for predicting impulse loads on submerged structures to account for fluid-structure interation. *International Journal of Impact Engineering*, 34:163–177, 2007.

[111] A. Ten Eyck and A. Lew. Discontinuous Galerkin methods for non-linear elasticity. *International Journal for Numerical Methods in Engineering*, 67:1204–1243, 2006.

[112] H.V. Tippur, S. Krishnaswamy, and A.J. Rosakis. A coherent gradient sensor for crack tip deformation measurements: analysis and experimental results. *International Journal of Fracture*, 48:193–204, 1991.

[113] T.J.R. Hughes. *The finite element method: Linear static and dynamic finite element analysis.* Dover Publications, Inc, New York, 2000.

[114] T.L. Warren, S.A. Silling, A. Askari, O. Weckner, M.A. Epton, and J. Xu. A non-ordinary state-based peridynamic method to model solid material deformation and fracture. *International Journal of Solids and Structures*, 46:1186–1195, 2009.

[115] P. Umberger. Experimental evaluation of dynamic crack branching in poly(methyl methacrylate) (pmma) using the method of coherent gradient sensing. Technical Report ARL-CR-637, Army Research Labs, 2010. pdf.

[116] W.G. Hoover. Smooth-particle applied mechanics: Conservation of angular momentum with tensile stability and velocity averaging. *Physical Review E*, 69, 2004.

[117] W.K. Liu, S. Jun, and Y.F. Zhang. Reproducing kernel particle methods. *International Journal for Numerical Methods in Fluids*, 20:1081–1106, 1995.

[118] W.K. Liu, S. Li, and T. Belytschko. Moving least square reproducing kernel methods (I) methodology and convergence. *Computer Methods in Applied Mechanical Engineering*, 143:113–154, 1997.

[119] X. Chen and M. Gunzburger. Continuous and discontinuous finite element methods for a peridynamics model of mechanics. *Computer Methods in Applied Mechanics and Engineering*, 200:1237–1250, 2011.

[120] Q. Yang, L. Stainier, and M. Ortiz. A variational formulation of the coupled thermo-mechanical boundary-value problem for general dissipative solids. *Journal of the Mechanics and Physics of Solids*, 54:401–424, 2006.

[121] Y.D. Ha and F. Bobaru. Studies of dynamic crack propagation and crack branching with peridynamics. *International Journal of Fracture*, 162:229–244, 2010.

[122] Y.Y. Zhang and L. Chen. Impact simulation using simplified meshless method. *International Journal of Impact Engineering*, 36:651–658, 2009.

[123] Y.Y. Zhu and S. Cescotto. Unified and mixed formulation of the 4-node quadrilateral elements by assumed strain method: application to thermomechanical problems. *International Journal for Numerical Methods in Engineering*, 38:685–716, 1995.

[124] Z.D. Han, H.T. Liu, A.M. Rajendran, and S.N. Atluri. The applications of meshless local Petrov-Galerkin (MLPG) approaches in high-speed impact, penetration and perforation problems. *Computer Modeling in Engineering & Sciences*, 14:119–128, 2006.

[125] Z. Zhang and G.H. Paulino. Cohesive zone modeling of dynamic failure in homogeneous and functionally graded materials. *International Journal of Plasticity*, 21:1195–1254, 2005.

[126] Z.P. Bazant and M. Jirasek. Nonlocal integral formulations of plasticity and damage: Survey of Progress. *Journal of Engineering Mechanics*, 128:1119–1149, 2002.